THE UNIVERSITY OF CHICAGO

NEXT GENERATION CATHODE MATERIALS FOR HIGH VOLTAGE APPLICATIONS

A DISSERTATION SUBMITTED TO

THE FACULTY OF THE PRITZKER SCHOOL OF MOLECULAR ENGINEERING

IN CANDIDACY FOR THE DEGREE OF

DOCTOR OF PHILOSOPHY

BY

ALVIN DAI

CHICAGO, ILLINOIS

JUNE 2024

TABLE OF CONTENTS

LIST OF FIGURES

LIST OF TABLES

NOMECLATURE

Abbreviations

ACAT	Argonne chromatic aberration-corrected
AC-STEM	Aberration corrected scanning transmission electron microscopy
APS	Advanced Photon Source
BCDI	Bragg coherent diffraction imaging
BET	Brunauer, Emmet, and Teller
BEV	Battery electric vehicles
CGS	Concentration gradient shell
CMCD	Coherent multi-crystal diffraction
CRED	Continuous rotation electron diffraction
CSTR	Continuous stirred tank reactor
DEMS	Differential electrochemical mass spectrometry
DFT	Density functional theory
DRX	Disordered rock salt
EDS	Energy dispersive spectroscopy
EELS	Electron energy loss spectroscopy
EIS	Electrochemical impedance spectroscopy
EXAFS	Extended x-ray absorption fine structure
FFT	Fast fourier transform
GITT	Gravimetric intermittent titration technique
HEXRD	High energy x-ray diffraction
HRTEM	High resolution transmission electron microscopy
KB	Kirkpatrick-Baez
LCO	Lithium cobalt oxide
LFP	Lithium iron phosphate
LIB	Lithium ion batteries
LMO	Spinel Manganese Oxide
LMR	Lithium and Mn rich
LR	Lithium Rich
LRND	Lithium rich nano domain
MS-NMC	Multi-structure NMC
NCA	Lithium nickel cobalt aluminum
NMC	Lithium nickel manganese cobalt oxide
OCV	Open circuit voltage
PLC	Programmable logistics controller
SAED/SAD	Selected area electron diffraction
SC	Single crystal NMC

SEM	Scanning electron microscopy
SXAS	Soft x-ray absorption spectroscopy
SXDM	Scanning x-ray diffraction microscopy
TEM	Transmission electron microscopy
TM	Transition metal
TXM	Transmission x-ray microscopy
XANES	X-ray absorption near edge spectroscopy
XAS	X-ray absorption spectroscopy
XRD	X-ray diffraction
2D	Two dimensional
3D rED	Three dimensional rotation electron diffraction
3D XRF	Three dimensional x-ray fluorescence

Greek Letters

α	Alpha Structure
σ	Conductivity
τ	Pulse Time

Symbols

a	a-axis
b	b-axis
c	c-axis
a*	Reciprocal axis a
b*	Reciprocal axis b
c*	Reciprocal axis c
C	Charge rate
°C	Degrees Celsius
D_{Li^+}	Li Diffusion Coefficient
ΔE	Voltage Difference
H	Hexagonal Structure
M	Monoclinic Structure
dQ/dV	Differential Capacity and Voltage
R_s	Equivalent Radius
R_{wp}	R-Factor
V	Voltage

ACKNOWLEDGEMENTS

Without the support of my cherished family, friends, and colleagues, graduate school would have been a far lonelier journey. Their encouragement and insights have undoubtedly helped me grow, mature, and become the scientist I am today. There are all too many I must thank, but I will mention some below.

Since 2018, Khalil Amine has provided me his unwavering support and for that I am forever grateful. At the end of my internship at Argonne, it is with his encouragement and willingness to financially support me that I pursued a Ph.D. Also at the time Jun Lu and Tongchao Liu became my great mentors and good friends. I must especially thank Tongchao for his guidance, mentorship, and insightful conversations that have helped shape my scientific interests and career forever. I will miss Khal, Jun, and Tongchao for our shared love of fine wines, good food, and curiosity for science as I move on in my career, but I am heartened knowing our paths will undoubtedly cross again. I must also thank the numerous colleagues at Argonne that had made my daily work there that much more enjoyable with their conversation, cheer, and camaraderie.

From the University of Chicago, I must thank the many professors, classmates, and staff from which I have been able to learn much across science, engineering, business, and humanities. In particular from Pritzker School of Molecular Engineering, Tony Pan, Jeremiah Kim, Carlos Medina, and Baiyang Dai have been the best of friends to journey through graduate school with. I will always cherish the memories and adventures we have had in our time, and look forward to more in the future. Also, many from the Booth School of Business have left a lasting impression on me. I must thank the University of Chicago broadly for allowing students to explore interests in a broad range of fields as I have benefitted greatly from this.

In my time at Apple, I have also made a number of good friends and colleagues from which I have learned much from. My work in the Battery Material Development team and the Battery Diagnostics and Root Cause Analysis team have allowed me to learn from a collection of some of the brightest minds in battery technology. The experiences I have had, the mentors I have had, and memories I have made will remain with me for a lifetime. Specifically, I must thank Munir Besli, Xiang Li, Daniel Park, Lei Liu, and Henry Dai for their support and mentorship. Among the other interns, I would also like to thank Aashray Narla, Steven Lee, and Philaphon Sayavong for their friendship, shared interests in batteries, and for making the work day easier with their conversation. I hope we are able to work together again in the future.

Furthermore, I would like to thank my personal friends and family. From my undergraduate years, I would like to thank Adam Erlichman and Zane Ostoin for their lasting friendship and uncountable adventures that have been shared. I would also like to thank Keegan Adair, who started as a colleague at Argonne during his post doc, and has since become a wonderful friend, advice giver, and running partner. Finally, I would like to thank those that know me best. I will forever cherish my best friend and cat, Spike, who has been the best companion and has gone through all the ups and downs of the graduate school journey with me. My partner, Manasa Padmanabhan, and her dog Mickey have been a wonderful distraction from finalizing my Ph.D. It is with their company and love that I can stay grounded. Finally my family, Lin Zhu, Quanbin Dai, and Liming Dai who have always supported me and always will. Every step of the graduate school journey and from even before, they have been with me. I could not want for a more loving and supportive family as it is only with their warm encouragement, thoughtful advice, and undying care that I am where I am today. To them and all those that have helped me along the way, thank you.

ABSTRACT

Inexpensive and high energy density cathode materials can decrease battery electric vehicle (BEV) cost and increase driving range, which are barriers to consumer adoption. Current state of the art BEV cathode is layered nickel manganese cobalt (NMC) oxide, which acts as the Li source and intercalates Li during discharge. Recently however, Co and Ni prices have skyrocketed due to supply chain challenges, which has increased material supplier costs and BEV prices indirectly. Therefore, next generation cathode materials that are cheap, robust, and long lasting can address cost and energy density limitations faced by NMC.

Direct pathways to reduce NMC cost and increase energy density are to utilize materials with lower input costs and operate the cathode material at higher voltages (> 4.5 V). However, when Co or Ni components are substituted for cheap materials (e.g., Mn) their performance can worsen. Similarly, when NMC are operated at higher voltages, the layered structure framework destabilizes, and phase transitions occur. This causes particle cracking, which exposes new surfaces to electrolyte and consumes active material. Clearly, there are tradeoffs for NMC development where low cost leads to low energy density and high voltages lead to poor longevity.

In the battery field, rather than only modify NMC, there is interest in developing cathode chemistries that are not restricted by the intrinsic limitations of NMC. To reduce cost, chemistries that contain high contents of Mn and provide high capacity through anionic redox, such as lithium rich (LR), are of interest. Unfortunately, practical use of LR is limited by poor longevity, which has been attributed to voltage fade caused by oxygen release. However, efforts to prevent oxygen release have not improved performance, which raises the question if oxygen release is even the root cause of voltage fade. For high voltage stability, single crystal nickel

manganese cobalt oxide (SC) cathodes consist of single grain morphologies that minimize particle cracking and electrolyte exposure. In theory, SC should be able to improve longevity at high voltages, but SC have higher costs due to more complex synthesis. Moreover, reducing Co content would directly lower SC costs, but few studies have discussed Co free SC performance. Although LR and SC can resolve tradeoffs between cost and energy density or energy density and longevity, there are clear knowledge gaps that prevent practical use.

In this dissertation, research has been conducted to resolve these knowledge gaps. Chapter 2 describes the use of advanced characterization techniques that span multiple length scales to clarify the origin of oxygen release in LR cathodes and ultimately voltage fade. Irreversible strain accumulation and release due to different redox activity in composite structures was found to be the root cause and strategies to address them are proposed. In chapter 3, the effects of Co removal on SC are investigated to better understand tradeoffs between cost and performance. Interestingly, when Co was removed a LR nano domain formed in SC, which induced particle strain and reduced longevity at high voltages. This also contrasts with NMC where performance at high voltages improved after Co removal.

Moreover, these insights from LR and SC have inspired the design of a multi structure NMC (MS-NMC) cathode as described in chapter 4. MS-NMC, integrates cathodes that are redox active, structurally coherent with NMC, and intrinsically stable at high voltages, such as LR or disordered rock salt (DRX), with NMC into one particle. NMC, LR, and DRX are also spatially controlled to reside in the bulk, interlayer, and surface respectively, to optimize their performance contribution. This work is among the first to describe controlled synthesis of multi structure cathodes and serves to inspire pathways to develop other cathode material types. Finally, chapter 5 summarizes the collected results and outlooks for future work are described.

Chapter 1

Introduction

Battery technologies play a critical role in enabling renewable energy technologies that can help alleviate challenges with climate and sustainability. The growing interest in grid scale energy storage, the fast proliferation of electric mobility, and the adoption of battery electric vehicles (BEV) are a few key efforts.[1] However, the demand for these technologies is growing exponentially and the current battery supply chain may not be able to handle the capacity (Figure 1.1a).[2] For BEV, lithium-ion batteries (LIB) account for nearly 40% of the cost due to materials expenses and are the main the source of energy to power the vehicle.[3] This makes them critical in determining the market competitiveness of BEV with cheaper combustion vehicles, performance, and material supply chain.[4] As a result, several governmental policies have been enacted recently to accelerate BEV development, especially efforts focused on growing supply chain and manufacturing.[5]

Within these LIBs, the major components include negative (anode) and positive (cathode) electrodes, electrolytes, separators, as well as the cell casing and battery management systems.[6] When LIBs charge and discharge, lithium ions are shuttled between the cathode and anode while electrons pass through an external circuit to power devices.[7] The separator is permeable to ion diffusion and acts as an insulating membrane that prevents an electrical short circuit.[8] The electrolyte, typically a lithium salt (e.g., $LiPF_6$ and $LiClO_4$) dissolved in a mixture of ethylene carbonate and either dimethyl carbonate, diethyl carbonate, or ethyl methyl carbonate, conducts Li ions between the electrodes.[9] Given the versatility of LIB applications, numerous materials have been developed with unique chemistries, structures, and properties. However, regardless of the design, the cathode acts as the lithium source in these batteries and therefore is a key determining

factor on battery energy density.[10] As a result, significant research efforts in academia and industry are focused on improving fundamental material development, mass production, and final integration of cathode materials into devices such as BEV.[11]

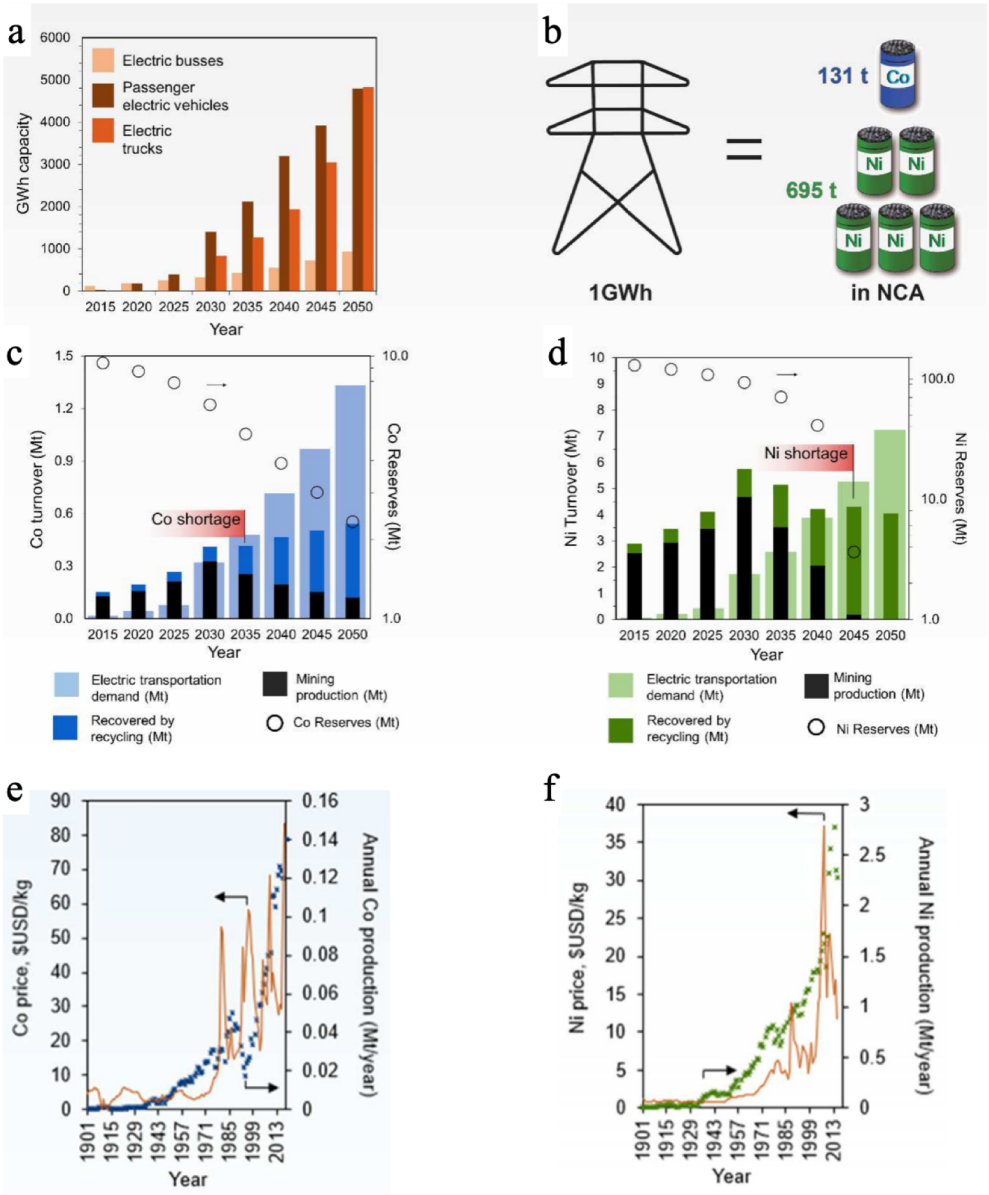

Figure 1.1. Demand forecasts for batteries and intercalation cathodes. (a) Battery production capacity needed to meet electric vehicle market growth. (b) Amount of Co and Ni that go into 1 GWh of NCA material. (c, d) Co and Ni raw material demand conditions that lead to supply shortage. (e, f) Historical prices for Co and Ni. Adapted from *refs. 2*.

Cathode materials typically undergo transition metal (TM) oxidation and reduction to charge and discharge during battery operation.[12] This cationic redox mechanism acts to shuttle Li^+ between the cathode and anode while electrons move through an external device.[13] Currently, a variety of chemistries are favored for commercial use, with the most common being $LiCoO_2$ (LCO), $LiFePO_4$ (LFP, theoretical capacity: 169 mAh g^{-1}), spinel $LiMn_2O_4$ (LMO, theoretical capacity: 148 mAh g^{-1}), $LiNi_xMn_yCo_zO_2$ (NMC, where x + y + z = 1 capacity: 160-200 mAh g^{-1} depending on Ni content), and $LiNi_xCo_yAl_zO_2$ (NCA, where x + y + z = 1, capacity 200 mAh g^{-1}).[14] LCO was first commercialized in 1991 but has been limited to portable applications as the available specific capacity (140 mAh g^{-1}) is only half of its theoretical capacity due to overcharge instability.[15] Although LFP exhibits high thermal stability due to its phosphate moieties, excellent cycle life, flat charge/discharge, and electrochemical stability, its low energy density and nominal voltage (~3.3V) limits its use to short range BEV.[16] LMO on the other hand enables 3D solid state diffusion that achieves high-rate capability but suffers from low practical capacity and cycle life due to Jahn-Teller distortion induced by Mn^{3+}.[17] Among these chemistries, state of the art NMC and NCA are most suitable for use in BEV given their high energy density (150-170 Wh kg^{-1} at pack level), good rate capability, and cyclability with an average price of US \$176 kWh^{-1} at pack level.[18] However, to fully compete with combustion vehicles, the U.S. Department of Energy has estimated that automotive batteries must deliver 235 Wh kg^{-1}/500 Wh l^{-1} at \$100 kWh^{-1} at pack level (350 Wh kg^{-1}/750 Wh l^{-1} at \$75 kWh^{-1} at cell level).[19]

To achieve these targets, NMC and NCA play a critical role in cost reduction as Co and Ni prices continue to skyrocket due to supply chain challenges and material sourcing constraints.[20] With current market trends, the demand will outgrow supply for Co by 2035 and for Ni by 2045 (Figure 1.1c and d).[21] Furthermore, the high content of Co and Ni used in commercial NMC and

NCA already account for a large percentage of the battery pack cost in BEV, which presents significant opportunity to decrease BEV cost.[22] For example, 1 GWh of NCA material equates to 131 tons of Co and 695 tons of Ni (Figure 1.1b) and when considering Co and Ni market prices (Figure 1.1e and f) as well as their exponential growth, it is clear why it is difficult to make cheap BEV.[21] As a result, sophisticated efforts to reduce NMC or NCA cathode cost and increase energy density can help achieve the price and performance benchmarks needed to accelerate BEV consumer adoption.

1.1 Overview of NMC and NCA

Prior to developing lower cost and robust NMC and NCA, understanding is needed on the current state of the art technology. Commercial NMC and NCA typically operate between 4.3 V to 3.0 V, provide 160-200 mAh g^{-1}, and have spherical morphology where average particle sizes are about 10 um.[23] Typically, increasing Ni content will increase capacity as be seen for NMC111 vs NMC900505 (Figure 1.2a and c), but cathode material longevity will be worsened.[24] Structurally, NMC and NCA cathodes exhibit α-$NaFeO_2$-type structure with a hexagonal layered phase (space group: R-3m) where Li and O atoms are placed on 3a and 6c sites in the crystal structure respectively.[25] Each of the three transition metals in NMC and NCA are distributed throughout 3b sites randomly and serve a unique purpose.[26] Ni provides high specific capacities, while Co and Mn facilitate layered structures and enhance structural integrity.[27] Due to similar radii sizes and magnetic frustration, Ni^{2+} (0.69 Å) and Li^{+} (0.76 Å) atoms tend to exchange positions, a phenomenon known as Li/Ni mixing that reduces cyclable capacity and rate capability.[28] Co and Al enhance rate capability by reducing Li^{+}/Ni^{2+} mixing given their nonmagnetic properties and smaller radii (Co^{3+} = 0.54 Å, Al^{3+} = 0.53 Å).[29] The presence of Mn and Al are critical for cycle and thermal stability as they suppress multi-step two-phase reactions and stabilize the layered structure

during de(lithiation).[30] During charge/discharge, the chemical valences of Ni ($t_{2g}^6e_g^2$), Co ($t_{2g}^6e_g^0$), and Mn ($t_{2g}^3e_g^0$) in NMC are +2, +3, and +4 respectively.[31] In the presence of Mn, Ni 3+/4+ redox shifts to Ni 2+/3+ as electrons in the e_g band of Mn^{3+} tend to transfer to the electronic orbit of Ni^{3+}, which can promote Ni/Li mixing.[32] The valence state of Mn and Al, since it is redox inactive, remains unchanged during electrochemical cycling, which stabilizes the structure, and Ni 2+/3+, Ni 3+/4+, and Co 3+/4+ redox occurs.[33] Typically, this valence state change will also change TM bonding lengths which can lead to phase transitions during cycling.

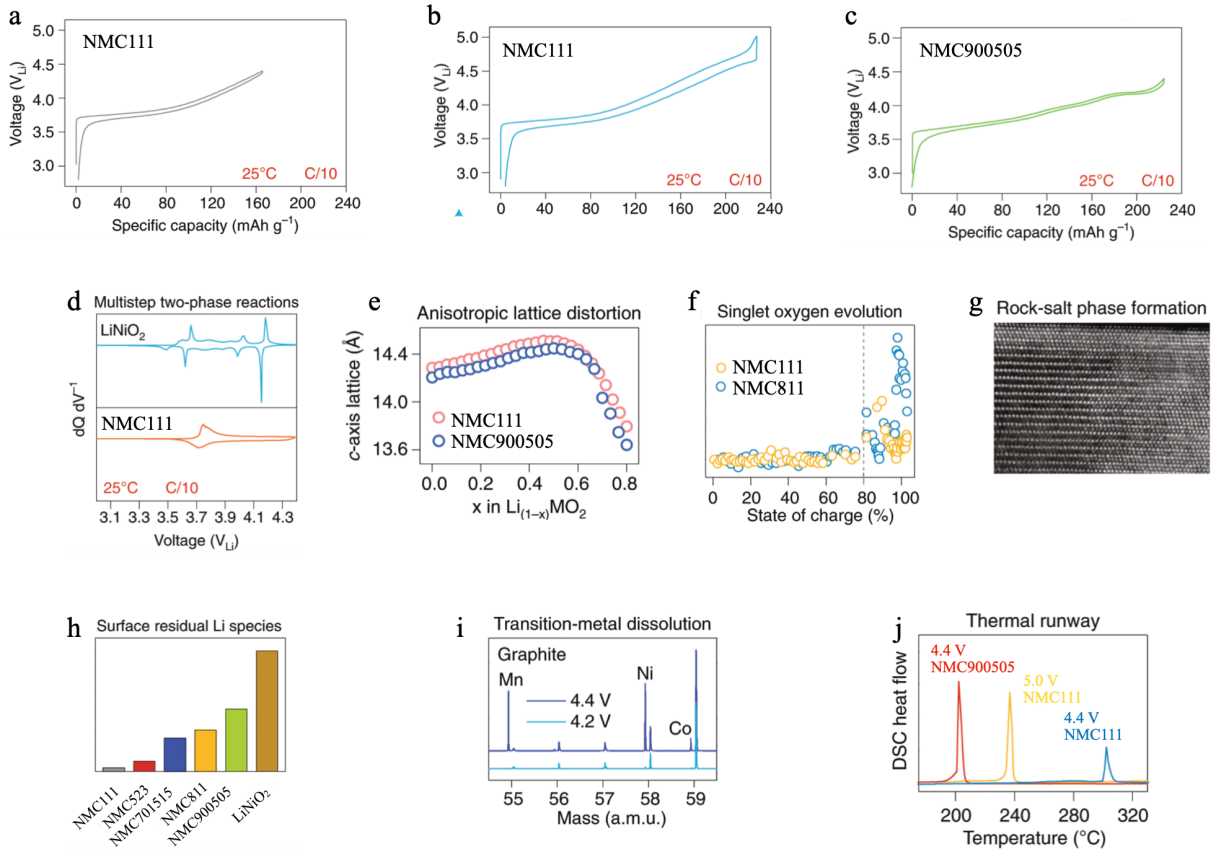

Figure 1.2. Performance challenges of high Ni and high voltage NMC as evidenced through various characterization methods. (a) First cycle of NMC111 charged to 4.4 V, (b) charged to 5.0 V, and (c) NMC900505 charged to 4.4 V. Higher voltage and higher Ni content increase discharge capacity. However, when NMC Ni contents are increased, (d) structure transition-dQ/dV, (e) lattice evolution-XRD, (f) oxygen release-DEMS, (g) TEM-irreversible phase transition, (h) residual Li surface byproduct content-Titration, (i) TM dissolution-ICP-MS, and (j) thermal stability-DSC are all more severe. These figures show how high voltage and high Ni composition lead to poor longevity. Adapted from *refs*. *24*.

Conventional efforts to improve energy density in NMC and NCA batteries have included using dopants and coatings to stabilize structure or morphology.[34] For example, elements that are larger than Al^{3+} and are also stable in the 3+ oxidation state such as Y^{3+} can act similarly to replace Al.[35] The efficacy of these doping and coating modifications are highly dependent on the oxidation state, steric properties, morphology, and stability of the applied material additives. Moreover, there are tradeoffs to using excess amounts of these modifications, such as reduced capacity due to increased contents of non-active sites or worsened kinetics due to inactive coating.[36] Conventional modifications have limits, but in order to truly develop robust cathode materials, understanding is needed as to what causes NMC or NCA to fail during cycling.

1.2 NMC and NCA Failure Mechanism

Structure and morphology are key factors that determine the stability and performance of NMC and NCA cathode materials. Structurally, they consist of ordered two dimensional layers of TM and Li ions that stack and alternate to form a layered crystalline structure in the pristine state.[37] When Li ions are inserted or removed during discharge or charge, the lattice framework will destabilize, and phase transitions will occur due to layer collapse, lattice gliding, or TM oxidation state change.[38] In particular, the TM oxidation state is a key determinant for structure behavior as redox activity directly influences local coordinate bonding with oxygen anions and discharge voltage. Elements with high oxidation state such as Ni^{4+} are in higher concentration when batteries are in a charged state and are highly prone to oxidate solvents when in contact with electrolyte which can lead to formation of surface by products or transition metal dissolution (Figure 1.2h and i).[39] Eventually, as these reactions propagate gas release and risks for thermal runaway hazards also increase (Figure 1.2f and j) which deteriorate battery performance and safety.[40] On the other hand, when oxidation states are low at the electrolyte interface, TM may have undergone O release

and are in Ni^{2+} or Co^{2+} states, which can cause lattice site exchanges.[41] After significant decomposition, a critical content of TM in the 2+ state will develop and irreversible phase transition from layered to spinel or rock salt is possible (Figure 1.2g). [42] Note that, rock salt phase takes on similar structure to disordered rock salt (DRX) type cathode materials, but DRX range across a variety of chemistries and are its own class of cathode.[43] Therefore DRX can share certain properties with rock salt phase but are distinct from each other. NMC or NCA at end of life have contents of rock salt, which is a structure type where Li and TM disordering are at such an extent that distinct layers are no longer present, Li diffusion occurs through percolation instead of intercalation, and anionic redox processes occur.[44] At this state, the capacity of the material is irreversibly reduced.

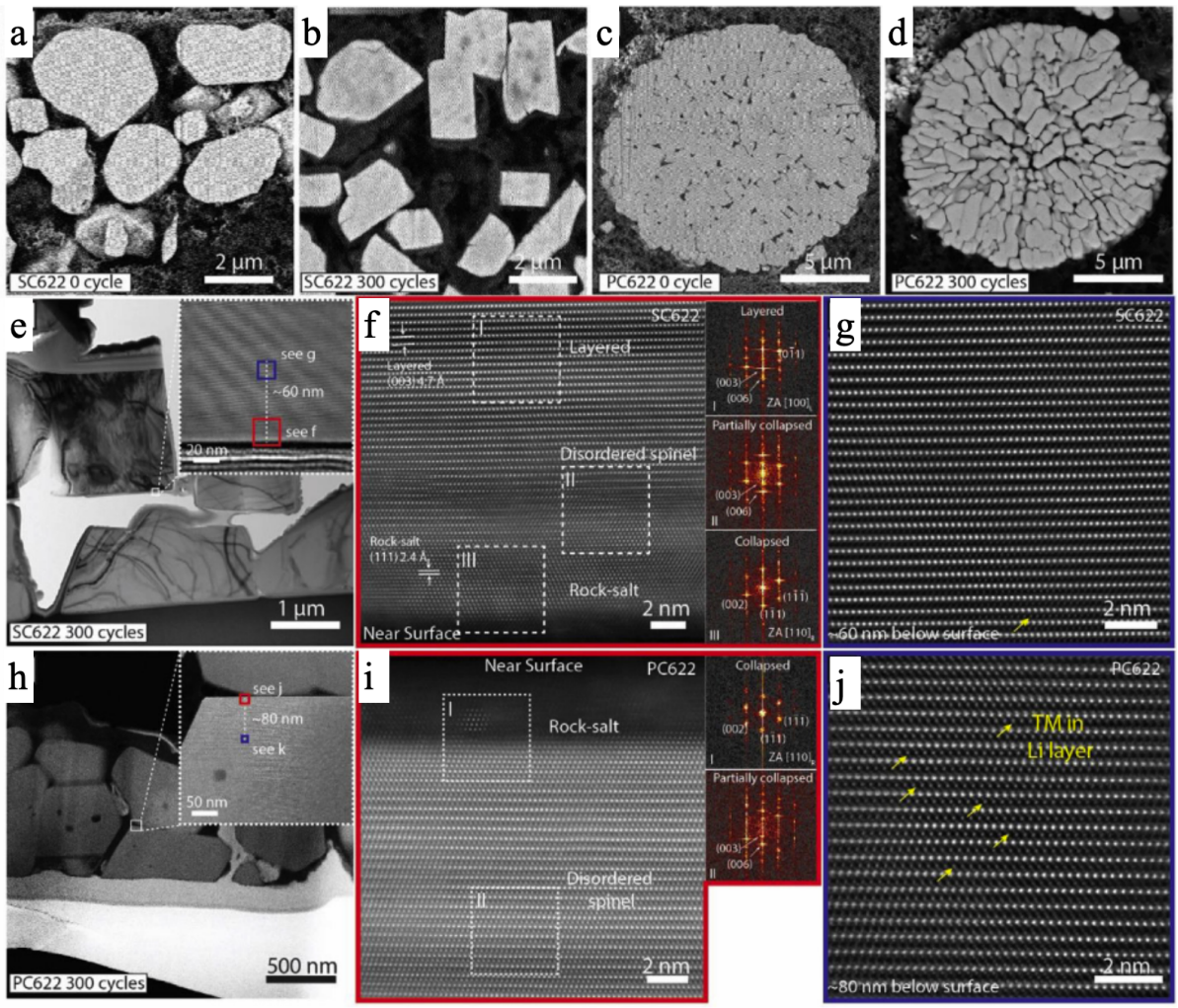

Figure 1.3. (a, b) Cross-sectional SEM images of single crystal NCM (SC-NCM) 622 electrodes before cycling and after 300 cycles, respectively. (c, d) Cross-sectional SEM images of polycrystalline NCM622 before cycling and after 300 cycles, respectively. The SC-NCMC622 particles show no cracking, whereas polycrystalline NCM 622 cracks extensively along grain boundaries. (e, f, g) are HAADF-STEM images and the associated selected-area FFT analysis for electrochemically cycled SC-NCM622 particle orientated along the [100] zone axis. (h, i, j) are structural characterization and analysis for cycled polycrystalline NCM622 grain located close to the center of the secondary particle. More spinel like phases were formed in the case of the cycled polycrystalline NMC622 than SC-NMC 622. More transition metal atoms were observed to occupy interstitial sites originally for Li in the cycled polycrystalline NMC622 particle, as indicated by the yellow arrows. Reproduced with permission from *refs*. *45*.

As for morphology, NMC and NCA crystallize as polycrystalline, secondary spherical particles through the random orientation of primary nanoparticles that undergo volume expansions and intergranular cracking during operation (Figure 1.3c), which is exacerbated with increases in Ni composition and oxidation state.[45] These randomly oriented primary particles undergo phase

transitions (H1 > M > H2 > H3) and *c*-axis lattice increases during charge (Figure 1.2d), where the H2 (a = 2.82 Å, c = 14.40 Å) to H3 (a = 2.81 Å, c = 13.36 Å) transition involves a sudden lattice contraction (Figure 1.2e).[46] These dynamic structure phase transitions are due to the oxidation state changes in TM as the battery is cycled. However, sudden lattice contraction at the boundary between primary particles can occur at uneven rates and produce microstrain that lead to particle cracking.[47] Cross sections images of NMC622 after 300 cycles show that intergranular cracking and voids formation was significant (Figure 1.3d).[45] When these particles crack, new surfaces are exposed to electrolyte which undergo structural decomposition to inactive structures as described previously. Rock salt formation after cycling is clearly present at the surface of NMC622 after cycling and transitions to a layered or spinel phase in the bulk (Figure 1.3h and i).[45] Bright TM spots in the Li layers are also characteristic of significant rock salt formation as they arise from TM disordering and are visible near the surface (Figure 1.3j). Collectively, these data indicate that electrolyte exposure may be a root cause of decomposition and structure or morphology decomposition must be prevented to improve NMC or NCA cathode materials.

Moreover, another metric where these materials fail is cost.[3] NMC and NCA that are used commercially utilize large contents of Co and Ni, which are becoming increasingly expensive and are facing supply chain challenges.[22] Co and Ni also account for a significant portion of the total cost a BEV battery and of the cathode. However, when cheaper elements such as Mn are used extensively to replace Co or Ni, the performance of the batteries can suffer.[48] High contents of Mn in NMC have been observed to decrease capacity, energy density, and rate capability.[49] Therefore, this presents a clear tradeoff where achieving low cost can lead to low energy density. New cathode chemistries that are cheap and robust are needed to overcome this intrinsic limitation.

Altogether, the primary challenges facing commercial NMC and NCA today are cost and energy density which are intrinsically linked to the chemistry, morphology, and structure of the material. A direct pathway to overcome these challenges are to replace expensive elements with suitable cheap materials and to modify them to enhance performance. Efforts to replace NMC with cheaper elements have seen decreases in performance, presenting a tradeoff between cost and performance. As for energy density, raising the operational voltages to higher voltages (> 4.5 V) is a straightforward method to increase energy density as more Li ions will be extracted from the cathode material, as can be seen for NMC111 (Figure 1.2b).[12] However, at high levels of delithiation the lattice framework is unstable, and structure and morphology deterioration are compounded. This presents a clear tradeoff between energy density and longevity where high voltage operation will exacerbate cathode failure (Figure 1.2). Conventional modification methods are also unable to resolve these performance challenges at high voltages and are only able to delay decomposition, as they do not intrinsically alter the layered crystal structure that underlie the root cause of failure. Therefore, in the battery field, instead of continuing to modify NMC or NCA, there is interest in developing new chemistries or material types that are not limited by the tradeoffs between cost and energy density or energy density and longevity.

Note however, it is important to discuss some commonalities between different cathode materials. First, the cost of all cathode materials is intrinsically linked to the elements that they are made of. Therefore, regardless of if a chemistry is optimized for longevity or for energy density, if its component elements are replaced by cheap elements than its cost will be reduced. Second, the energy density of all cathode material types that rely on Li intercalation/deintercalation can be increased by operating at higher voltages, as energy is a function of voltage and capacity. Though the failure modes of each cathode type at high voltages may be different. However, when voltages

are raised over 4.5 V, further Li extraction can also occur through anionic redox pathways in oxide-based cathodes, where instead of TM oxidation state change as through cationic redox, the O^{2-} anions can be oxidized to O^{-}.[50] This will typically result in TM reduction and oxygen gas release from surface sites that may cause material decomposition.[51] Therefore, although excess capacity can be obtained at higher voltage charges potentially due to anionic and cationic redox, longevity may be reduced. When all these factors are considered, insights gained from resolving cost and high voltage challenges in one cathode type may directly impact the development of other cathode materials.

1.3 Next Generation Cathodes to Resolve NMC Challenges

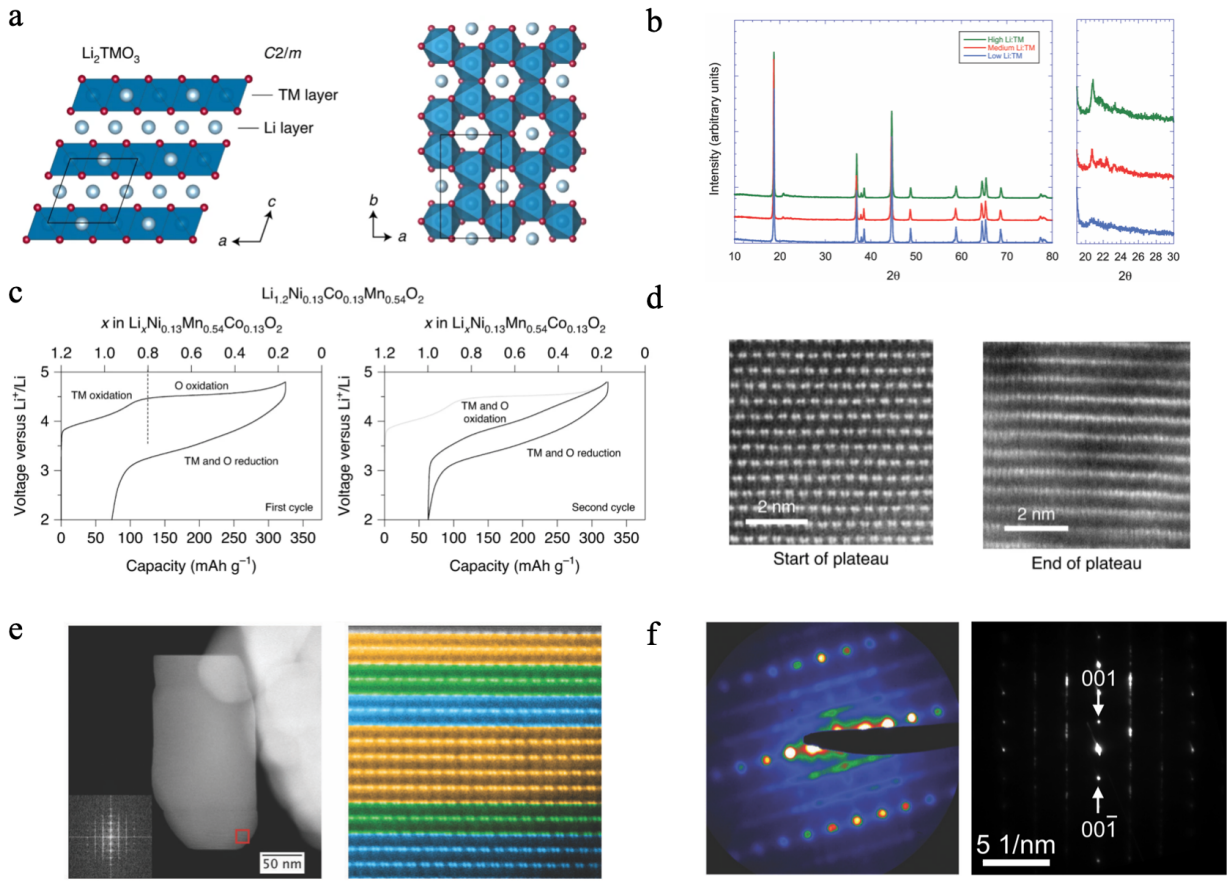

Figure 1.4. LR properties. (a) Crystal structure of LR composite Li_2TMO_3 ($Li[Li_{1/3}TM_{2/3}]O_2$). (b) XRD showing characteristic LR superlattice peaks between 20-30° at high lithiation levels. (c) Typical first and second cycle behaviors using $Li_{1.2}Ni_{0.13}Mn_{0.54}Co_{0.13}O_2$ as LR example. (d) STEM along the [010] direction before and after the charge plateau showing decomposition of the characteristic TM-TM dumbbell ordering in TM layer. (e) TEM images of LR with colors that correspond to three monoclinic variants. (f) Electron diffraction patterns showing diffuse lines that are characteristic LR features due to three monoclinic variants. Adapted from *refs*. *53*, *54*, and *55*.

Although layered cathode materials can universally benefit from low cost and high voltage stability, there are several chemistries more suited for resolving cost, longevity, and energy density tradeoffs. For cost, cathode materials that contain low contents of Ni and Co and high contents of Mn, such as lithium-rich (LR) cathodes, have developed great interest in recent years. LR cathodes can provide high capacities (> 270 mAh g^{-1}) due to high contents of anionic redox activity exhibited around 4.5 V, and stoichiometrically contain higher contents of Li than TM.[52] The

transition between cationic and anionic redox, as well as the extra capacity gain from anionic redox, (Figure 1.4c) is quite clear when looking at a representative LR cathode ($Li_{1.2}Ni_{0.13}Mn_{0.54}Co_{0.13}O_2$) cycled between 2 V to 4.7 V.[53] They are also morphologically spherical, exhibit structural coherence (C2/m) with layered NMC or NCA, and consist of composite layered $LiTMO_2$ and Li-excess Li_2TMO_3 structures (Figure 1.4a).[53] This composite nature leads to some characteristic signals that uniquely identify LR, especially for the Li-excess structures. For example, the C2/m structure arises from Li_2TMO_3, as $LiTMO_2$ are typically $R\bar{3}m$, and causes characteristic super lattice peaks unique to LR to from in x-ray diffraction (Figure 1.4b).[54] Also, due to high contents of Li and TM disordering, the lattice structure of LR can form into a dumbbell type arrangements (Figure 1.4d) where bright lattice points (TM ions) are separated by dim spaces (Li).[55] Furthermore, the unit cells of LR have been observed to stabilize into 3 distinct monoclinic variants, since TM and Li can occupy several lattice site combinations, which are observable along the (100), (110), and $(1\bar{1}0)$ zone axis (Figure 1.4e).[55] When viewed the along the (210) zone axis, characteristic diffuse traces at 1/3 and 2/3 spacing between bright transition metal layers are present due to these variants (Figure 1.4f).[55] However, despite their potential to replace NMC and NCA, LR cathodes undergo significant structural transformation after cycling which leads to poor reversibility, voltage fade, and excessive gas release that restrict usable energy density to levels below commercial application.[52] For example, this voltage fade is already observable in the second cycle of $Li_{1.2}Ni_{0.13}Mn_{0.54}Co_{0.13}O_2$ (Figure 1.4c and d) and indicates how significant the irreversible structural transition can be.[53] Oxygen release has long been considered the root cause of voltage fade and irreversibility in LR, however modifications such as doping and coating have been unable to resolve these challenges thus far.[56] This raises the question of whether oxygen release is in fact

the primary cause for voltage fade and structure decomposition in the first place, but there is a knowledge gap in the literature leaving this unresolved.

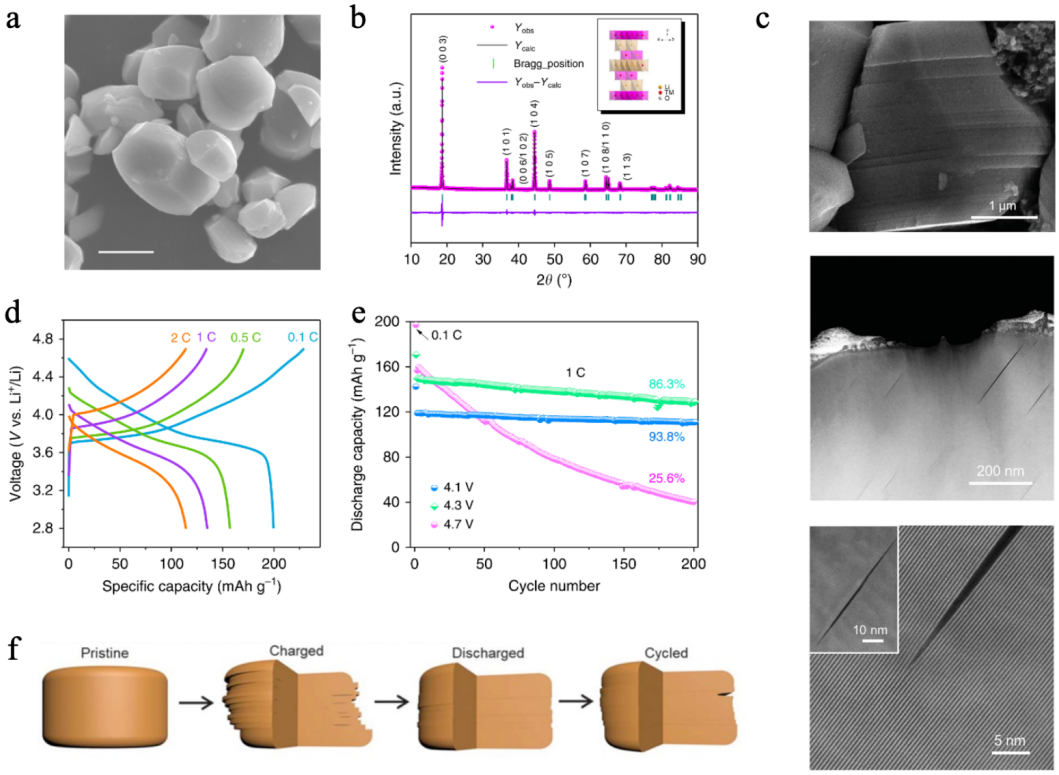

Figure 1.5. SC properties. (a) SEM of image of SC with NMC622 (SC622) composition. (b) Rietveld refinement results for SC and inset depicting structure schematic. (c) SEM (top image) and STEM showing SC lattice defects after extended cycling. (d) Various rate charge-discharge profiles of SC622. (e) Cycle performances at 1C with increasing voltage cut-offs of SC622 (4.1, 4.3, 4.7 V). (f) Schematic showing lattice gliding as a form of SC structure evolution during cycling. Adapted from *refs. 57* and *59*.

In terms of longevity, single-crystal nickel manganese cobalt oxides (SC) form with only one grain per particle (1-3 μm) that are smaller than NMC or NCA (Figure 1.3a and 1.5a) and have attracted increasing attention due to their superior longevity during long cycle times, which exceed those of polycrystalline NMC or NCA.[57] Structurally, SC are analogous to NMC (Figure 1.5b) and exhibit a strong layered formation as evidenced by the (003) peak.[57] After cycling, SC morphologies undergo much less particle cracking (Figure 1.3b) than NMC and irreversible surface transition are also reduced (Figure 1.3e-g).[45] Morphology, particle size, and specific

surface area are critical for electrochemical performance, as small particle sizes can significantly shorten diffusion distances and increase electrode/electrolyte contact, which facilitates fast lithium-ion transfer.[58] These single crystal grain boundaries avoid the intergranular cracking problems of NMC and provide continuous conductive networks in single-crystal particles.[58] In theory, SC should be more stable at high voltages as they resolve particle cracking, have been postulated to reduce oxygen loss, and improve surface contact with electrolyte.[58] However, some electrochemical studies at higher voltages have shown that SC622 longevity decreases severely as voltage is raised from 4.1 V to 4.7 V (Figure 1.5d and e).[57] Other studies have correlated these performance decreases to intragranular cracking and structure transition caused by strains from heterogenous lithiation (Figure 1.5c and f).[59] Additionally, the synthesis process to grow the single grains of SC is more complex than NMC and requires more calcination steps, holding time, as well as higher temperatures.[60] To a material supplier, this can increase input costs and reduce the economic incentive to develop SC. As a result, developing lower cost SC would help realize their practical use. Following the prior discussion, Co removal is also a viable strategy to reduce SC cost. However, few literatures have discussed the impacts that Co removal will have on SC regarding performance, structure, and morphology.[61] Therefore, a clear knowledge gap exists whereby understanding is needed on the impact of Co removal in SC. Interestingly, when Co has been removed from NMC, longevity performances at high voltage operation improved.[49]

Finally, efforts to increase the energy density of NMC or NCA have also focused on advanced chemistry designs such as core-shell, concentration gradient, or full-concentration gradient design types (Figure 1.6a-c).[62-64] The key concept behind these materials is to control the chemical distribution of active materials to improve performance. For example, the contents of Mn will be increased towards the surface of these particles as it is more stable against electrolyte, while

the content of Ni will be higher at the bulk of particle since Ni is highly reactive with electrolyte. Core-shell designs have an abrupt transition between the Ni and Mn portion, concentration gradient have a smooth transition from Ni to Mn at an interface near the surface, and full concentration gradient have a continuous transition Ni rich to Mn rich from the bulk to the surface.[62-64] Each development led to more homogenous chemical distribution, improved particle stability, and electrochemical performance, which generally led to improved capacity (Figure 1.6d-f) and longevity (Figure 1.6g-i) when compared to NMC.[62-64] Although the core idea of controlling element distribution to enable robust performance is inspiring, nevertheless the intrinsic challenges that face all NMC due to their layered structure, especially at high voltages (e.g., lattice instability, phase transition), remain unresolved by these advanced designs. Therefore, alternative strategies that can address the intrinsic structural challenges of these materials are needed.

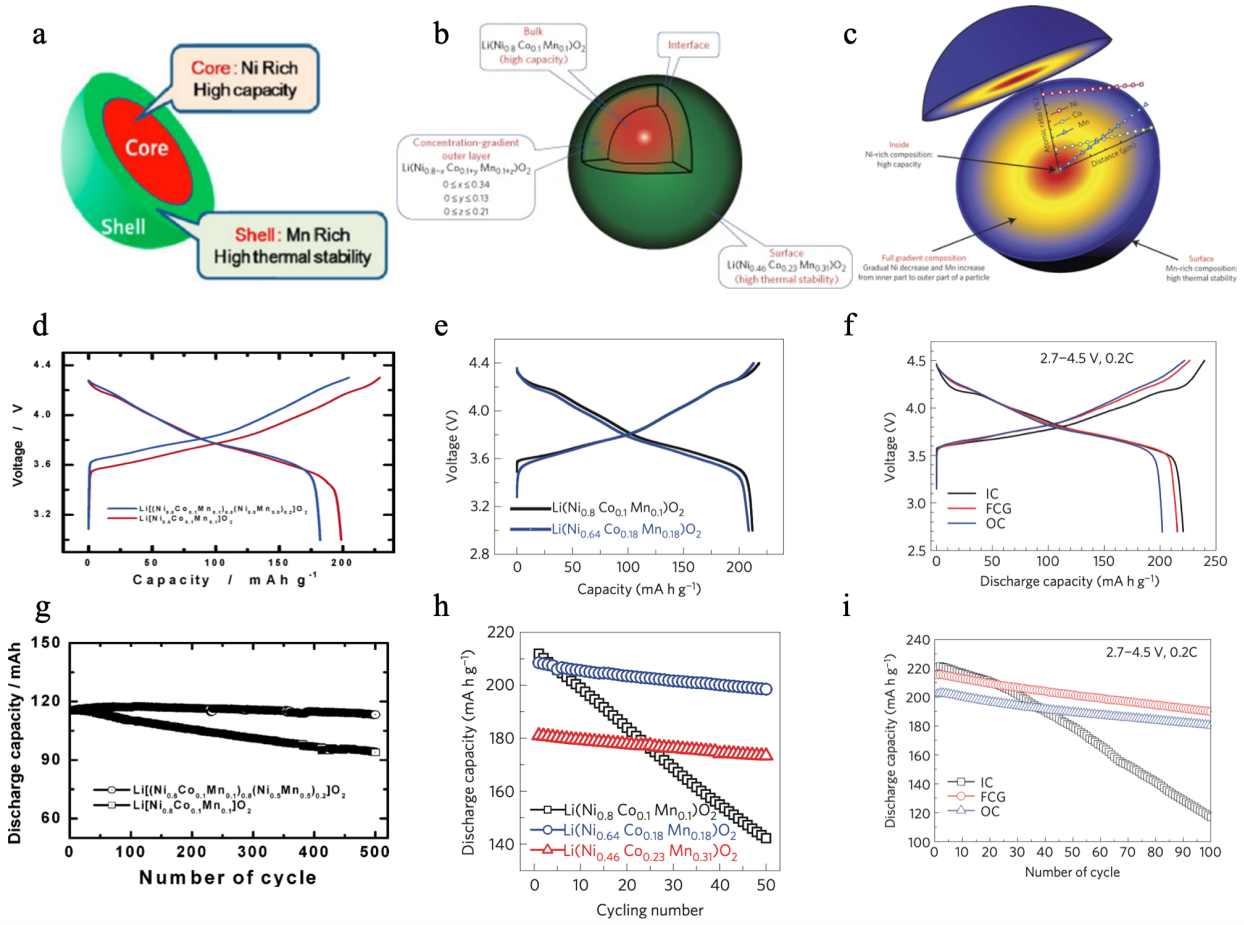

Figure 1.6. Schematic and cycle performance of (a, d, g) core-shell, (b, e, h) concentration gradient, and full (c, f, i) concentration gradient NMC designs. Provided performance is intended to show examples of design impact and are not intended to cross compare design methods as they were tested under different conditions. Adapted from *refs*. *62*, *63*, and *64*.

Clearly LR cathodes resolve tradeoffs between cost and energy density, SC resolve tradeoffs between cost and longevity, and advanced NMC gradient designs resolve tradeoffs between energy density and longevity. However, there are technical challenges to resolve and knowledge gaps to fill before they can be practically realized. In this dissertation, much work has been done to resolve the related challenges of each cathode type and advance their development. Before discussing the collected work, a general understanding of the synthesis process for these materials and how to characterize them are presented.

1.4 Cathode Material Development Process

Developing new cathode material types require an iterative process of synthesizing the material and characterizing them to understand their properties. For LR, SC, and advanced NMC materials, synthesis begins with the formation of a non lithiated precursor material. Industrial and academic synthesis typically utilizes co-precipitation in continuous stirred tank reactors (CSTR) to synthesize these precursors as they produce spherical morphologies that can lead to high levels of material density.[65] This setup (Figure 1.7a) typically includes chemical containers to feed solution, a continuous stirred tank reactor (CSTR), and programmable logic controller (PLC) to control process conditions. Although other literature sources can describe this process in more detail, at a high level co-precipitation produces TM hydroxide or carbonate complexes (e.g., $Ni(OH)_2$) by the transfer of TM ions from a source material (e.g., $NiSO_4$) to an intermediate chelating agent (e.g., ammonia hydroxide) to a precipitating agent (e.g., NaOH).[66] Co-precipitation relies on the careful balance of chemical concentration, flow rates, pH, temperature, and stirring speed as these are all factors that control precursor formation. Manipulating these parameters can tune the nucleation, growth, and ageing process that cathode precursors undergo and directly affect final cathode performance.[67] Typically, SC precursors, about 3-5 um (Figure 1.7c), will be synthesized to be smaller than LR or NMC precursors, about 10 um (Figure 1.7b) to limit particle growth during calcination, which is the second synthesis step.[57] Large size SC can face kinetic performance issues due to their long diffusion pathways.[68] Moreover, adjusting chemical feed concentration during particle growth is how advanced chemical gradients such as core-shell can be synthesized.[62-64]

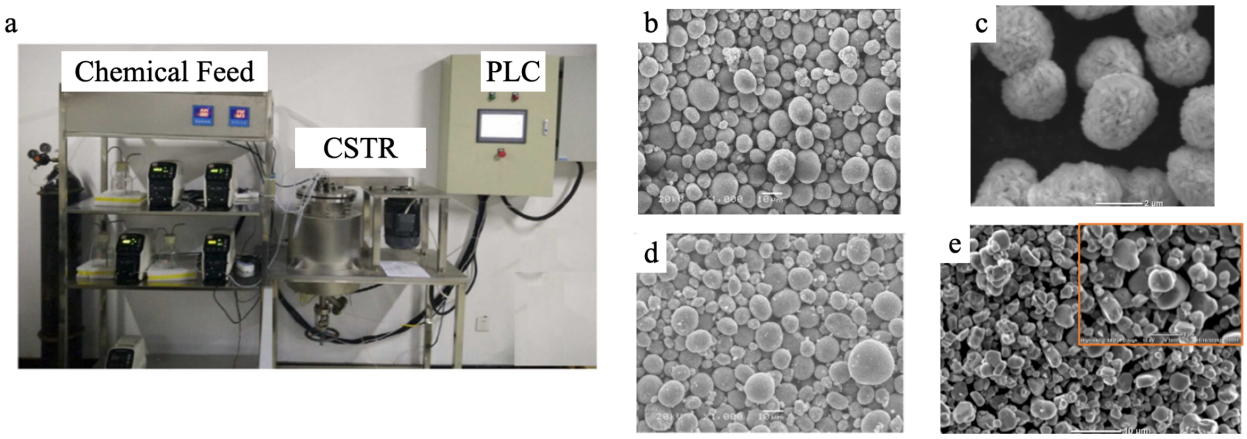

Figure 1.7. Co-precipitation for cathode precursor. (a) Photo of a standard co-precipitation synthesis setup with pumps to feed chemicals into the CSTR and PLC to monitor process parameters. (b) SEM images of $Ni_{0.6}Mn_{0.2}Co_{0.2}(OH)_2$ precursor after synthesis. (c) SC precursor after synthesis. (d) SEM images of NMC622 after calcination at 820 °C for 12 hours. (e) SC after calcination at 920 °C for 14 hours. Adapted from *refs*. *66* and *69*.

After precursor synthesis, the precursors undergo calcination to lithiate the materials and form the final oxide products (e.g., NMC).[65] When lithiated, the cathode precursors will undergo phase transitions at specific temperatures that are determined by thermodynamics. Typically, these processes will occur using solid state methods where Li content, temperature, and gas environment are key determinants for synthesizing robust cathodes with good performance. Excess Li will usually be needed to compensate for lithium volatization and evaporation that occurs at high temperature calcination.[69] When Li contents are too low, the precursor structure will be improperly lithiated and structure segregation will occur.[70] Temperature and holding time directly influence cathode material chemical structure and morphology.[65] Certain structural phases will only form after energy barriers are overcome at high temperatures and long holding times enable additional grain growth and large particle morphologies. For example, even though SC and NMC precursors are synthesized using similar processes, calcination of SC at 920 °C show single crystalline morphology, while for NMC at 820 °C polycrystalline morphology is obtained (Figure 1.7d and e).[69] This moderate gap in temperature led to drastically different morphology, which highlights

how sensitive the synthesis process can be for cathode materials. Also, the gas environment will depend on the material being synthesized, where, for example, chemistries that are more difficult to oxidize such as Ni rich will require oxidative environments statured in O_2.[71] When considered together, precursor synthesis and calcination form the core of cathode material development and determine much of the intrinsic material behavior present in the material.

Following synthesis, characterization methods are needed to investigate and understand the phenomena introduced during material synthesis or device operation. Although other literature discusses in detail specific techniques, methods, or electrochemical phenomena, at a high level the use of characterization is to understand the physical and chemical properties of a cathode material that dictate its performance.[42] These involve the use of characterization that can detail particle morphology (e.g., scanning electron microscopy, SEM), structure (e.g., x-ray diffraction, XRD and transmission electron microscopy, TEM), chemical composition (e.g., energy dispersive x-ray spectroscopy, EDS) as well as numerous electrochemical methods (e.g., dQ/dV and electrochemical impedance spectroscopy, EIS).[72] These methods can be utilized in static states (e.g., ex-situ) or in real time (e.g., in-situ), to describe cathode material phenomena at various stages of operation.[73] Moreover, the information that is obtained from these methods are largely determined by their length scale, which can range from atomic, to nano, to micro, to particle, and even electrode level length scales. It is necessary to achieve diagnostic understanding at a variety of length scales as small-scale phenomena can be hidden in bulk type tests such as XRD or electrochemical testing. In fact, a strong understanding of how these materials operate fundamentally at the atomic or nano scales can directly lead to robust solutions to improve them. As a result, efforts to utilize advanced synchrotron-based techniques to study LR, SC, or NMC materials and generate fundamental insights have increased in recent years.[74] Advanced

synchrotron tools can provide information at unprecedented resolution such as structural evolution or chemical oxidation states in a single particle and correlate them to electrochemical performance in real time.[75] Therefore, the use of these tools are instrumental in developing next generation cathode materials and have been utilized in this dissertation.

1.5 Outline of the Dissertation

With the understanding of state-of-the-art NMC, next generation cathode materials must resolve tradeoffs between cost and energy density, between cost and longevity, and between energy density and longevity. LR, SC, and advanced NMC cathode materials are ideal candidates, to address those challenges respectively. Moreover, the fundamental working principles for the synthesis and characterization of these materials may be applicable across these material types and knowledge gained from developing one material may benefit another. They all fundamentally contain lithium lattice frameworks that undergo structure evolution due to lithiation content and TM oxidation state changes that lead to structure transition. Nonetheless, specific challenges unique to each cathode need to be resolved to realize their practical use and the work discussed in this dissertation serves to resolve these knowledge gaps.

For LR cathodes, a key limitation is severe voltage fade that occurs during long term cycling. As discussed previously in literature, oxygen release was thought to be the root cause. However, methods to alleviate oxygen release such as doping or coating modifications remain ineffective during long term cycling and voltage fade is still observed. This raises the question whether oxygen release is indeed the root cause of voltage fade in the first place. In chapter 2, advanced characterization techniques such as Bragg coherent diffraction imaging (BCDI) and electron 3D electron diffraction (3D rED) are utilized to diagnose nanoscale material phenomena that are not visible in bulk characterization methods. The novel use of these methods on LR have

identified for the first-time the fundamental strain behavior and structure evolution in LR composite structures with different redox activity (e.g., $LiTMO_2$ and Li_2MnO_3). This understanding enables new development strategies and resolves the knowledge gap limiting LR, which is a step to overcoming tradeoffs between cost and energy density.

For SC, a Co free SC is investigated in chapter 3 utilizing advanced synchrotron x-ray microscopy and nano diffraction techniques. Co free SC are attractive as they can resolve the tradeoffs between cost and longevity, as well as enable practical use of SC. However, literature reports on the impact of Co removal in SC is lacking, while for NMC, studies have even suggested that Co removal is beneficial to performance at high voltages. By using advanced techniques in this dissertation, it was found that LR nano domains form in SC after the removal of Co and electrochemical performances are worsened. The electrochemical performance deterioration was clearly linked to strain evolution and voltage fade that arose from the formation of the LR nano domains. As a result, it is possible that cobalt removal from SC is not viable and that there will be tradeoffs between cathode material cost and longevity. Nonetheless, these insights reveal for the first time a key challenge facing Co free SC, whereby strategies can now be developed to resolve it.

In chapter 4, the findings obtained from LR and SC investigation are utilized to develop a cathode material that can resolve the tradeoff between energy density and longevity. Unlike previously reported chemical gradient designs, a multi structure nickel manganese cobalt oxide cathode (MS-NMC) is proposed, synthesized, and characterized using advanced methods. MS-NMC design emphasizes spatial control of material structure and chemical composition, as opposed to only chemical composition in chemical gradient designs, to resolve the intrinsic structural limitations of layered NMC. By integrating layered NMC with other structures that are

intrinsically more stable at higher voltages, the intrinsic weakness of prior chemical gradient methods can be overcome. These other structures, namely LR and DRX, contain moderate to high contents of Li and TM site exchange, which forms pillar structures that improve structure stability during cycling. However, when Li disordering is severe as in the case of DRX, kinetic performances are reduced, and achievable energy densities are reduced. Therefore, NMC, LR, and DRX cathode types contain strengths and weaknesses that balance each other, and a spatially controlled cathode design would be able to leverage them to achieve robust performance. When tested, MS-NMC outperformed state of the art NMC and validated the new design concept, which can also be applied to the development of other cathode chemistries.

Finally in chapter 5, the results of this dissertation are summarized and an outlook on the development of next generation cathode materials is discussed. Collectively, the development efforts discussed in this dissertation on LR, SC, and MS-NMC materials detail incremental progress to the realization of next generation cathode materials that resolve tradeoffs between cost and energy density, cost and longevity, and energy density and longevity. Resolving these tradeoffs can enable cheap BEV with long driving range, which accelerates consumer adoption and promotes the transition to sustainable energy.

Chapter 2

Origin of Structural Degradation in Li-rich Layered Oxide Cathode•

Abstract

Voltage fade prevents effective use of the excess capacity and represents the most crucial technical challenge faced by Li- and Mn-rich cathode materials (LMR) in modern batteries. Although oxygen release has been arguably considered as an initiator for the failure mechanism, its prerequisite driving force has yet to be fully understood. Herein, relying on the *in-situ* nanoscale sensitive coherent X-ray diffraction imaging (BCDI) technique, we are able to track the dynamic structure evolution of the LMR cathode. The results, surprisingly, reveal that continuous nanostrain accumulation arose from lattice displacement during cell operation is the original driving force for detrimental structure degradations together with oxygen loss that triggers the well-known rapid voltage decay in LMR. By further leveraging primary to multi-particle structure and electrode-level as well as atomic scale observations, we demonstrate that the heterogeneous nature of the LMR cathode inevitably causes pernicious phase displacement which cannot be eliminated by the previous trials. With these fundamental discoveries, we propose the mesostructural design strategy to mitigate the lattice displacement and inhomogeneous electrochemical/structural evolutions, thereby achieving stable voltage and capacity profiles. These findings highlight the significance of lattice displacement in voltage decay mechanism and will inspire a wave of efforts to unlock the potential of the broad-scale commercialization of LMR cathode material.

• This work was originally reported in *Nature* **2022**, 606, 305-312.

2.1 Introduction

Li and Mn-rich cathode materials (LMR) that utilize both cation and anion redox are among the very few options available to yield substantial increases in battery energy density. However, voltage decay issues cause continuous energy loss and restrains the development of the battery management system, the Achilles' Heel of this promising cathode material that impedes its broad-scale commercialization.[76-79] While several prevailing theories have been established for voltage fade, including transition metal (TM) migration, TM valence state reduction and irreversible phase transitions, they are eventually attributed to thermodynamic instability of lattice oxygen and to oxygen release.[80-84] Prior research efforts have also sought diverse solutions to premeditatedly enhance lattice oxygen stability, however, the effectiveness of these strategies is limited and it remains unresolved so far.[85-87] This predicament raises the suspicion of whether thermodynamic instability is the governing prerequisite for voltage decay in the LMR cathode.

In conventional intercalation cathodes, Li ion (Li^+) movement in/out of its host framework will drive dynamic structural evolution, which directly affects structure stability and electrochemical profiles.[49,88-90] Unfortunately, uneven Li^+ (de)intercalation and heterogeneous electrochemical reactions often occur in these cathodes, leading to nonequilibrium structural dynamics at both the macroscopic and microscopic level.[91-92] The former is manifested as the anisotropic volume variation and bulk mechanic strain that have been broadly viewed as the root cause of mechanical degradation, such as secondary particle cracking.[59,93] The latter contributes to nanoscale strain with less detectable lattice displacement,[94] while their destructive effects on topical structure stability remain unclear. This is particularly significant for LMR cathode because its heterogeneous structure is composed of two structurally coherent nano-domains ($LiTMO_2$ and Li_2MnO_3) that are electrochemically activated in separate voltage ranges with different redox

chemistries.[95-97] It is such heterogeneous structural dynamics of nano-domains that determines the global generation of nanoscale strain that can substantially alter the structure stability and aggravate oxygen release.

Despite its fundamental importance, lattice displacement and nanoscale strain are probably the least understood structural properties in battery materials. Due to technical limits faced in the past, characterization tools could not penetrate into nanoscale regimes, preventing the observation of lattice displacement and the analysis of nanoscale strain.[74] This is even more challenging to monitor the spatial strain evolution under operando conditions.[92,98,99] Clearly, building a mechanistic link between nanoscale structure dynamic and electrochemical property requires systematic investigations spanning multiple length scales, which benefits to unity the prior electrochemical degradation mechanism of LMR and guide effective approaches to mitigating voltage fade.

Herein, we conduct a comprehensive investigation of nanoscale lattice evolution in LMR cathode, revealing that lattice displacement and the resulting nano-strain are the root cause of oxygen release prior to thermodynamic destabilization. By leveraging the combination of *in-situ* nanoscale sensitive coherent X-ray diffraction, 3D rotation electron diffraction, and multi length scale X-ray diffraction techniques, we identify the heterogeneous nature of LMR as the prerequisite for severe lattice displacement and the resulting nano-strain upon Li^+ (de)insertion. Subsequently, continuous strain accumulation in nanoscale domains serves as the original driving force triggering oxygen loss and detrimental structure degradation, which eventually results in rapid voltage fade. Our results affirm that lattice displacement and nano-strain, which represent commonly occurred but less detectable dynamic structure evolutions, play an undeniable role in structure decomposition and voltage fade. Benefitting from these fundamental discoveries, we

propose to mitigate the voltage degradation of LMR with O2 phase-based cathode or a whole-voltage-range oxygen redox cathode that can effectively eliminate inhomogeneous reactions and suppress strain generation. These findings provide more effective structural strategies for preventing oxygen release and solving the long-standing voltage fade issue.

2.2 Results and Discussion

2.2.1 Initial Structure and Electrochemical Properties

A representative LMR cathode with $Li_{1.2}Ni_{0.13}Mn_{0.54}Co_{0.13}O_2$ was synthesized by a classical sol-gel method.[97] Its morphology and composition details are described in the Method section and Figure A.2.1-2.4. The X-ray powder diffraction (XRD) measurement (Figure 2.1a) shows identical result as reported in the literature.[96, 97] Characteristic super-reflections present in the 2θ region of 1.4 to 2° correspond to Li/Mn ordering in the TM slabs (Li_2MnO_3-like phase). The detailed structure information can be found in Table A2.1.

Aberration-corrected scanning transmission electron microscope (AC-STEM) is applied to directly visualize the spatial distribution of $LiTMO_2$ and Li_2MnO_3 domains. Figure 2.1c illustrate a typical layered structure with two types of bright spot arrangement. Those with regular "bright-bright-dark" arrangements are identified as Li_2MnO_3 domains, which are characterized by the well-known honeycomb Li-Mn ordering. The others with no distinguished dark spots in the bright spot columns are identified as $LiTMO_2$ domains. It is clear that $LiTMO_2$ domains are three-dimensionally incorporated into the Li_2MnO_3 lattice without obvious interphase boundaries, indicating that these two phases are randomly mixed and share the coherent lattice structure.

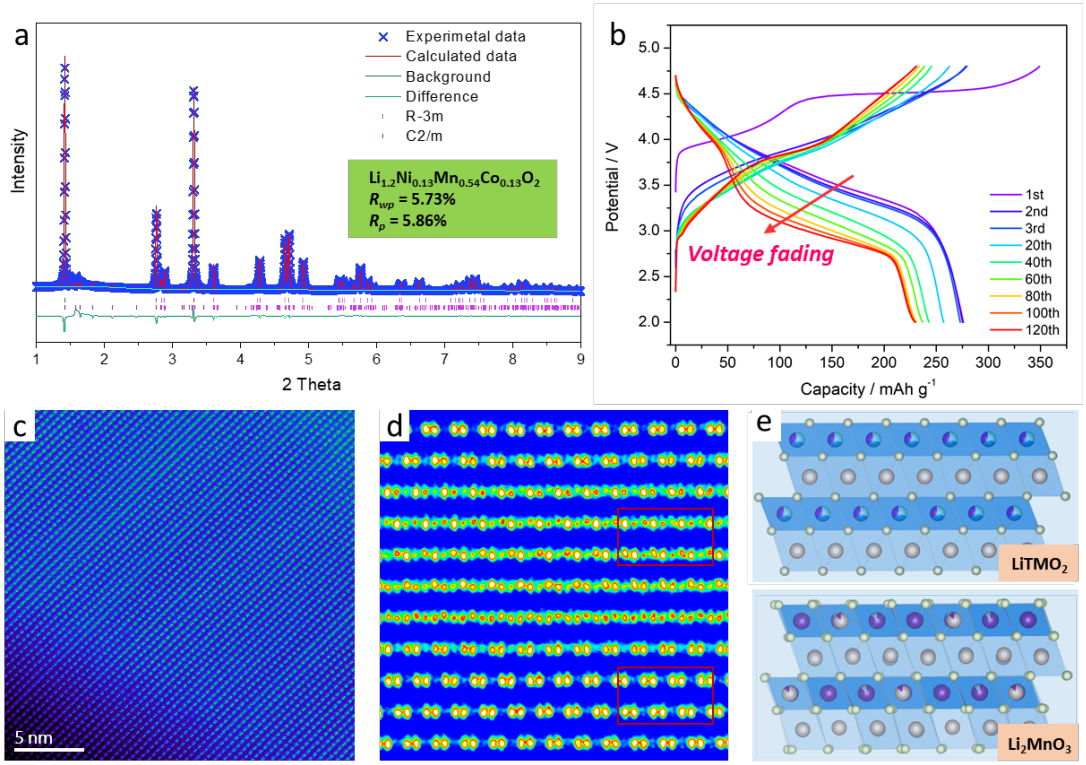

Figure 2.1. Electrochemical profile and initial structure of the LMR cathodes. (a) The XRD pattern and Rietveld refinement results of LMR. (b) Charge / discharge curves of the LMR within a voltage range of 2.0-4.8V at 0.1C rate current. (c) High resolution TEM image showing the atomic arrangements of LMR. (d) Enlarged figure of the selected area of Figure 2.1c. (e) Schematic structure of $LiTMO_2$ domains and Li_2MnO_3 domains

The electrochemical profile of the LMR shows a high discharge capacity of 273 mAh g^{-1} (Figure 2.1b), which is very competitive against the current commercial cathode materials with high Ni content.[24,100] Notably, two distinct electrochemical stages at different voltage ranges were observed from the first charge profile (Figure A.2.5 and Figure A.2.6). Stage 1 is attributed to the activation of $LiTMO_2$ domains associated with the oxidation of Ni and Co ions.[101] Stage 2 at a plateau voltage over 4.47 V corresponds to the activation of Li_2MnO_3 domains, where lattice oxygen is oxidized with accompany of oxygen release usually.[102,103] The electrochemical profile confirms the differential electrochemical activities of these two structurally coherent domains. Galvanostatic Intermittent Titration Technique (GITT, Figure A.2.7) demonstrates that Li ion diffusion coefficient keeps stable in stage 1 but dramatically decreases after the activation of

Li_2MnO_3 domains (stage 2), indicating that reaction kinetics involved in TM redox and oxygen redox are also significantly different. Despite its attractive capacity, the LMR cathode typically suffers from rapid voltage fade and capacity loss concurrently during cycles, which causes a substantial loss of energy density and the invalidation of the battery management system.

It is argued that the electrochemical degradation mechanism is closely related to the synergy of structure decomposition and oxygen release.[101] However, the prerequisite driving force of these detrimental reactions remain ambiguous. Previous studies also argued that oxygen-related gas stems from the activation of thermodynamically unstable Li_2MnO_3 domains.[101,104] Paradoxically, recent density functional theory (DFT) calculation results demonstrate that oxygen release is thermodynamically unfavorable in the initial delithiation of the pure Li_2MnO_3.[105,106] To clarify the uncertainty shrouding oxygen release, we carefully measure the gas evolution of Li_2MnO_3 upon the first charge under operando condition. The synthesis and morphology details can be found in Figure A.2.8-2.10. The differential electrochemical mass spectrometry (DEMS) result shows that oxygen-related gas is absent at the initial activation of Li_2MnO_3 around 4.5 V (less than 20% delithiation) and started to be detected over 20% delithiation of Li_2MnO_3. This result provides direct evidence that the activation of pure Li_2MnO_3 material is not the root cause of oxygen release. Consequently, oxygen release mechanism of LMR cathode cannot be solely attributed to the activation of Li_2MnO_3 domains and its thermodynamic instability. This also explained why the previous effort to improve oxygen stability of LMR cathodes fails to solve the voltage fading issue. The interaction between Li_2MnO_3 and $LiTMO_2$ is critical for oxygen release but it seems to be overlooked previously. In light of the fact that the $LiTMO_2$ and Li_2MnO_3 domains share a coherent lattice at the nanoscale but exhibit differentiated electrochemical activities due to different redox chemistries, such heterogeneous electrochemical reactions will lead to

nonequilibrium structural responses, which may be reflected by lattice displacement and nanoscale strain in the bulk structure. This is particularly important for the failure mechanism understanding of the LMR cathode but was rarely investigated due to the characterization limit.

2.2.2 Strain Evolution of the Single LMR Particle through BCDI

The Bragg coherent X-ray diffraction imaging (BCDI) is an indispensable tool to visualize structural, morphological and lattice strain information in electrode materials under operando conditions.[94,107,108] Hence, in-situ BCDI measurements are performed to monitor lattice displacement and analyze strain evolution of the LMR primary particle during electrochemical reactions. The experimental setup is illustrated in Method section. These 3D diffraction patterns of the [003] reflection is analyzed using a combination of the Error Reduction and the Hybrid Input/Output algorithms to reconstruct the 3D structure and the lattice displacement along the momentum transfer direction, which is the particle *c*-axis here. Henceforth in this work, we will refer to images if this lattice displacement as generic "strain" although it is technically an integral of strain.[94]

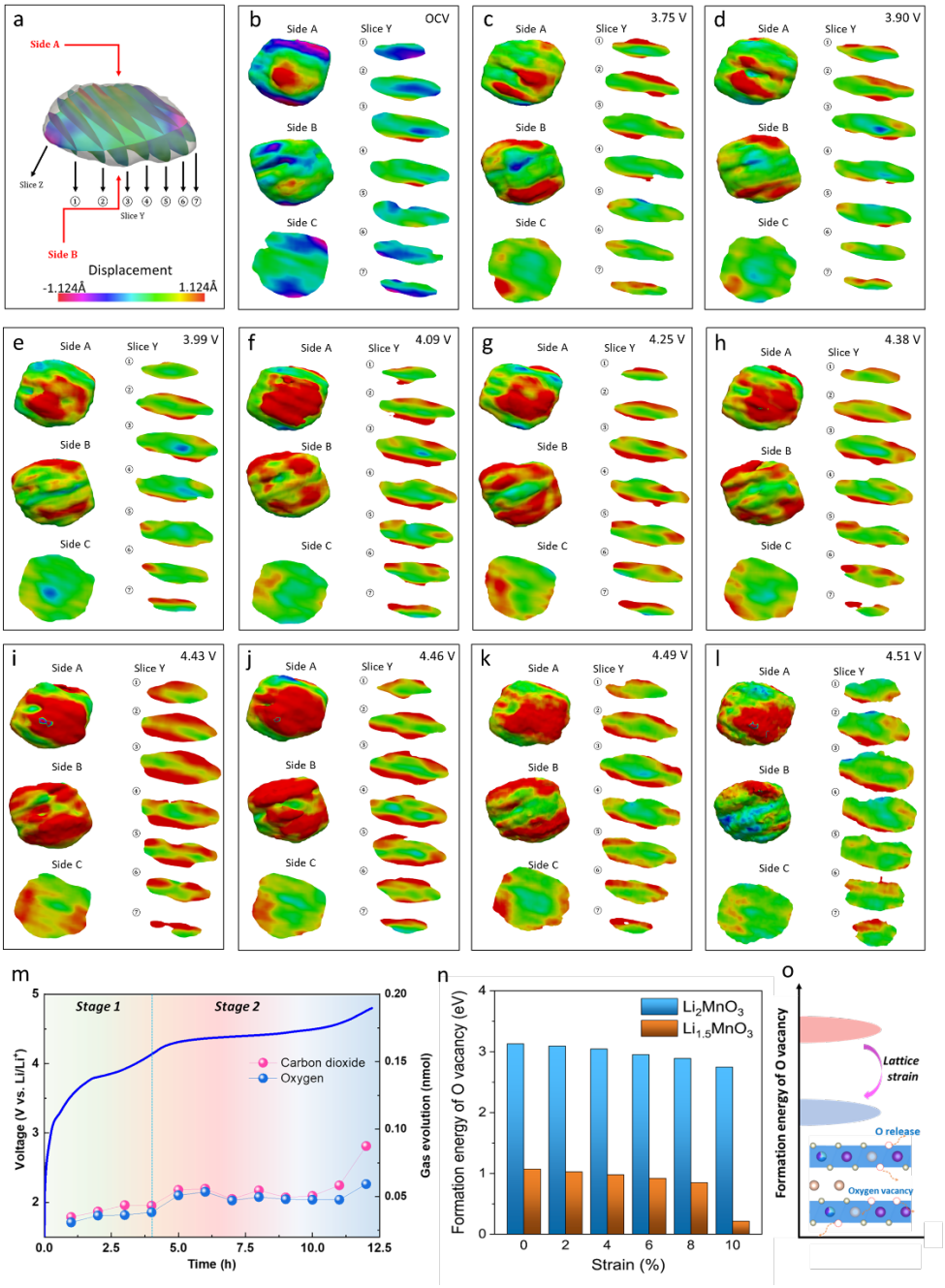

Figure 2.2. Strain evolution of the LMR and its relationship with oxygen release. (a-l) In-situ BCDI images of the 3D LMR particle in the strain field, measured at 3.2 V (Open circuit voltage, OCV), 3.75 V, 3.90V, 3.99V, 4.09 V, 4.25V, 4.38V, 4.43V, 4.46V, 4.49V and 4.51V, respectively. The strain evolution in each state is detailed by the spatial location of the slices along the Y axis. (m) In-situ differential electrochemical mass spectroscopy measurements for LMR. (n) Formation energy of O vacancies in Li_2MnO_3 and $Li_{1.5}MnO_3$ when tensile strains are applied. (o) Schematic illustration of the influence of lattice strain on O release.

In Figure 2.2a, to demonstrate the spatial lattice evolution, the reconstructed LMR primary particle is displayed as three-dimensional cross-section images, in which the compressive and tensile strains are expressed by blue and red, respectively. In the pristine stage (Figure 2.2b), we observed the concurrent appearance of both compressive and tensile strain. We believe these initial strains are due to local Li aggregation and vacancies caused by high temperature sintering process. The initial strain gradually disappears with initial delithiation as rearrangement of Li occupancies in Li layers (Figure 2.2c). When entering the first voltage slope around 3.9V (Figure 2.2d), a tensile strain begins to present itself on the particle surface. As discussed above, the initial Li extraction predominately occurs in the $LiTMO_2$ domains and results in local lattice expansion. The lattice expansion is partly confined by the inactive Li_2MnO_3, which results in tensile strain at nanoscale. The tensile strain occurs preferentially near particle surface area which makes sense since Li extraction starts there. With continuous Li extraction, the tensile strain gradually accumulates and extends into the interior of the particle (Figure 2.2e-h). At the end of stage 1 (4.43V), where almost all $LiTMO_2$ domains are fully delithiated, the electrostatic repulsion between oxygen layers reached the maximum, resulting in the global existence of tensile strain in the entire particle (Figure 2.2i). Therefore, undergoing such inhomogeneous Li concentration and accumulated tensile strain severely affects the structural stability of the composite LMR, which may trigger the decomposition of Li_2MnO_3 domains.

Interestingly, the lattice strain evolution reverses once entering stage 2. Figure 2.2j shows the tensile strain started to decrease at 4.46 V, which is considered as the starting voltage of the Li_2MnO_3 domains activation and the onset of O_2 release. To verify this, *in-situ* DEMS is carried out to measure the gas generation during the first charge. Figure 2.2m shows oxygen-related gas is not evolved in stage 1. Once entering stage 2, the onsets of O_2 and CO_2 signals are

simultaneously observed, which is exactly consistent with strain changes mentioned above.[109] The overall tensile strain gradually decreases with oxygen release in stage 2, until the particles disappeared from the detection field at 4.51 V (Figure 2.2k and l). As a consequence, the correlation between lattice strain evolution and oxygen release is naturally established. The inhomogeneous electrochemical kinetics of two domains results in globally existed tensile strain in coherent lattice and tremendous inhomogeneity of Li^+ concentration, which will accelerate the decomposition of Li_2MnO_3 and trigger oxygen release. After oxygen release, the confined lattice expansion relaxes and in turn leads to the decrease of lattice strain. This argument is further supported by the results of the DFT calculation. Figure 2.2n and o indicates the energy barriers to remove lattice oxygen will be significantly reduced when the increased lattice strain is applied to the Li_2MnO_3 domains.

2.2.3 Origin and Relaxation of Tensile Strain in the LMR Cathode

To build the mechanistic link between lattice displacement/nanostrain and electrochemical reaction, systematic structure characterization spanning multiple length scales were performed to investigate structure evolution of LMR cathode during the first cycle (Figure 2.3a). Firstly, the *in-situ* coherent X-ray multi-crystal diffraction technique (CMCD) is applied to monitor the minuscule phase evolutions of LMR cathode during operando operation.[109] With just tens of particles giving diffraction signals, CMCD can record semi-statistical information on the structure transmissions of LMR particles and the response of individual crystals that are typically not visible in conventional XRD. This technique benefits from a unique vision between the macroscopic and the microscopic and fills in the capability gap between conventional XRD and BCDI. As can be seen in Figure 2.3b, the Debye-Scherrer ring of the (003) peak is selected to track the structure evolution and lattice changes, which is consistent with the reflection of BCDI. The image captured

at OCV shows a single ring composed of a series of bright diffraction spots (D_1) that corresponds to the *c-axis* reflection of tens of primary particles. Since the single-phase reaction of $LiTMO_2$ domains is below 4.47 V, there is no obvious change to the diffraction ring. When the battery was charged to 4.472 V that corresponds to the initial voltage of oxygen release, a bright diffraction spot appears at a smaller angle (D_2), which suggests that part of a particle undergoes lattice expansion with oxygen release. This reaction should be attributed to the activation of Li_2MnO_3 domains and lead to the relaxation of confined lattice expansion. Further charging to 4.484 V leads to more diffraction spots moving towards smaller angle. At the later stage of the O-redox plateau, these diffraction spots integrate to a clear powder ring (D_2) at 4.562 V. The powder ring of D_2 keeps intensifying along with the charging and its intensity reaches the maximum at 4.8 V. Meanwhile, the original powder ring (D_1) weakens as the new powder ring intensifies.

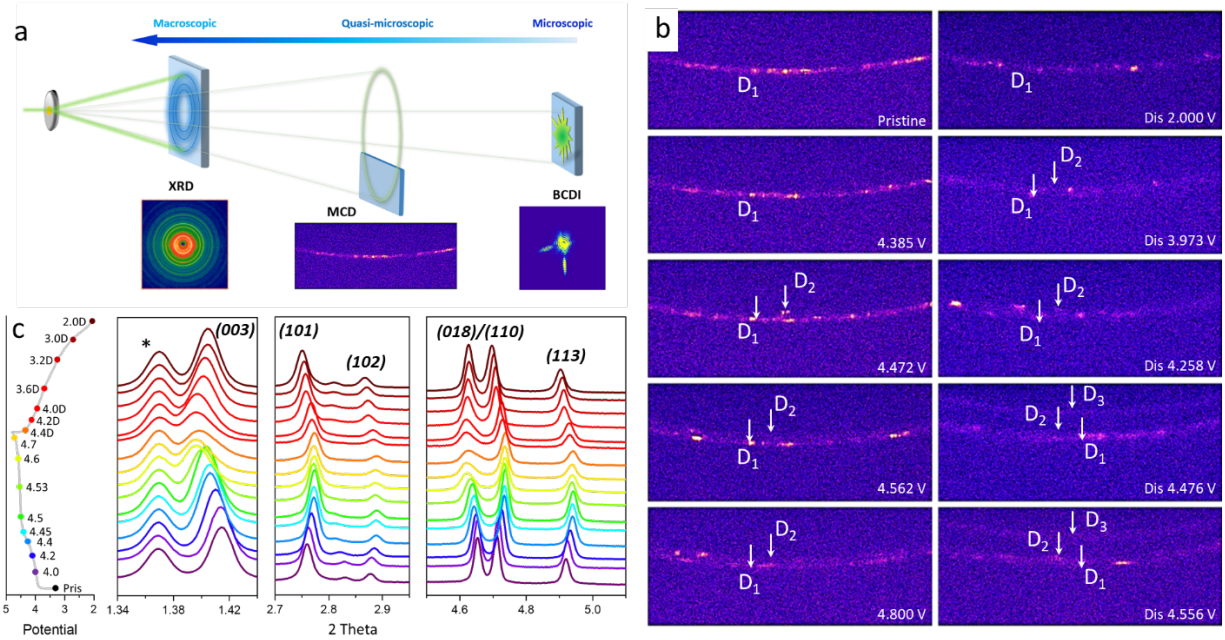

Figure 2.3. Multiscale X-ray diffraction techniques used to investigate the structure evolution of the LMR cathode. (a) Schematic of multiscale X-ray diffraction techniques used in this work. (b) *In-situ* CMCD for the (003) peak along with charge and discharge curve of the LMR cathode. Bright spots in the left figure show initial multi crystal diffraction corresponding to tens of particles. D_1, D_2 and D_3 correspond to three lattice distances. (c) *Ex-situ* HEXRD of the LMR cathode measured at different potentials. The peak marked by * comes from the PTFE binder.

The CMCD results clearly reflects the inhomogeneous lattice expansion behavior of the LMR cathode during the first charge. In stage 1 (below 4.472 V), due to the surrounding inactive Li_2MnO_3 domains, the lattice expansion is partly confined and only presents one diffraction ring. Such inhomogeneous structure evolution of two domains is the primary cause of the tensile strain observed in the BCDI images. As tensile strain gradually reaches the limit, the Li_2MnO_3 domains is struggling with the imposed lattice strain and Li^+ concentration imbalance, which subsequently triggers the decomposition of Li_2MnO_3. The confined lattice expansion is released naturally with the activation of Li_2MnO_3 domains, leading to the relaxation of tensile strain. With more Li_2MnO_3 domains decomposing in the following charging process, a growing number of lattices are liberated and expand along the c axis, which is reflected in the brighter spots appearing in the second diffraction ring (D_2). In the end of charge (4.8 V), the intensity of D_2 reaches the maximum, suggesting most of Li_2MnO_3 domains are "activated".

During the discharge process, the reflection in the CMCD images converts back to the original single diffraction ring (D_1) via the converse sequence of structure transitions. Interestingly, in addition to D_2 and D_1 rings, another weak diffraction ring (D_3) is visualized in even smaller diffraction angle at the very beginning of discharge. This diffraction ring can be indexed to the (101) crystal plane of $Li_2Mn_2O_4$, which is considered to be the phase formed by the overlithiation of spinel $Li_xMn_2O_4$. This observation implies that transition metal migration to Li layers occurs with oxygen release and $Li_xMn_2O_4$ spinel-like phase forms in the first charge. The diffraction ring of D_3 only appeared in the first 10 minutes of discharge (vs. a total of 10 hours discharge time), which suggests the $Li_2Mn_2O_4$ is a kinetic-dependent intermediate phase. In this sense, we infer that those $Li_xMn_2O_4$-like spinel domains are most likely concentrated on the particle surface that are momentarily over-lithiated to form $Li_2Mn_2O_4$ due to the high Li ion

concentration and poor Li diffusion of the surface at the beginning of discharge. As lithium ions gradually migrate to the bulk, the over-lithiated $Li_2Mn_2O_4$ gradually change to $LiMn_2O_4$, whose diffraction ring is very close to D_1 and D_2. Thus, the diffraction ring of D_3 accordingly disappears with surface Li^+ concentration equilibrium.

Concurrently, high-energy in-situ and ex-situ XRD was further conducted to macroscopically investigate the correlation between structural evolution and electrochemical properties. As seen in Figure 2.3c and Figure A.2.12-2.13, (003) peak shift towards the lower diffraction angle before 4.45 V, which is associated with the lattice expansion induced by $LiTMO_2$ domains. When charged to 4.45 V, corresponding to the beginning voltage of oxygen release, obvious (003) peak broadening started to be visualized, indicating that the confined lattice expansion is released with the decomposition of Li_2MnO_3 domains. These statistical observations of structure evolution are consistent with the appearance of the second diffraction ring (D_2) in the CMCD images. At the same time, the disappearance of the superlattice peak over 4.5 V (Figure A.2.12) suggests that TM migration must occur with oxygen release and the TM ordering is broken. This argument is further supported by the *ex-situ* extended X-ray absorption fine structure (EXAFS) and the fitting results. Figure A.2.14 and Table A.2.2 show that the coordination number of Mn-O evidently decreases but that of Mn-TM increases accordingly. This again confirms that lattice strain accumulation will trigger TM migration and oxygen release. More importantly, the broadening and weakening of a series of peaks are found to be mainly related to *c* axis, such as (003), (104), (107) and (108) peaks (Figure 2.3c and Figure A.2.12). The oriented peak broadening is due to more inhomogeneous lattice changes mainly occurring along the c-axis during charge/discharge, which further confirmed that strain evolution stems from the heterogeneous nature of LMR cathode.

2.2.4 Atomic Observation of Lattice Displacement and Chemical State Evolution

To visually investigate the lattice displacement and nanostructure evolution, transmission electron microscope (TEM), 3D rotation electron diffraction (3D-rED) and electron energy loss spectroscopy (EELS) are performed on the delithiated samples. As mentioned above, the inhomogeneous electrochemical activities and structure evolution of two domains result in nanoscale strain. In the microscopic vision, strain is manifested as lattice displacement, which can be captured by a high resolution TEM. Figure 2.4a-c and Figure A.2.15 show that although layered structure is maintained at 4.47 V, obvious lattice displacement presents on the surface and the bulk as well. For example, the lattices in the marked areas are deformed significantly. Likewise, more obvious displacement occurs on the surface with constant lattice twist (Figure 2.4c), which should be attributed to the concentrated strain on the surface.

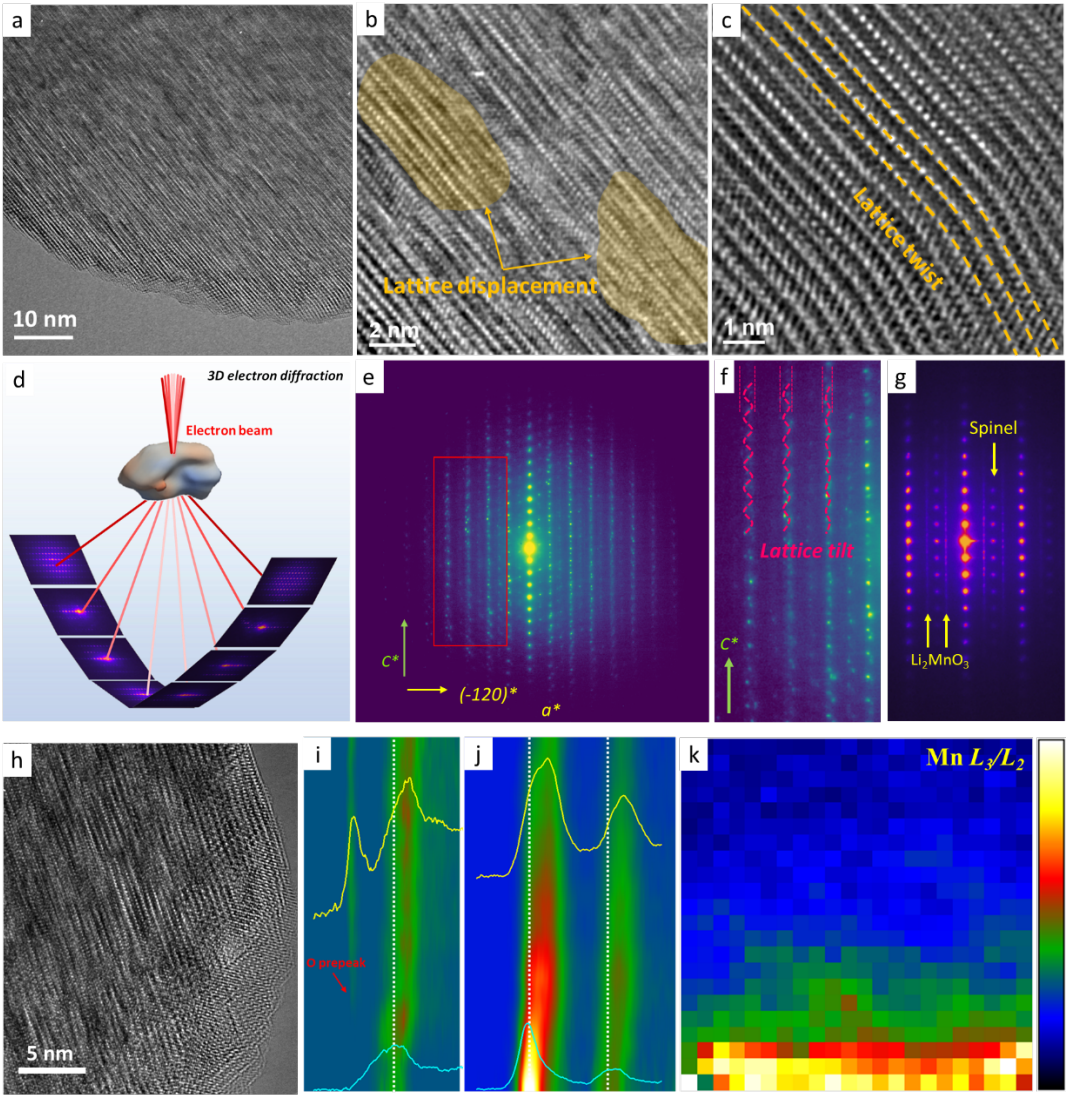

Figure 2.4. Visible observation from atomic-level TEM, 3D electron diffraction and chemical state analysis from EELS. (a) Low magnification TEM image of the LMR cathode charged to 4.47 V. (b) Enlarged image of the selected area of Figure 2.4a. (c) High resolution TEM image of the LMR surface. (d) Schematic of the data collection process of 3D-rED. (e) Reciprocal lattice along the *b** axis of LMR. (f) Enlarged figure of the selected area of Figure 2.4e. (g) SAED image of delithiated sample (4.5V) at a certain angle of rotation. (h) Low magnification TEM image of the LMR cathode charged to 4.8 V. (i and j) EELS line-scan of O *K*-edge and Mn $L_{2,3}$ edge of the LMR cathode charged to 4.8 V. (k) 2D EELS mapping of Mn K-L_3/L_2. The high value and low value colored by red and navy blue corresponds lower and higher valance state of Mn, respectively.

When entering stage 2, a continuous delithiation is accompanied by oxygen release together with the activation of Li_2MnO_3 domains. The same observation is conducted to track the lattice changes after Li_2MnO_3 activation. Figure A.2.16-2.17 demonstrates that beside lattice

displacement, a phase transition from layered structure to spinel phase occurs in this stage (4.5V). The lattice evolution in a larger scale were further investigated by 3D-rED in reciprocal space that recently was applied to study battery materials (Figure 2.4d and Figure A.2.18-2.19).[111] The experimental details can be found in the Method section. Figure 2.4e-f and Figure A.2.20 illustrate that obviously twisted reflections along the *c* axis is observed in the reconstructed discrete reciprocal lattice. These twisted diffraction points could be attributed to the lattice displacement observed in the high resolution TEM. Structure identifications are analyzed using the selected area electron diffraction (SAED). As shown in Figure 2.4g and Figure A.2.21, in addition to typical layered structure and weak Li_2MnO_3 reflection, we also observed the reflection that corresponds to spinel lattice. This further confirmed the severe lattice strain will trigger transition metal migration and structure transition from layered phase to spinel phase. These observations are in good agreement with the structure evolution captured by CMCD.

TEM combining EELS is used to precisely probe the structural and chemical variation of the fully delithiated sample (4.8 V). As shown in Figure 2.4h and Figure A.2.22, TEM again confirms the occurrence of structure transition, especially on the surface of the particle. A clear reconstruction surface layer with spinel and rock-salt phase is the direct evidence of transition metal migration and irreversible phase transition after oxygen release. EELS line profiles of O-*K* edge and Mn-$L_{2,3}$ were stacked in Figure 2.4i, j and Figure A.2.23 along the bulk to the surface. The intensity of O-*K* edge prepeaks substantially reduces from the interior to the exterior and almost disappears near the surface. Likewise, the O-*K* line-scan parallel to the surface (Figure A.2.24) further confirms that the oxygen release uniformly occurs in the entire particle surface as the O prepeak disappears. It is worth noting that the oxygen release predominately occurs near the surface, where the strain evolves most drastically during the first charge, verifying that strain

accumulation is the root cause of oxygen release. Concurrently, Mn *L* edge shows left shift near the surface (Figure 2.4j). 2D EELS mapping further reverts the chemical state change of Mn in the whole particle (Figure 2.4k). It is evident that the surface reconstruction layer shows a relatively lower Mn valance than the bulk, which suggests that Mn oxidation state decreases occur with its migration and oxygen release near the surface. Based on the above observation, the oxygen release and transition metal migration occur preferentially in regions where the structure suffers from severe lattice strain, suggesting that these destructive reactions are primarily rooted in lattice displacement.

2.2.5 A Prospect for the Future Development of Li- and Mn-rich Cathode Materials

The prevailing theories established for the voltage fade are thermodynamic instability of structure with the tendency to oxygen release and progressive structural rearrangement involving TM migration and irreversible phase transitions.[88, 111] However, there are significant confusions over these aspects. First, the presumption that thermodynamic instability triggers oxygen release is not supported by DFT calculation results.[105,106] Although the fact that oxygen release or oxygen vacancies extensively generate in the bulk and dominate the rapid structural/electrochemical degradation has been recognized recently, the original driving force of oxygen release of the LMR cathodes remains unclear.[112,113] In addition, TM migration and irreversible phase transition is limited near surface area from TEM observation and invisible in the macroscopic characterizations.[114-116] This calls into question whether such local structural degradation can undermine the overall electrochemical behaviors. In this work, we dig into the dynamic nanostructure evolution and the local interaction of the domain structures, which are not accessible previously. Combining the multiscale characterizations and DFT calculation, we revealed that lattice displacement induced by nonequilibrium structural dynamics is the root driving force of

voltage fade. More importantly, nanoscale strain evolution provides a plausible explanation for the origin of oxygen release and TM migration, unifying previously proposed theories for voltage fade.

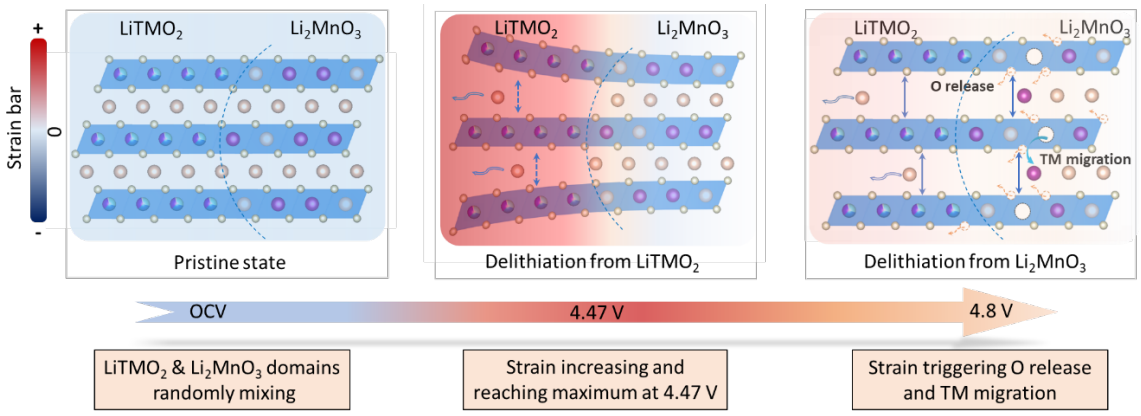

Figure 2.5. Schematic of the correlation of strain generation and O release as well as transition metal migration. The $LiTMO_2$ and Li_2MnO_3 domains share a coherent lattice at the nanoscale but exhibit differentiated electrochemical activities due to different redox chemistries. The initial Li extraction predominately occurs in the $LiTMO_2$ domains and results in local lattice expansion. The lattice expansion is partly confined by the inactive Li_2MnO_3, which results in tensile strain at nanoscale. The accumulated tensile strain severely affects the structural stability of the composite LMR, which may trigger the decomposition of Li_2MnO_3 domains, oxygen release and transition metal migration. The activation of Li_2MnO_3 and oxygen release in turn release the lattice strain at high voltages.

A strain-induced structure degradation mechanism is detailed in the schematic image (Figure 2.5). In general, the different electrochemically reactivities but coherent lattice structure of two domains constitutes a prerequisite for lattice strain. The activation of $LiTMO_2$ increases local electrostatic repulsion with a tendency of lattice expansion. Due to the inactive O redox of the Li_2MnO_3 domains at low potentials, their lattice expansion is partly confined, resulting in severe nanoscale strain with lattice displacement. Lattice strain initiates from the particle surface, gradually extends into the bulk of particle with continuous delithiation and reaches the maximum when the $LiTMO_2$ domains are almost fully delithiated. The extreme strain imposed on the particles substantially decreases the structural stability, triggering the decomposition of Li_2MnO_3

and oxygen release. As the Li_2MnO_3 domains are activated, the imposed lattice expansion is naturally released and tensile strain relaxes synchronously. Likewise, oxygen release significantly lowers the energy barrier of transition metal migration, resulting in irreversible phase transition.[117] Such strain evolution would adversely accumulate on long-term cycling, and eventually lead to structural degradation and fast electrochemical decay.

The above mechanism demonstrates that the lattice strain of the LMR cathode originates from the heterogeneous composite structures and differential electrochemical activities. Thus, post-treatments such as surface engineering methods show little effectiveness towards voltage decay. Resolving this issue must fundamentally consider composition design or local structure regulation. Following this concept, practical approaches to tackle lattice strain are to solve the heterogenous structures of two compositions in the LMR cathodes and their differential electrochemical activities. Since it has been proven challenging to alter the domain mesostructure of the O3 type-LMR, we attempted to eliminate composite domain structure with homogeneous atomic arrangement in O2 type-LMR cathode. Figure A.2.25-2.26 show that a O2-type $Li_xNi_{0.13}Mn_{0.54}Co_{0.13}O_2$ cathode material is characterized by eliminating composite domain structure with homogeneous atomic arrangement. As a result, the differential electrochemical activities are effectively suppressed, which is evidenced by a smooth charging behavior with no apparently differentiated voltage plateaus (Figure A.2.27). Benefitting from the well-integrated electrochemical activities, the O2 based cathode fundamentally eliminates the prerequisite for strain generation, thereby inhibiting oxygen release and achieving an enhanced electrochemical performance with stable voltage profiles. This result in turn proves that the elimination of lattice strain is essential to solve the long-standing voltage fade issue. Other realistic strategies based on electrochemical reactivities could also be promising. It will be more ideal if two types of redox

reactions can be completely blended, achieving a whole-voltage-range cationic/anionic hybrid redox cathode material. This could not only eliminate the electrochemically inhomogeneous reactivity of two domains, but also access to higher energy density, which potentially carries forward the practical application of anionic redox or cationic/anionic hybrid cathode materials.

2.3 Conclusion

With an innovative combination of in-situ BCDI and 3D rED techniques, we thoroughly investigated spatial and temporal strain evolution of the LMR cathode during in-operando conditions. A convincing mechanism that lattice displacement and strain accumulation trigger oxygen loss and detrimental structure degradations is naturally established by leveraging gas investigation and DFT calculation. The multiscale structure characterizations from CMCD and macroscopic XRD further indicate that the inhomogeneous structure evolution in the coherent lattice dominates the formation of lattice displacement and nano-strain accumulation. To fundamentally resolve this issue, we propose that eliminating the electrochemically inhomogeneous reactivity of two domains is crucial for suppressing lattice strain and subsequent electrochemical degradation. Structure design based on O2 phase and whole-voltage-range oxygen redox cathode are considered as realistic strategies for resolving voltage fade. These findings highlight the importance of the lattice strain in the voltage decay mechanism and will serve as the guideline for seeking new solutions to eliminate this issue.

2.4 Materials and Methods

2.4.1 Materials Synthesis

The primary particle cathode materials of $Li_{1.2}Ni_{0.13}Mn_{0.54}Co_{0.13}O_2$ was synthesized using a sol-gel method. In a typical synthesis, $LiCH_3COO{\cdot}2H_2O$ (Aladdin, 99%), $Ni(CH_3COO)_2{\cdot}4H_2O$ (Aladdin, 99%), $Co(CH_3COO)_2{\cdot}4H_2O$ (Aladdin, 99.5%), $Mn(CH_3COO)_2{\cdot}4H_2O$ (Aladdin, 99%) and Polyvinylpyrrolidone (Aladdin, K30) were mixed in a molar ratio of 9:1:1:4:30 and then dissolved in 100 mL of deionized water. The resulting solution was dried at 90 °C overnight under continuous stirring and then calcinated at 500 °C for 3 hours. The obtained powder was thoroughly ground and mixed in a mortar and then calcinated at 900 °C for 12 hours to obtain the final product.

2.4.2 Electrochemistry Tests

For electrode preparation, active materials were mixed with carbon black (C45 Conductive Carbon Black, TIMCAL) and polyvinylidene fluoride (PVDF, 8%wt Solvay® 5130 PVDF binder dissolved in n-methyl-2-pyrrolidone (NMP)) at 80:10:10 wt. % ratios and then followed by grinding the mixture in a mortar at 2000 rpm for 9 min (3 min per time, a total of 3 times) in air atmosphere. The slurry was coated onto 10 μm-thick Al foil and then punched into round pieces with a diameter of 14 mm. The electrodes were dried at 80 °C under vacuum for 12 h to remove all traces of solvent. The 2032 type coin cells were used to prepare lithium metal cells. Celgard 2325 separators (25 μm), 1.2 M $LiPF_6$ in EC / EMC (3:7) electrolyte (GEN II with a water content below 20 ppm, 40 μl) and Li metal foil (MTI, 16mm x 0.6mm (diameter x thickness), high purity of 99.9%) were used. The half cells were then cycled between 2.0 and 4.8 V vs Li^+/Li, using small amounts of powder (~5.2 mg/cm^2) as positive electrodes.

2.4.3 Materials Characterization

Bragg coherent X-ray diffraction imaging and coherent multiple crystal diffraction: Bragg coherent diffraction data were collected at the 34-ID-C beamline of the Advanced Photon Source (APS). For the coherent diffraction analysis shown in this manuscript, we used 11.2 and 9 keV monochromatic beams in two independent experiments. The coherent X-ray beam was focused using a pair of Kirkpatrick−Baez (KB) mirrors to ∼1 × 1 μm^2 illuminating the LMR nanocrystals. The measurement was done on a 10 μm thick LMR electrode in transmission geometry. We used the same in situ coin-cell setup, which was implemented in the previous experiments with a window opening of 1 mm.[107] The coin cell was mounted on a coin cell holder vertically with the LMR electrode located downstream to minimize the absorption of the diffracted X-rays. The particle morphology of the LMR particles was examined with SEM, indicating 200−600 nm sized LMR particles (Figure A.2.1-2.3). From the fringe spacing in the diffraction patterns, we estimated that the measured LMR nanoparticle size is approximately 600 nm.

Coherent X-ray multi-crystal diffraction (CMCD) patterns were acquired using a Timepix photon-counting detector mounted D = 1950 mm away from the sample. We obtained full rocking curves around the (003) Bragg reflection and collected 2D CMCD patterns using a 2D detector at two-theta angles of 18.6° ($\Delta\theta = \pm 0.15°$), respectively. Although the full sensor of the detector has 512 × 512 pixels with 55 × 55 m pixel size, the coherent diffraction patterns were collected utilizing just the first quadrant sensor, which has fewer bad pixels. Automatic background subtraction is implemented within the detector.[107] We collected 22 sets of CMCD patterns and each set includes 302 CMCD patterns by rocking the sample in 0.0025° steps around the Bragg peak while we were cycling the coin cell at the C/10 current rate (the C/10 rate is the current value discharge a battery in 20 h). Between consecutive scans, we optimized the sample position on a piezo scanning stage,

to maintain the Bragg condition and avoid sample misalignment. The coin cell was cycled using an 8-channel MACCOR battery cycler while the series of measurements progressed.

Synchrotron X-ray diffraction, X-ray absorption spectroscopy measurement: Powder diffraction data of the cathode materials was collected using high-energy X-ray diffraction (HEXRD) located at sector 11-ID-C of the Advanced Photon Source at Argonne National Laboratory. A high-energy X-ray with a beam size of 0.2 mm×0.2 mm and wavelength of 0.1173 Å was used to obtain two-dimensional (2D) diffraction patterns in the transmission geometry. X-ray patterns were recorded with a Perkin-Elmer large-area detector placed at 1800 mm from the samples. Rietveld refinement of the collected HEXRD patterns was carried out using GSAS package. *Ex-situ* HEXRD measurements were performed at the same beamline. The electrodes were dissembled from the coin-cells charged or discharged to different potentials. With high penetration and low absorption, synchrotron HEXRD precisely reflects bulk sample structure properties, which is beneficial when observing tiny phase changes that usually are invisible from lab scale XRD due to poor background noise. To avoid peak interference from Al current collector, a freestanding LMR electrode was prepared from a mixture of LMR powder, carbon black and PTFE at 80:10:10 wt. % ratios.

X-ray absorption near edge structure (XANES) and extended X-ray absorption fine structure (EXAFS) for Mn K-edge were performed at the APS on the bending-magnet beamline 9-BM-B. X-ray photon energy was monochromatized by an Si (111) double-crystal monochromator. Higher-order harmonic contaminations were eliminated by detuning the monochromator to reduce the incident X-ray intensity by approximately 30%. All spectra were collected at room temperature in the transmission mode.

Density Functional Theory (DFT) calculation: All calculations were performed based on density functional theory (DFT) using the plane-wave projector-augmented wave method as implemented in the Vienna ab initio simulation package (VASP). The Perdew−Burke−Ernzerhof (PBE) exchange-correlation functional was used and the Hubbard U corrections (PBE+U) was taken into account, with the effective U of Mn (4.2 eV) adopted from previous studies. A kinetic energy cutoff of 520 eV and a k-point mesh of 11 × 11 × 11 were employed. Spin-polarization was considered for all calculations. Structures were relaxed until a force tolerance of 0.01 eV/Å was reached. The formation energy of oxygen vacancy was obtained using the following formula:

$$E^{f}[V_O] = E_{total}[V_O] - E_{total}[P] + \mu_O \quad (2.1)$$

where $E_{total}[V_O]$ and $E_{total}[P]$ are the total energies of the supercells with and without an oxygen vacancy, respectively. μ_O is the chemical potential of oxygen, for which we used the gas-phase O2 molecule as the reference. An energy correction of 0.68 eV/atom was applied to compensate the overbinding of O2 in DFT calculations.

Gas evolution analysis: Differential electrochemical mass spectrometry (DEMS) was applied to detect and identify gas evolution of different cathode materials during first charge/discharge. The differential electrochemical mass spectrometry (DEMS) was built based on a purchased mass spectrometer (HPR-40, Hiden Analytical). A homemade cell with glass fiber separators and 1.2 M $LiPF_6$ in EC / EMC (3:7) electrolyte (GEN II) was used for *in-situ* measurements. To increase the gas detection accuracy, we adopt the method of intermittent gas intake and use a certain degree of vacuum to ensure that the generated gas is completely ingested. The generated gas was collected in the cell for 60 minutes before being ingested into the mass spectrometer. In addition, to prevent O2 from reacting with Li metal, we assembled full cells using graphite as the anode electrode in

our DEMS experiments. The cells were then cycled at a current rate of C/10 between 2.0 and 4.8 V vs Li^+/Li, using small amounts of powders (~8 mg) as positive electrodes.

Transmission electron microscopy measurement: TEM and HRTEM were conducted using the Argonne Chromatic Aberration-corrected TEM (ACAT) (a FEI Titan 80-300 ST with an image aberration corrector to compensate for both spherical and chromatic aberrations) at an accelerating voltage of 200 kV. The 3D-rotation electron diffraction (3D-rED) datasets were acquired by stepwise tilting sample with a collection angle of -40° to 40°. The tilt step is 2°. The reciprocal lattice pattern was then reconstructed and analyzed by a handwritten script.

Chapter 3

Parasitic Structure Defect Blights Cobalt-Free Single Crystal Cathodes

Abstract

In the pursuit of reducing battery costs and improving sustainability, substantial efforts have been dedicated to eliminate cobalt (Co) use in cathode materials. Recent Co-free designs have demonstrated notable success in polycrystalline cathodes, exhibiting competitive electrochemical performance and structural stability. Logically, single-crystallization potentially further advances Co-free cathodes, as they enhance mechanical/structural properties and minimize side reactions compared to polycrystalline cathodes. However, given the significant alterations in structural properties, the efficacy of Co removal in single-crystalline (SC) cathodes becomes less understood. Here, we unveiled that removing Co from SC cathodes is structurally and electrochemically unfavorable, leading to an unusual voltage fade issue that was rarely observed in Ni-rich cathode materials. Combining multiscale diffraction and imaging techniques, it is found that an atomic structure defect, lithium-rich nanodomains (LRNDs) as a heterogeneous phase, universally exists in lattice structure of Co-free SC cathodes. The heterogeneous LRNDs acting as tipping point, induce significant chemo-mechanical lattice strain and irreversible structural degradation, resulting in fast voltage and capacity degradation. These findings highlight the considerable challenges associated with realizing Co-free single-crystalline cathodes compared to the polycrystalline system, emphasizing the need for new strategies to balance the interplay between cost, sustainability, and performance.

3.1 Introduction

The rapid adoption of electric vehicles (EVs) offers a promising way to reduce carbon emissions into the environment and contribute to the long-term goal of carbon neutrality.[6,118-119] Nevertheless, the excessive utilization of cobalt (Co) in battery raw materials raises concerns about the sustainability of EVs over time, owing to the scarcity of Co, its elevated costs, and volatile supply chains.[79,120] In response, developing Co-free cathode materials has gained momentum, aiming to reduce Co dependency, ensure robust capacity, and enhance battery sustainability.[121] Nowadays, polycrystalline Co-free cathodes have demonstrated competitive electrochemical performance compared to conventional Co-contained cathode materials, which raises the question of whether Co use is even necessary.[12,49] However, regardless of whether Co is used, there have been inherent limitations that persist within the long-standing design of polycrystalline spherical particle morphology.[85,90,122] These micron-sized secondary particles, comprising multiple primary nanoparticles, permit electrolyte penetration into the bulk through interstitial gaps among crystal grains to initiate severe interfacial side reactions.[123,124] Moreover, the random crystallographic orientation of primary particles will exacerbate mechanical degradation due to anisotropic volume evolution during electrochemical cycles.[125]

Single crystal (SC) $LiNi_xMn_yCo_zO_2$ (NMC) holds the potential to extend the lifespan of lithium-ion batteries (LIBs) by mitigating challenges such as mechanical degradation and surface side reactions found in polycrystalline NMC.[59] Similarly, there is motivation to reduce Co content in SC and realize Co-free SC cathodes to reduce cost challenges, as well as resolve sustainability issues related to material sourcing.[48] While the success of Co-free cathode in polycrystalline is indeed inspiring, the thorough understanding for the impact of Co-free designs on SC has yet to be detailed.[126-129] Fundamentally, the removal of Co and its impact on dynamic

structure evaluation in both the synthesis and electrochemical operation is unclear. Co plays a pivotal role in facilitating Li^+ diffusion within the lattice, a particularly critical attribute for SC cathodes, given their elongated diffusion pathways whereby heterogeneous Li diffusion can occur and lead to strain evolution.[43,131] In addition, the fabrication of single crystal morphology using high-temperature conditions intrinsically introduces substantial structure defects.[59] Addressing such defects has historically relied on Co, which, by virtue of its tendency to oxidize preferentially and unique electronic configuration, promotes structural ordering and suppresses the formation of Ni/Li mixing.[131,132] Therefore, notwithstanding the inherent cost benefits, the merits of Co-free designs in SC remain a mystery, necessitating a more profound and comprehensive understanding.

In this work, we systematically investigate Co-free high-Ni single-crystal cathode materials to understand the impact that removing Co will have. It was found that removing Co is electrochemically and structurally unfavorable for single crystal cathodes and significantly affects electrochemical properties and structure integrity. Leveraging multiscale structural characterizations, we revealed that the removal of Co and the high-temperature calcination to form single crystal morphology would introduce an unexpected atomic lithium-rich domain that is randomly distributed in the bulk lattice, which was never observed in both Co-contained NMC cathodes and polycrystalline Co-free cathodes.[133-135] In addition, given the extended diffusion pathways of SC, Li diffusion gradients are exacerbated by the presence of lithium-rich domain, which can lead to significant chemo-mechanical lattice strain that was directly confirmed by X-ray nanodiffraction. As a result, the Co-free SC cathode displays unsatisfactory initial capacity, coulometric efficiency, and unusual voltage degradation. This work underscores that the realization of Co-free single-crystal cathodes is a formidable challenge that requires substantial

advancements before it can materialize, particularly in the absence of a suitable alternative element.

3.2 Results and Discussion

3.2.1 Structure and Electrochemical Performance

A series of Co-free Ni-rich cathodes were synthesized using a two-step method involving co-precipitation synthesis of the precursors and solid-state calcination. The detailed preparation procedure can be found in the experimental methods section. Here, $LiNi_{0.75}Mn_{0.25}O_2$ (SC75) was selected as a model sample for the systematic investigations because this optimal composition is supposed to be more stable than ultrahigh Ni content (>80%) cathode and provide higher energy density than median Ni-content (50%~60%) cathode while being more cost efficient. The initial morphology of the SC75 sample after synthesis was first investigated by scanning electron microscope (SEM). As shown in Figure 3.1a, the SC75 particles present a fairly uniform particle size in the range of 3-5 μm. The particle size is apparently larger than that of the primary particle of conventional polycrystalline cathode materials, which may cause sluggish Li insertion and the formation of initial structure defects during the sample synthesis.[136,137] The phase structure of SC75 was then investigated by synchrotron based high-energy X-ray diffraction (HEXRD) and Rietveld refinement analysis. As illustrated in Figure 3.1b, all Bragg diffraction peaks can be well indexed to a hexagonal α-$NaFeO_2$-type layered structure (*R-3m* space group) without any impurity detected. It should be noted, however, that the (003) peak intensity and the ratio of (003)/(104) peak are relatively low, which together suggests the SC75 has a relatively high content of Li/Ni disorder or structure defects. This is further confirmed by Rietveld refinement analysis as shown in Table B.3.1, where the Li/Ni disorder is quantified as 5.44% and higher than most Co-contained single crystal cathode materials.[15] When used, Co's nonmagnetic

properties and large steric differences with Li allow for the energetically favorable formation of well-layered structures, so it is expected that removing Co would result in more Li/Ni disordering.[138]

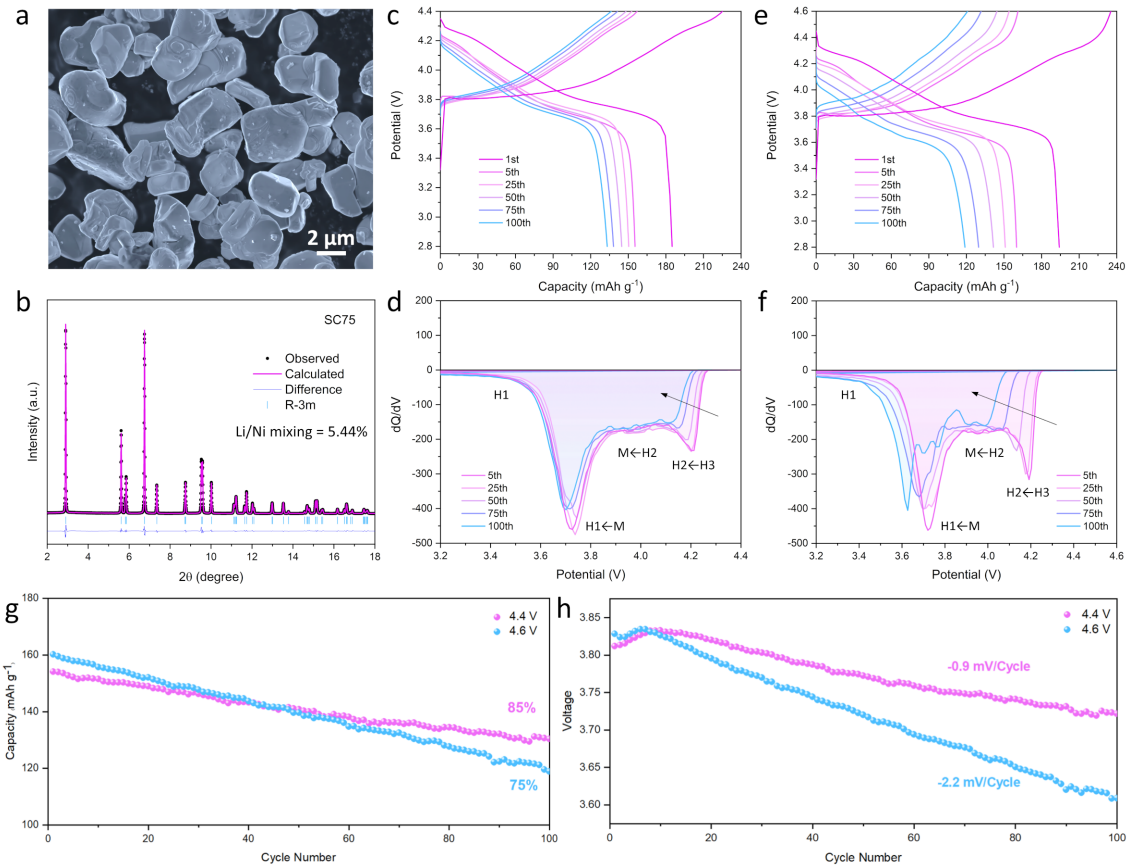

Figure 3.1. Structure and electrochemical performance of SC75 cathodes. (a) SEM image of the prepared SC75 particles. (b) High-energy XRD and Rietveld refinement plot of the SC75 sample. (c) Charge and discharge curves of SC75 electrode within a cutoff voltage range of 2.8-4.4 V. (d) Associated *dQ/dV* profiles for 4.4 V cycling. (e) Charge and discharge curves of SC75 electrode within a cutoff voltage range of 2.8-4.6 V. (f) Associated *dQ/dV* profiles for 4.6 V cycling. (g) Cyclic stability curves of SC75 electrodes at the current rate of 0.5C within the voltage ranges of 2.8-4.4 V and 2.8-4.6 V after three activation cycles. (h) Detailed voltage fade analysis during the long-term cycling.

The electrochemical performance of SC75 was evaluated by coin-type cells with as-prepared SC75 and Li metal anode at different voltages. The galvanostatic charge/discharge curves in Figure 3.1c show that the initial capacity was recorded as 185 mAh g^{-1} at 0.1C within a voltage window of 2.8-4.4V. It is of note that the coulombic efficiency of the initial cycle was

only 84%, which is lower than those of typical Co-contained SC cathodes.[64,139,140] The subsequent cycles operated at 0.5C show a slight capacity degradation during cycling. The corresponding *dQ/dV* curves are used to describe the structural reversibility during electrochemical cycling. As shown in Figure 3.1d and Figure B.3.1, the presented *dQ/dV* peaks reflect the phase transitions of the layered structure at different stages with a sequence of H1-M-H2-H3 transitions in charging and inverse transitions in discharging. During cycling, the peaks at 4.2 V clearly shift to lower voltage with degraded peak intensity, while the peak at 3.75 V is relatively stable. This suggests that capacity fade and structure degradation mainly occur during the H2-H3 phase transition.

Figure 3.1e further shows the electrochemical performance of the SC75 electrode when the charging voltages are raised and cycling occurs between 2.8-4.6 V. The initial capacity is recorded as 194 mAh g^{-1}, a bit higher than that of 4.4 V. However, the coulombic efficiency and rate performance are even worse compared to that at 4.4 V, suggesting an additional reaction occurred at high voltage. This is further confirmed by the charge/discharge profiles and the corresponding *dQ/dV* curves (Figure 3.1f and Figure B.3.1). Besides the fast capacity fading, an obvious voltage decay can be observed during the prolonged cycles, which is usually absent from layered NMC cathode materials. Furthermore, the *dQ/dV* curves shown in Figure 3.1f have significant peak shifts during charge and discharge as long-term cycling proceeds. For example, the peaks at both 4.2V and 3.7 V have quickly shifted to lower potential with a weakened intensity. In addition, new peaks at 3.90 V, 3.77 V, and 3.71 V are present upon discharge after 100 cycles, indicating an irreversible phase transition occurred when cycled at 4.6 V. In general, the Co-free SC75 electrode exhibits underachieved cycle stability and fast structure degradation at high operation voltage.

The capacity and voltage retentions are summarized in Figure 3.1g and h, respectively. The capacity retention after 100 cycles at 4.4 V is 85%, whereas it is only 75% at 4.6 V. The exacerbated capacity fade at 4.6 V should be attributed to the irreversible structural transformations observed in the *dQ/dV* peak profiles. Moreover, as displayed in Figure 3.1h, the SC75 electrode cycling at 4.6 V shows an accelerated voltage fade, where the voltage fade is recorded as -0.9 mV per cycle at 4.4 V but increases to -2.2 mV per cycle at 4.6 V. Note that the significant voltage fade is not a characteristic feature of the conventional layered NMC cathodes. Considering unexpected low coulombic efficiencies, poor structural reversibility, and voltage fade, it is highly suspected that the removal of Co may have led to subtle structural changes in SC75 that impact electrochemical performance and structure integrity.

3.2.2 Structure and Chemical Stability in Bulk Level

To uncover these abnormal phenomena, in-situ XRD was conducted to monitor the structure reversibility during the electrochemical process. Figure 3.2a and b depict the two-dimensional (2D) contour plots for the structural evolutions of the SC75 electrodes during the first charge-discharge cycle at the different voltage ranges of 2.8-4.4 V and 2.8-4.6 V, respectively. In general, the in-situ XRD results operated at different voltages show similar phase transition behavior without additional phase transition detected at high operating voltage. Specifically, the (003) reflections initially shift to lower 2θ values, which indicate increases in *c-axis* lattice spacing and correspond to H1-M and M-H2 transitions. After that, the (003) reflections undergo a sudden right shift, implying rapid decreases in *c-axis* lattice spacing, which is associated with the H2-H3 phase transitions at high voltages.[141] During the discharging process, all the peaks smoothly shift back to the original position following a reverse sequence. Both in-situ XRD results show that the structure evolution of SC75 seems reversible without obvious structure

degradation within one cycle. The difference is that the SC75 cathode cycling at 4.6 V exhibits a slightly larger change in the *c-axis* lattice parameter than at 4.4 V, which is attributed to more Li removal with increased cut-off voltage.

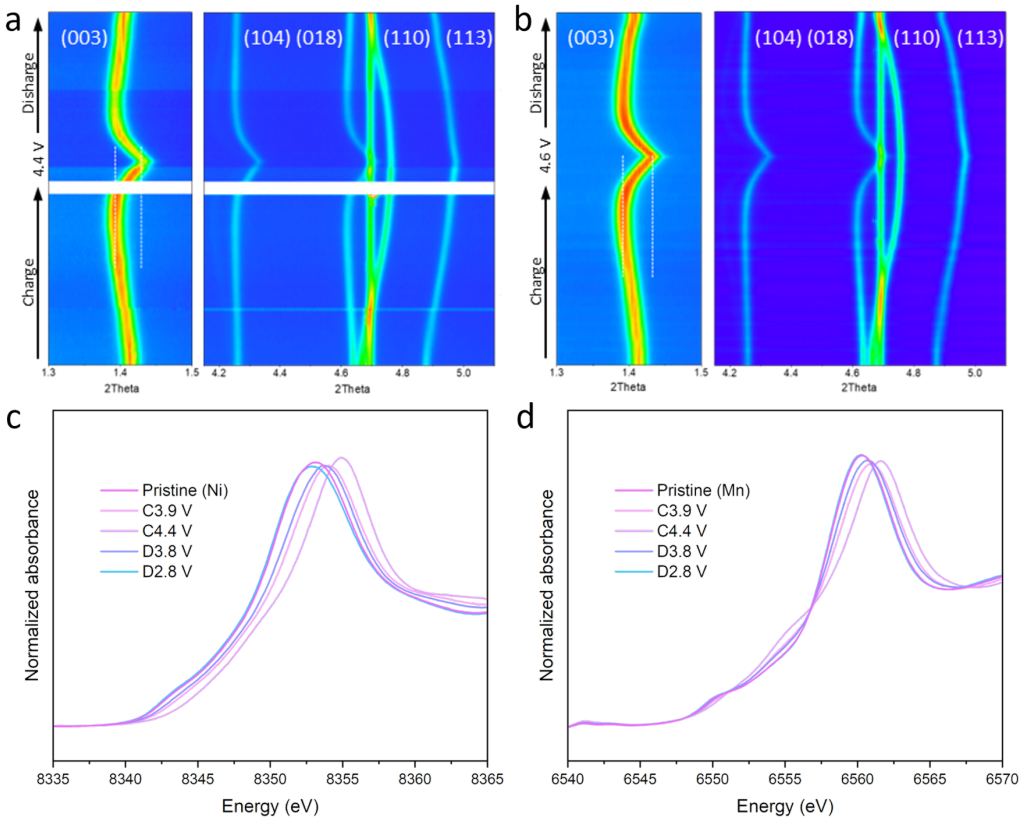

Figure 3.2. Statistical structure and valence evolution of SC75 during charge-discharge process. (a, b) Two-dimensional contour plots of in situ HEXRD for the structural evolution of SC75 at the initial cycle within the voltage ranges of 2.8-4.4 V (a) and 2.8-4.6 V (b). (c, d) Ex situ Ni (c) and Mn (d) K-edge XANES spectra of SC75 at different charge/discharge states.

X-ray absorption spectroscopy (XAS) was further conducted to investigate the chemical state changes for Ni and Mn in SC75 during the electrochemical process. Figure 3.2c and d depict the X-ray absorption near edge spectroscopy (XANES) of Ni and Mn K-edges at different charged and discharged states. It is clear that the peak position of the Ni K-edge shows a positive shift toward high absorption energy upon charging, reflecting an increase in the oxidation state (Figure 3.2c). Accordingly, an opposite change occurred in the discharge process. When

discharged to 2.8 V, the profile of the Ni K-edge basically returns to the initial state, indicating the chemical reversibility in an electrochemical cycle. However, the XANES of the Mn K-edge does not show apparent shifts in the electrochemical process, which illustrates that the Mn valence state remains stable and electrochemical inactive (Figure 3.2d). The shape deformation of the curve at 4.4 V can be related to the change in local coordination environment. Overall, with these macroscale characterizations, it is found that the structural and chemical evolution of SC75 is reversible and not much different from conventional layered NMC materials. However, the apparent structural instability and unusual electrochemical phenomena at high voltage remain unexplained, which suggests that macroscopic characterizations may not be sufficient to identify the structural changes associated with the removal of Co. Therefore, microscopic structural characterizations at the nano or atomic scales are essential to understanding the SC75 sample.

3.2.3 3D Rotation Electron Diffraction and Atomic Imaging Observation

To thoroughly investigate the microstructure of SC75, 3D continuous rotation electron diffraction (3D-CRED) was utilized to analyze the lattice structure and distortion. Unlike conventional selected area electron diffraction (SAED) and polycrystalline XRD, where only the diffraction information of two-dimensional cross-sections can be obtained, 3D-CRED collects a tilt series of diffraction patterns by continuously single-tilting the sample to reconstruct the 3D reciprocal lattice, as shown in Figure 3.3a. Hence, the structural information can be resolved in arbitrary directions instead of a specific direction.[142] Furthermore, compared to the statistical XRD technique, 3D-CRED technique allows the data to be acquired on much smaller sample volumes and collected within minutes. Therefore, this method is especially suitable for the structure analysis of single-crystal cathode materials.

The transmission electron microscope (TEM) image in Figure B.3.2a shows the selected SC75 single particle used for the 3D-CRED measurement. At this moment, the sample is at the eccentric height under the irradiation of a parallel electron beam. Figure 3.3b and c and Figure B.3.2b are the corresponding results of the 3D-CRED measurement after data processing. Figure B.3.2b exhibits the reconstructed 3D-reciprocal lattice projection along the c^* direction. The regular arrangement of diffraction spots implies an ordered intralayer structure. However, the blue diffraction spots should not exist in a typical layered $LiTMO_2$ structure, indicating the presence of a superlattice.[143] Figure 3.3b and c are the reconstructed 3D-reciprocal lattice projections along the a and a^* directions, which further reveal the interlayer structure information. It is clear that multiple diffraction streaks along the c^* direction are observed. This kind of diffraction feature reflects the stacking faults in the layered structure.[144] Therefore, the 3D-CRED technique enables the observation of new structure defects in SC75 at the single particle level that is invisible in polycrystalline NMC cathode and is also undetectable with the bulk characterization techniques. This indicates that the microstructure of SC75 may be more complex than conventional NMC materials and provides some clues for the unusual electrochemical phenomena.

Detailed TEM characterization of the SC75 particle was carried out at different zone axes to investigate the exact microstructure at the nanoscale. Figure B.3.3 shows the low-magnification TEM images at the zone axis of [110], [210], and [16 8 -1] taken at same location. The [110] zone axis is a basic orientation of the layered $LiTMO_2$ structure.[6] The corresponding SAED pattern, shown in Figure 3.3d, manifests a standard diffraction feature of layered $LiTMO_2$ structure without impurity phase. Moreover, the HRTEM image in Figure 3.3g further manifests the atomic arrangement of the layered structure, where the TM layers can be clearly seen with no

obvious intensity difference along this orientation. The slightly enhanced contrast in Li layer implies a small amount of Li/Ni mixing, consistent with XRD result. The TEM observation at this zone axis does not show the stacking faults and superlattices that are observed in 3D-CRED. This also reflects that these structural defects are easily overlooked in conventional characterization.

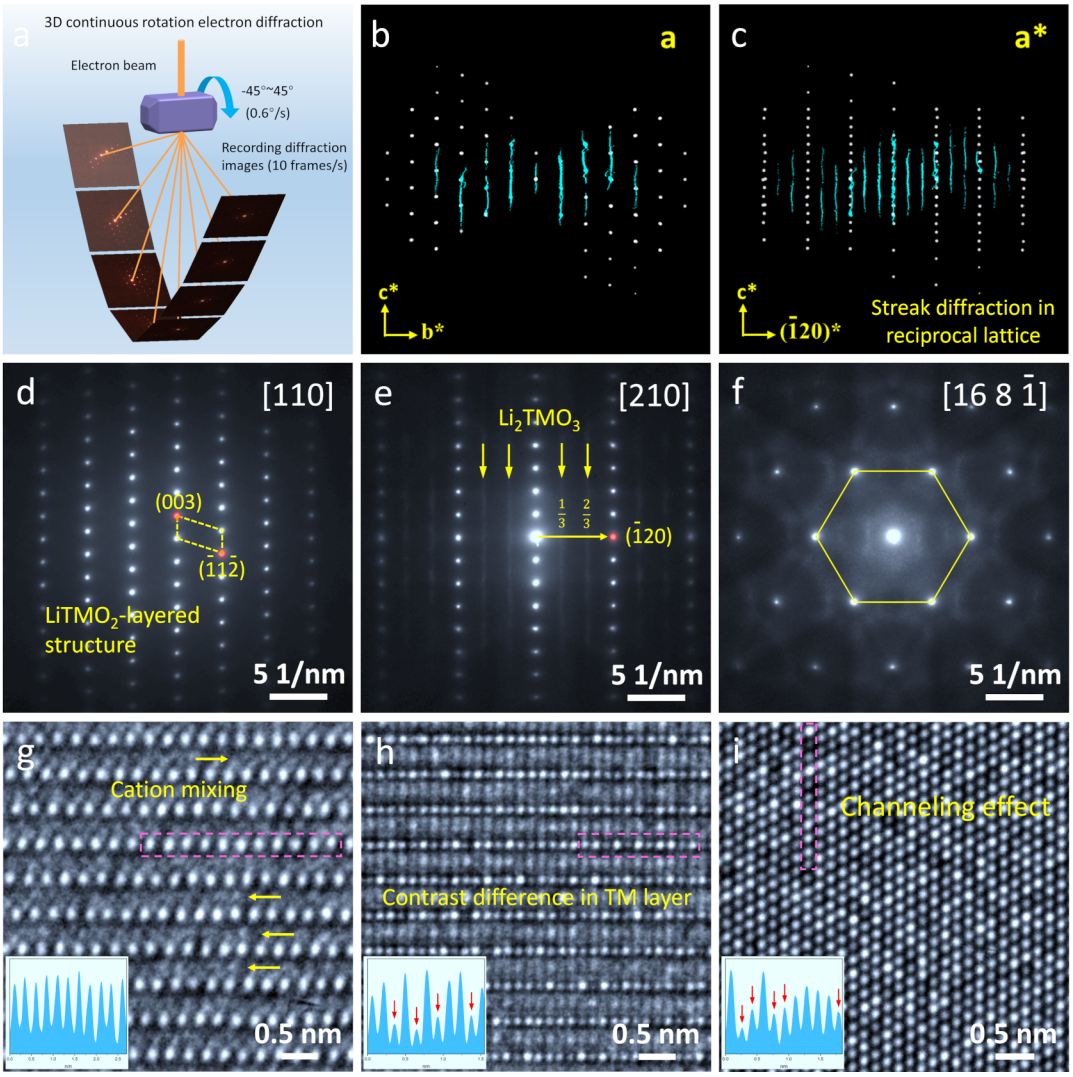

Figure 3.3. 3D-CRED, 2D-SAED, and HRTEM characterization. (a) Schematic diagram of 3D-CRED. (b, c) The reconstructed 3D-reciprocal lattice projections along different directions. (d-f) 2D-SAED patterns and (g-i) corresponding HRTEM images along different orientations, the insets in HRTEM images are the corresponding line intensity profiles of red boxes.

When tilting to [210] zone axis, the TM atoms are arranged vertically along the *c-axis* between the layers and have smaller in-plane spacing. Hence, higher-resolution imaging is required to analyze structure details. As shown in Figure 3.3e, the corresponding SAED pattern at the [210] zone axis shows that an additional diffraction steaks present parallel to (001) at n/3 (1-20) positions, which is a typical diffraction feature of the Li_2TMO_3 (Li-rich phase), corresponding to the ordering of excess Li in the TM planes.[54] The HRTEM image in Figure 3.3h further demonstrates the SAED result, and the obvious contrast differences are observed in the TM planes owing to the occupation of Li. These results indicate the layered structure of SC75 is mixed with the small amount of Li_2TMO_3 phase, which is rarely observed from typical NMC cathode materials. The same structural features are also present in SC80 and SC90 samples, suggesting that this is a common structure defect of Co-free SC cathodes (Figure B.3.4-3.6).

The above TEM characterization at the interlayer [210] zone axis reveals the presence of Li/TM ordering in the TM plane. Hence, the intralayer observation at the [001] zone axis is desirable to reflect the distribution of the impurity phase. However, the angle between these two directions is 90°, which cannot be achieved in the same particle as the TEM observation. As shown in Figure 3.3f, the same TEM observation was chosen to be performed at [16 8 -1] zone axis, which is reached by tilting the sample at [210] zone axis around the (1-20) by 20°. This zone axis is equivalent to the [001] zone axis in the layered structure because they both belong to the family of <111> crystal directions in the parent structure of the face-centered cubic lattice. The SAED pattern in Figure 3.3f displays the typical six-fold diffraction spots but with a weak superlattice.[55] In Figure 3.3i, the HRTEM image and selected intensity line profile exhibit the apparent channeling contrast difference, indicating that the Li_2TMO_3 phase is randomly distributed and remains extremely small in nanometer size. Hence, the heterogeneous Li_2TMO_3

phase can be seen as numerous Li-rich nanodomains (LRNDs) embedded in the layered structure. This result agrees with the prior bulk XRD observations where no superlattice peaks were detected. The unexpected LRNDs in SC75 provide some clues for the voltage fade and fast capacity decay at high voltage, as voltage fade is a well-known phenomenon in Li-rich cathode materials.

3.2.4 LRNDS Cause Lattice Strain and Lattice Bending

It has been well acknowledged that $LiTMO_2$ and Li_2TMO_3 phases are activated at different voltages, and severe lattice strain is generated owing to the heterogeneous electrochemical processes, which is highly corrected with electrochemical failure.[121] Here, the presence of Li_2TMO_3 domains in SC75 may also impact the lattice strain evolution, leading to structure and performance decay. Hence, scanning X-ray diffraction microscopy (SXDM) was performed to analyze the lattice strain evolution of SC75 particles in the initial cycle and prolonged cycle. To increase the strain sensitivity, dark field images are created by integrating in the reciprocal space all the pixels that fall in a certain q-range based on the obtained five-dimensional diffraction dataset (see Methods). Figure 3.4a, d, and g show the structural mappings of SC75 particles at different states and cycles, where the color gradient reflects the lattice parameter variation and the arrow indicates the deformation of the lattice that manifests as lattice bending. Note that lattice bending here refers to rigid body rotations of the crystal lattice that are independent of the effect of strain. The direction of the arrows shows the direction of the bending, and the length of the arrows is indicative of the magnitude of the bending. Figure 3.4a shows that the pristine particle has a narrow d-spacing distribution with only 0.25% variation and negligible lattice bending (maximum amplitude of 5 mrad). In the dark field image for the unstrained part (i.e., strain ~ 0%, Figure 3.4b), the largely uniform intensity contrast indicates that the pristine particle

is a high-quality single crystal with no visible defects. A small portion of the surface is strained by only 0.2% (Figure 3.4c), which may be caused by the slightly off-stoichiometric Li content on the particle surface.

When the particle was charged for one cycle, the lattice parameter variation and lattice bending show significant changes. As shown in Figure 3.4d, both the lattice variation (lattice strain) and lattice bending at this stage are double as compared with the pristine particle. Larger bending was again found at areas with larger variations of d-spacing and the maximum magnitude of bending has more than doubled, to 13 mrad. The dark field image on the unstrained area (Figure 3.4e) shows an inhomogeneous particle. More importantly, a significant amount of surface area was shown (Figure 3.4f) to have a large compressive strain of 2%, which is ten times larger than that of the pristine particles. The surface compressive strain is highly related to the inhomogeneous delithiation caused by the faster reaction rate of the surface and sluggish Li^+ diffusion in the bulk. It is noted that the obvious d-spacing differences also exist within the bulk, which should be due to heterogeneous electrochemical processes between $LiTMO_2$ and Li_2TMO_3 domains. This strain induced by the heterogeneous electrochemical process will continuously accumulate during the repeated cycles.

The lattice strain and lattice bending analysis were also conducted for the cycled sample. As shown in Figure 3.4g, compared to the pristine state, the much larger average lattice parameter of the cycled SC75 suggests that a certain amount of Li could not reinsert into the lattice. This indicates that the SC75 undergoes severe structural irreversibility during long-term cycling, which is further corroborated by the d-spacing variation where the inhomogeneous d-spacing has been expanded into the particle bulk. In addition, large lattice bending was observed on most parts of the particle, with a maximum amplitude of 30 mrad, which is six times higher

than the pristine state. Moreover, the top part of the particle is tilted increasingly to the right, while the bottom part is tilted increasingly to the left, indicating a twisting of the entire particle around its long axis. An inhomogeneous particle is again observed in the unstrained dark field image (Figure 3.4h), with some parts compressively strained to 2% (Figure 3.4i). Based on the above understanding, a vivid model was built to reflect the structural change of the SC75 after cycling. As shown in Figure 3.4j, three types of mechanical change behavior (expansion, bending, and twisting) can be distinguished, and their combination leads to significant stress concentrations.

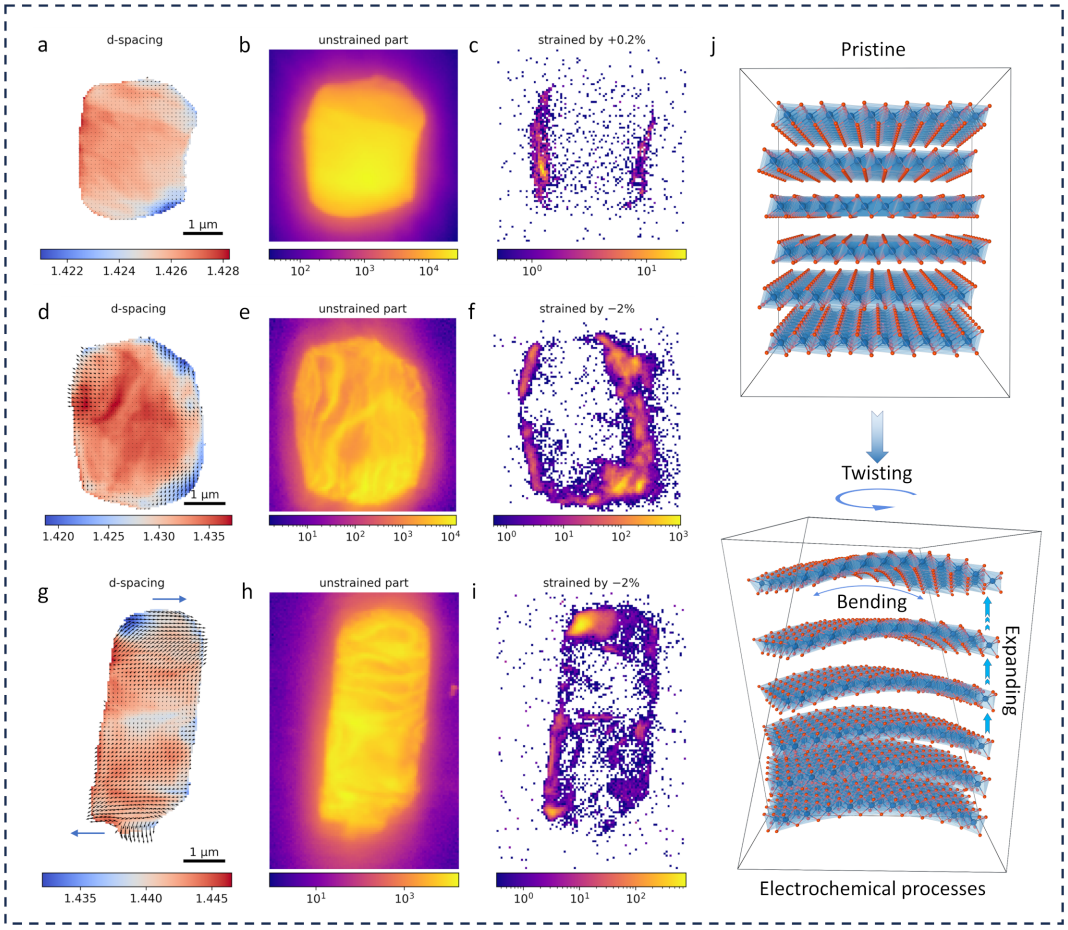

Figure 3.4. Scanning X-ray nanodiffraction microscopy characterization. (a, d, g) Structural mapping of SC75 particles at pristine (a), charged (d), and after100-cycles (g) stages based on 5D-diffraction dataset. (b, e, h,) The corresponding integration of unstrained parts. (c, f, i) The

Figure 3.4, continued. corresponding integration of strained parts. (j) the comparison of structural models for SC75 before and after cycling.

The above SXDM experiment reveals the heterogeneous lattice structure changes within the particles. Furthermore, full-field transmission X-ray microscopy (TXM) coupled with 3D X-ray absorption near-edge spectra (XANES) was performed to analyze the variation of chemical states at the particle level. The uniform color distribution on both 3D TXM-XANES mapping and cross-sectional 2D TXM-XANES mappings (Figure 3.5a-c) demonstrates a well-distributed Ni-related phase and the homogeneous oxidation state of the Ni element in the pristine SC75. The statistical analysis of the whiteline peak position shows a symmetric distribution and is centered at 8349.6 eV (Figure 3.5d). During charging, the observed color in the particles turns into red, indicating the increase of valence state of Ni with Li removal (Figure 3.5e-g). However, the uneven color distributions imply the heterogeneous electrochemical process, which can be attributed to the large particle size and presence of LRNDs. These phenomena are further reflected in the statistical whiteline peak position curve, which shows a positive shift and asymmetric distribution (Figure 3.5h). It is noted that the inhomogeneous distribution of chemical states persists in the long-term cycled sample (Figure 3.5i-k). Especially, the near-surface region displays the elevated valence of Ni (Figure 3.5k and l), which confirms that some of the Li is not reinserted into the lattice. This result is caused by the lattice distortion and phase transition, in agreement with the SXDM observation.

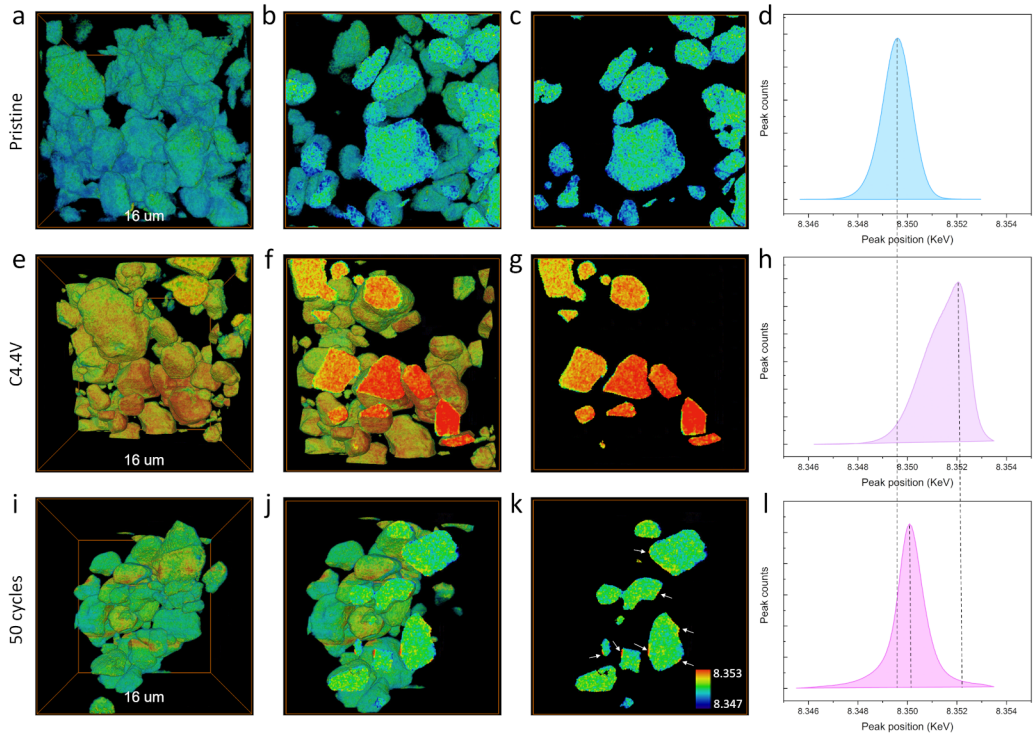

Figure 3.5. 3D TXM-XANES for chemical state distribution. (a-d) The 3D TXM-XANES mapping (a), cross-sectional views (b, c), and statistic distribution (d) based on whiteline peak position for pristine SC75. (e-h) The 3D TXM-XANES mapping (e), cross-sectional views (f, g), and statistic distribution (h) based on whiteline peak position for charged SC75. (i-l) The 3D TXM-XANES mapping (i), cross-sectional views (j, k), and statistic distribution (l) based on whiteline peak position for cycled SC75.

The morphology and structure changes after cycling were investigated by TEM. Figure 3.6a shows the low-magnification TEM image of the cycled SC75 particle at 4.4 V, and no obvious morphology damage is presented. Figure 3.6b is the corresponding SAED pattern. It is clear that the sample, after 100 electrochemical cycles, still maintains the basic layered structure. However, the Li_2TMO_3 phase is significantly reduced with the generation of a new spinal phase. Furthermore, the elongated diffraction spots, especially at high order, indicate the presence of microstrain inside the particles after cycling at 4.4 V. The microscopic structural changes after cycling were further revealed by the HRTEM test. The moire patterns are widely observed in the layered structure, indicating the localized lattice variations caused by strain concentration (Figure

3.6c and Figure B.3.7). In Figure 3.6d, the atomic-resolution HRTEM image further demonstrates the existence of spinel structure. In principle, Li_2TMO_3 phase is electrochemically inactive below 4.5 V. However, the generation of microstrain facilitates oxygen loss from the lattice, thereby triggering the TM migration and phase transition. Hence, these results clearly indicate that the LRNDs in SC75 induce structural degradation as well as the accumulation of microstrain during the electrochemical process at 4.4 V, further confirming the SXDM results.

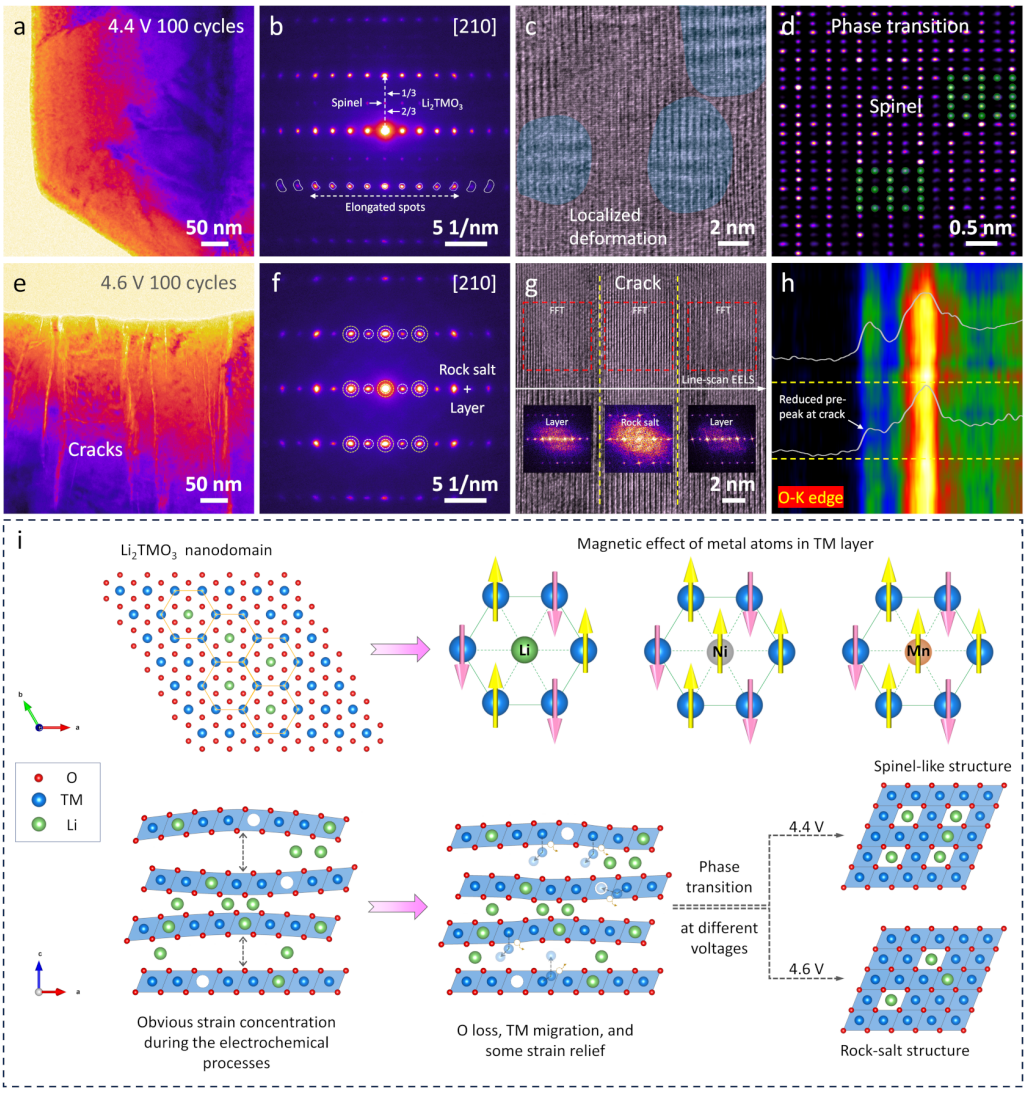

Figure 3.6. Microscopic TEM characterization for cycled SC75 and the formation and degradation mechanism of LRNDs. (a) Low-magnification TEM image of SC75 particle after 100 cycles at 0.5C and 2.8-4.4 V. (b) Corresponding SAED pattern showing the weak Li_2TMO_3 phase and newly formed spinel diffraction spots. (c) HRTEM image of the marked areas in (a) that shows structure transition after cycling. (d) Enlarged HRTEM image and corresponding FFT pattern showing the subsurface phase after cycling. (e) Enlarged HRTEM image and corresponding FFT pattern showing the surface phase after cycling. (f) Low-Magnification TEM image of SC75 particle after 100 cycles at 0.5C and 2.8-4.6 V where severe particle cracking and degradation is visible. (g) Corresponding SAED pattern where newly formed rock-salt structures are present. (h) HRTEM image showing the structural transition on the crack. (i) EELS line scan of O K-edge along the marked direction in (h). (j) The formation mechanism of LRNDs and phase transition route during electrochemical process.

Figure 3.6e further exhibits the low-magnification TEM image of the SC75 particle after cycling at 4.6 V. Unlike cycling at 4.4 V, severe intragranular cracks occur, leading to particle

damage (Figure B.3.8), which is the result of internal strain release and component loss due to side reactions. The SAED pattern in Figure 3.6f indicates the complete disappearance of the Li_2TMO_3 phase and the substantial increase of the rock salt phase after long-term cycles. As shown in Figure 3.5g, the HRTEM image further characterizes the microstructure near the crack. It is clear that the structure at the crack has transformed into a pure rock-salt phase, indicating the Li layer is completely occupied by the TM atom. The rock salt phase is electrochemically inactive, thus leading to a significant capacity decrease as observed in the electrochemical tests. Overall, the root cause of capacity fading is attributed to crack initiation by strain evolution, which expose fresh surfaces to trigger irreversible phase transitions of rock salt with electrolytes. According to our previous report, the strain concentration during the electrochemical process is closely related to the voltage fade and anion charge compensation mechanism of the Li_2TMO_3 phase. As shown in the line-scan EELS of Figure 3.6h, this is also well evidenced by the reduction of the pre-peak of O-K edge at the crack. Hence, the TEM results for the cycled SC75 sample indicate that the randomly distributed LRNDs are like structural faults buried in the $LiTMO_2$ phases, which are completely excited under high voltage to cause structure destruction.

3.2.5 Formation Mechanism of the LRNDs

The formation of the LRNDs, where Li is present in the TM layer, can be reasoned from the magnetic interactions that occur in the TM layers.[49] This mechanism was recently recognized as a new driving force in tuning the structural disordering of the conventional layered cathode materials. As shown in Figure 3.6j, for the SC75 sample in this work, Ni^{2+} and Mn^{4+} will induce strongly frustrated magnetic interactions between spins of TM ions in the TM layer, thereby give rise to lattice instability. In order to form a stable crystal structure, the extra nonmagnetic Li^+ is introduced in centers of the hexagons in the TM layer by forming a nonmagnetic center during

the synthesis of SC75. As a result, the LRNDs were finally formed in the layered structure of SC75 sample. Compared to the conventional layered cathode materials, the LRNDs in SC75 lead to the changes of electrochemical performance. The SC75 sample shows the low coulombic efficiency and substantial voltage decay during cycling, resulting from the heterogeneous electrochemical behaviors between $LiTMO_2$ and Li_2TMO_3 phases. Furthermore, the anion charge compensation mechanism of Li_2TMO_3 phase leads to the fast capacity fade especially at high operation voltage. The X-ray nanoprobe technique and atomic-scale TEM characterization revels that the LRNDs will induce the remarkable strain evolution and undesirable phase transition in bulk. The collective results confirm that the Co-free component design combined with single-crystal morphology does more harm than good to the electrochemical performance of layered cathode materials.

3.3 Conclusion

In conclusion, a nanodomain Li_2TMO_3 phase was discovered to exist and be heterogeneously distributed in the bulk structure of Co-free single-crystal layered cathode materials. The formation of the Li_2TMO_3 phase nanodomain alleviates the magnetic frustration within the TM layer and improves lattice stability, but leads to unsatisfactory electrochemical behavior and performance. Significant strain evolution and phase degradation in bulk occur during cycling, resulting from the heterogeneous electrochemical behaviors and anion charge compensation mechanism of Li_2TMO_3 phase. These forceful results confirm that removal of Co from single-crystal layered materials contains subtle structural changes that weaken the performance of the material in LIBs. Unlike in poly-crystalline cathode where Co-free designs have been found to improve LIBs performance, direct cobalt removal strategies in single-crystal cathode system are undesirable. New strategies must subsequently be designed in order to balance the cost,

sustainability, and performance of single-crystal cathode to realize their promising role in accelerating vehicle electrification.

3.4 Materials and Methods

3.4.1 Materials Synthesis

Co-precipitation methods were used to synthesize precursors for single crystal NMC. $Ni_{0.75}Mn_{0.25}(OH)_2$ precursors were produced by first adding nickel sulfate (Sigma-Aldrich, ≥98%) with manganese sulfate (Sigma-Aldrich, ≥99%) and then mixing to obtain a uniform metal ion solution. The solution was then pumped into a reactor at 2.0 mol L^{-1} while an additional 4.0 mol L^{-1} NaOH solution (aq.) and 5.0 mol L^{-1} NH_4OH solution (aq.) were pumped into the reactor. The NaOH solution acted as precipitating agent while the ammonia solution acted as a chelating agent. Reactor conditions were kept at ~11.5 pH, ~60°C, and 1000 rpm stirring rate. The resulting precursor powders were filter, washed, and vacuum dried overnight in a heated oven. SC75 was prepared by mixing $LiOH{\cdot}H_2O$ contents at a molar ratio of 1.03:1 (Li:[Ni+Mn+Co]) with the precursor and calcining overnight at 900 °C for 12 h under oxygen atmosphere.

3.4.2 Electrochemistry Tests

Active materials were mixed with carbon black (C45 Conductive Carbon Black, TIMCAL), polyvinylidene fluoride (PVDF, 8 wt% Solvay 5130), and n-methyl-2-pyrrolidone (NMP) at 80:10:10 wt% ratios to prepare solutions for electrodes. The mixture was then mixed at 2000 rpm for 9 min (3 min per cycle) in air atmosphere. After drying at 80 °C under vacuum for 12 h to remove traces of solvent, 2032 type coin cells were prepared using the electrode material. Lithium metal foil (99.9% purity, MTI. 16.0 mm x 0.6 mm, diameter x thickness), Celgard 2325 separators (25 μm), and 1.2 M LiPF6 in EC/EMC (3:7) electrolyte (GEN II with < 20 ppm water

content, 40 µl) were used to assemble cells. Cells were then cycled between 2.8 and 4.4 or 4.6 V vs Li+/Li in a temperature-controlled chamber at 25 °C ± 2 °C.

3.4.3 Materials Characterization

Synchrotron X-ray Diffraction: The 11-ID-C beamline at the Advanced Photon Source at Argonne National Laboratory was used to perform high-energy X-ray diffraction (HEXRD) experiments. A 0.2 mm x 0.2 mm X-ray beam with a wavelength of 0.1173 Å was used. To collect diffraction patterns in the Laue diffraction geometry, a Perkin-Elmer detector placed 1800 mm from the samples were used and Rietveld refinements were conducted using GSAS software packages.

In situ HEXRD was performed at the same beamline. This allowed visualization of small phase changes that are not noticeable in lab scale XRD. Experimental cells were assembled using 2032-coin cells with a 3 mm opening that allowed X-rays to pass and the opening was sealed using Kapton tape to prevent air atmosphere exposure. Diffraction patterns were collected every 10 min.

X-ray absorption spectroscopy: XANES for Ni K-edge and Mn K-edge were performed at the APS on the 9-BM-B beamline. A Si(111) double-crystal monochromator was used to monochromatize X-ray photon energy. In order to reduce X-ray intensity by about 30%, high-order harmonic contaminations were eliminated by detuning the monochromator. Spectra were collected in the transmission mode at room temperature.

3D-Continuous Rotation Electron Diffraction: TEM grids were carefully placed and fixed on a single tilt sample holder and inserted into the TEM sample stage. Sample nanocrystals were selected in the field of view and a series of 21 TEM images was recorded to track crystal

positions at 5° intervals across a range of -45° to + 45°. To account for crystal movement during the rotation of the goniometer, interpolation was used and diffraction patterns were recorded sequentially. Data acquirement begins with the recording of a diffraction pattern with beam precession. Then a charge coupled device recorded the next diffraction pattern without beam precession while the angle is slowly rotated by defined intervals. The step finishes by positioning the beam using a tracking procedure to the expected crystal position.

Scanning Electron Microscopy and transmission electron microscopy: After electrochemical cycling, coin cells were disassembled in a glove box with Ar atmosphere. Dimethyl carbonate was used to wash obtained cathode electrodes and samples were vacuum dried. TEM tests required thin specimens that were prepared from the electrode foil. Standard focused ion beam lift-out procedures were used to first thin specimens to 200 nm by a 30 kV Ga ion beam. Damaged layers were removed by polishing with a 5 kV Ga ion beam. The Argonne Chromatic Aberration-Corrected TEM (ACAT, FEI Titan 80-300 ST with an image aberration corrector was used to compensate for spherical and chromatic aberrations. TEM and HRTEM measurements were conducted at an accelerating voltage of 200 kV.

Synchrotron 3D X-ray Fluorescence and Nanodiffraction: The hard x-ray nanoprobe beamline at the Advanced Photon Source was used for scanning XRD and x-ray fluorescence experiments where 10 keV beam was focusing using a 160 μm Fresnel Zone Plate with an outmost zone width of 30 nm. Samples were placed under high vacuum to prevent oxidation and samples were placed 1 m from an Eiger 2 X 1M detector to collect diffraction images. To conduct strain analysis, a 4 x 4 μm^2 area was raster scanned with a focused beam at a spatial resolution of 50 nm. This was repeated at 16 different rocking curve angles at 3° intervals, a process known as k-

mapping or tilt series. With this method, 2-dimensional diffraction patterns are collected at each point on the area detector. This is equivalent to obtaining a 3-dimensional reciprocal space map about the (003) reflection for each point that is scanned in the nanoparticle. Dark field images result from the scans that are 3 dimensions in reciprocal space and 2 dimensions in real space, which are then reduced to 5 dimensional datasets. XRF signals were collected using a Vortex ME-7 detector during the raster scans. Resulting XRF maps were used primarily for aligning the 16 diffraction maps using image registration methods.

Full-field transmission X-ray microscopy (TXM) imaging: Transmission X-ray microscopy imaging was conducted at 18-ID FXI beamline of NSLS-II of Brookhaven National Laboratory and generate 3D nano-XANES datasets. At each energy, 3D tomography was reconstructed from the projection images taken from 0 to 180o. The voxel resolution of X-ray microscopy imaging was 40 nm.

Chapter 4

Multi Structure Design for High Voltage Nickel Rich Cathode

Abstract

Efforts to improve energy density of layered cathode materials by raising operational voltages is limited by intrinsic lattice instability at low lithiation levels. Other cathode types, such as lithium rich (LR) or disordered rock salt (DRX) have moderate to considerable Li and transition metal (TM) disordering, where TM in the Li layers can act as pillar to stabilize structures. However, despite their advantages these materials suffer from reduced energy density and rate capability when compared to layered cathode types which has limited their commercial applicability. In efforts to combine the strengths and weaknesses of these cathode types, a multi-structure cathode (e.g., average composition $LiNi_{0.81}Mn_{0.13}Co_{0.06}O_2$) with structure transition from a bulk layered structure to LR interlayer, and to DRX surface structure has been synthesized. In addition, the chemical composition transitions from a Ni rich core to Mn rich surface to stabilize the interface with electrolyte. When integrated, the multiple structures with chemical gradient led to greatly improved cycle performance at high voltages when compared to conventional NMC811 cathode (at 2.7-4.6 V: 215 mAh g^{-1}, 89% capacity retention for MS-NMC vs 204 mAh g^{-1}, 83% for NMC811 capacity retention over 100 cycles at C/2). Advanced characterizations also demonstrate that morphology, structure, and the multi structure design is maintained after long term cycling. As a result, these promising findings open new avenues to develop cathode materials whereby multiple structure types are integrated into one particle and customized for performance application.

4.1 Introduction

Layered lithium nickel-rich oxide cathodes, $LiNi_xMn_yCo_{1-x-y}O_2$ (NMC, $x > 0.7$), are widely used in lithium-ion batteries (LIBs) for electric vehicle applications as they provide high theoretical capacity (~280 mAh g^{-1}) and working voltage (~4 V vs Li^+/Li).[6,118,119] These layered NMC cathodes structures are formed from alternating Li and two-dimensional transition metal TM oxide layers which operate by Li diffusion to and from the Li layers during discharge and charge respectively.[79, 120] When Li is extracted or inserted, a TM element such as Ni will oxidize or reduce to maintain electroneutrality.[121] This change in oxidation state will adjust the local bonding coordination around the TM at the micro scale and collectively result in structural changes at the macro scale, such as particle cracking.[12] Methods to further increase the energy density for NMC have relied on enabling high voltage operations (> 4.5 V) as more Li are extracted from the layered cathode structure when voltage is increased.[49] However, when more Li are extracted, the layered structural framework will undergo widespread structural change as more TM are oxidized and Li ions are no longer present in the layer to stabilize the structure, which leads to severe phase transitions.[122] Much of the other processes that lead to cathode failure such as particle cracking, reaction with electrolyte, gas release, and transition metal dissolution are exacerbated by this structure instability.[90] Therefore, structure instability in Li deficient layered cathodes is an intrinsic barrier to realizing high voltage operations and presents a tradeoff between energy density and cycle stability.[85]

Conventional modification methods to help stabilize layered NMC materials have included utilizing dopants, and coatings to improve particle bulk and surfaces respectively.[145] However, dopants and coatings are often redox inactive which reduces energy density and provide heterogenous coverage which reduces the efficacy of the method as many particle areas

remain unprotected.[146] Advanced chemical designs such as core-shell, concentration gradient, or full concentration designs improved upon conventional methods as they tuned the spatial control of element distribution to improve performances.[63, 64] Despite these efforts though, the advanced chemical designs do not resolve the intrinsic chemo-mechanical degradation that underlies structure instability in layered cathodes as they do not alter the intrinsic layered structure. Interestingly, other redox active cathode types such as spinel, disordered rock salt (DRX), or lithium rich (LR) are structurally coherent with layered cathode structures but are more inherently stable at higher voltages due to higher amounts of disordering between Li and TM elements.[147-149] This disordering reduces phase transitions during cycling as more Li ions can acts as pillars to intrinsically reinforce structure stability.[49] Although efforts for other cathode chemistries such as single crystal cobalt oxides have sought to integrate structures such as spinel and layered before, the methods used (e.g., coating) led to nonuniform protection and abrupt transitions between the components.[150] The efficacy of these methods would be further reduced when used on polycrystalline NMC as polycrystalline morphology could be more challenging to uniformly coat than a single crystal. Moreover, a controllable method should be able to integrate more than a single structure to enable robust performances and custom particle designs to suit application needs.

In this work, a scalable and viable concentration gradient shell method was utilized to synthesize a multi-structure NMC cathode (MS-NMC, average composition $LiNi_{0.83}Mn_{0.12}Co_{0.05}O_2$) with as designed layered NMC core in the bulk, LR interlayer, and DRX surface layer. Advanced characterizations show a gradual transition from layered to LR to DRX structure when moving from the bulk to the surface indicating the synthesis successfully integrated multiple structures within a single particle. When compared to conventional layered

NMC811 cathodes, the presence of LR and DRX structures increased capacity as they are redox active, reduced particle cracking as they undergo less structure evolution than layered structures, and reduced capacity loss as they experienced less irreversible structure transitions in particle surfaces. As a result, electrochemical performances showed significant improvements at high voltages over conventional NMC811 cathodes (at 2.7-4.6 V: 215 mAh g^{-1}, 89% capacity retention for MS-NMC vs 204 mAh g^{-1}, 83% for NMC811 capacity retention over 100 cycles at C/2). These promising results demonstrate the unique properties of MS-NMC and how robust cathode performances can be enabled by leveraging different cathode structures, which serves to inform future design of advanced cathodes.

4.2 Results and Discussion

4.2.1 Multi-Structure Design Parameters

To improve the stability and performance of NMC cathodes, alternative structures that can be integrated must be redox active and structurally coherent with the layered structure. Of the available cathode types, LR and DRX are known to operate at higher voltages (e.g., activated above 4.5 V) due to their unique structures.[121,151]

LR cathode structures rely on moderate amounts of Li occupation in TM sites to form stabilized structures that are coherent with layered cathodes.[152] However, due to the high Li content and reduced transition metal activity, particularly in LR compositions with high Mn content, redox activity proceeds through anionic pathways that are activated above 4.5 V as opposed to cationic pathways.[153] This changes the primary failure mode from chemo-mechanical degradation due to Li extraction to strain formation that is compensated by O_2 release at high voltages, which mitigates volume change during cycling and structure instability when compared

with layered structures.[154] Some studies have also demonstrated that anionic redox pathways can cycle reversibly in LR cathodes if the O_2 release is contained in the bulk and the generated gas is hindered from reaching the surface.[53] As a result, integrating the robust structural evolution of LR at higher voltages with layered cathodes can be realized if its surface dynamics can be stabilized.

Disordered cathode structures on the other hand contain extreme contents of TM and Li occupancies that interchange to form cation-disordered cathodes.[155] These highly disordered structures exhibit restricted structural movement that reduce dynamic evolution and fundamentally solve structural instability challenges at high voltages.[159] Disordered frameworks free the dependence of structural stability on Li content at high delithiation states as the mode of Li extraction (e.g., percolation) differs from ordered structures.[129,131,157,158] However, when both the bulk and surface structures are disordered, Li-ion transport pathways are obstructed and rate capabilities, as well as energy densities, are significantly reduced to levels unsuitable for commercialization.[159] Hence, it is evident that disordered structures can enable stability at high voltages but come at the cost of energy density. Therefore, when considering the strengths and weaknesses of each structure type, layered structures can enable high energy density with rate capability at the cost of structure stability, LR structures experience reduced volume expansion at the cost of surface gas release, and DRX structures can stabilize surfaces with electrolyte at the cost of energy density. Though it is clear blending the properties of these structure types can enable robust cathode materials, no synthesis method has achieved this thus far.

4.2.2 Particle Characterization in the Pristine State

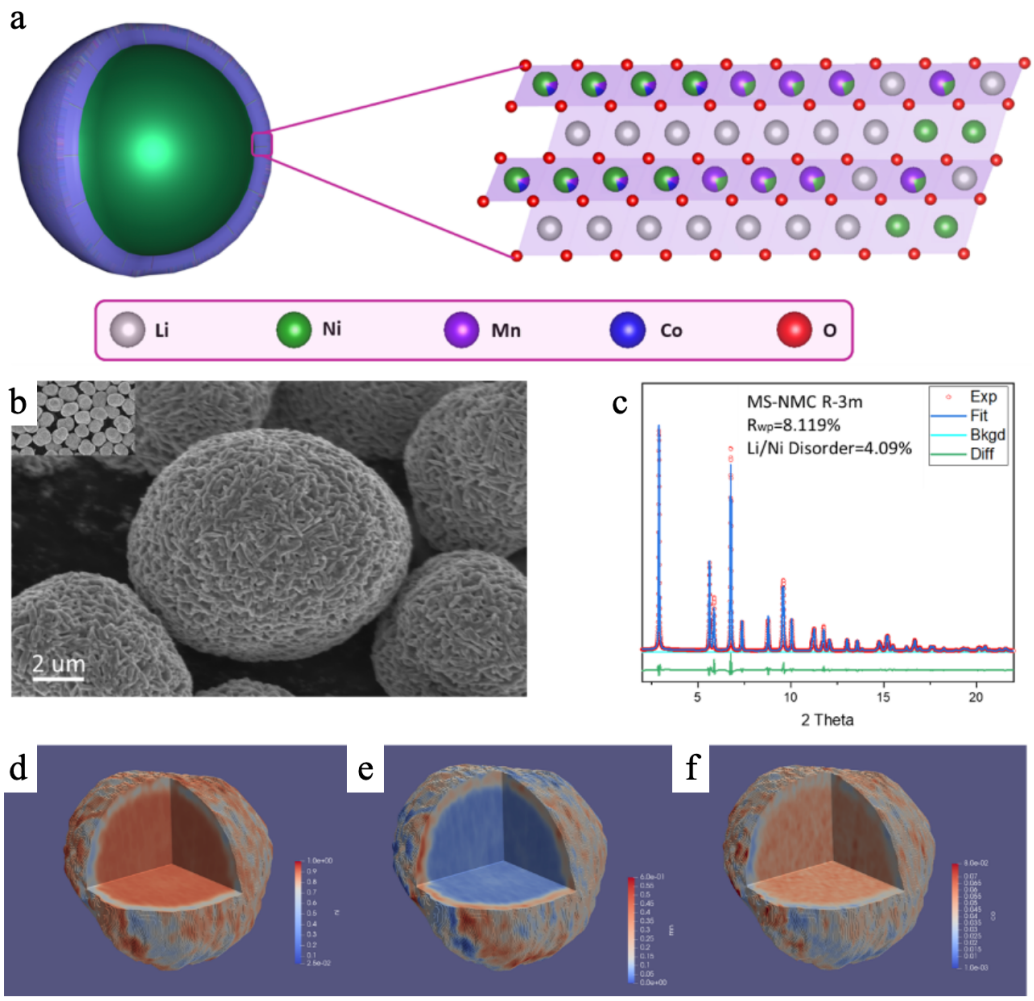

Figure 4.1. Design concept and materials characterization of MS-NMC. (a) Schematic image of MS-NMC showing bulk to surface composition and phase changes. (b) SEM image of MS-NMC. The inset shows a lower magnification of particles.(c) HEXRD and Rietveld refinement result for MS-NMC. (d, e, and f) 3D tomography reconstruction from individual secondary particles and spatial element distributions of Ni, Mn, and Co detected by fluorescence-yield scanning probe X-ray microscopy.

To realize the potential for this multi structure design in NMC cathodes (MS-NMC), co-precipitation was selected to synthesize a cathode with layered core, LR interlayer, and DRX surface. Here, Mn rich LR and DRX compositions were selected for the interlayer and surface structures as the chemical state of Mn is also more stable than Ni when in contact with electrolyte. Therefore, the as designed MS-NMC would benefit from both chemical and

structural stabilizing elements. The schematic for MS-NMC in Figure 4.1a shows a nickel-rich NMC phase in the green core that transitions to LR phase forming purple, green blend to a textured surface DRX layer in purple. The key differentiator in the surface structure is the extent of Li and TM disordering. In addition, Mn is gradually increased from the core to the outermost layer to improve cycle life and stabilize electrolyte interfaces, while the core is rich in Ni to provide high energy density and Ni is reduced towards the surface to improve stability. MS-NMC was successfully prepared using conventional co-precipitation methods as described in the Methods section. Figure 4.1b shows scanning electron microscopy (SEM) images of MS-NMC secondary particles that are spherical, dense, well layered, about 10 μm in diameter, and uniformly distributed. This morphology is ideal for co-precipitated NMC as it can maximize electrode density and indicates that designing the multi structure composition did not detrimentally affect secondary particle morphology. Quantitative composition analysis was conducted using 3D X-ray fluorescence (3D XRF) (Figure C.4.1) where an average composition of $LiNi_{0.81}Mn_{0.13}Co_{0.06}O_2$ was obtained, which is close to the designed elemental contents and indicates successful synthesis. Finally, Figure 4.1c shows a high-energy x-ray diffraction (HEXRD) curve and Rietveld refinement result for MS-NMC, where characteristic Bragg peaks for a well crystallized $NaFeO_2$ structure with R-3m symmetry are present. Namely, a strong (003) peak is visible and there is clear peak splitting between the (008)/(110) peaks that signify a well layered structure. Interestingly, the characteristic superlattice speaks associated with LR structures in low 2 theta values are not visible, which indicate that their content is not significantly high.[160] These refinement results indicate that as-prepared samples have uniform atomic occupancy and a small amount of Li/Ni disorder was detected, further confirming a well-crystallized structure.

Spatial variations in chemical composition were also investigated using 3D XRF to visualize the spatial distribution of TM elements within a secondary particle. Figure 4.1d, e, and f shows the distribution of Ni, Mn, and Co in MS-NMC where the scale bar in red indicates high chemical content of each TM and blue indicates low element content. Here, it is evident that the bulk consists of a Ni-rich core and the surface is enriched with Mn. Co is also more concentrated in the bulk and minimal amounts are present on the surface layer, which is consistent with the designed composition. These results collectively provide visual evidence at a single particle level that the multi structure design was successful in varying chemical composition and further advanced characterization was used to verify changes in structure. However, since these results are only representative of a single particle, characterizations at a bulk scale are also needed to verify the chemical distribution.

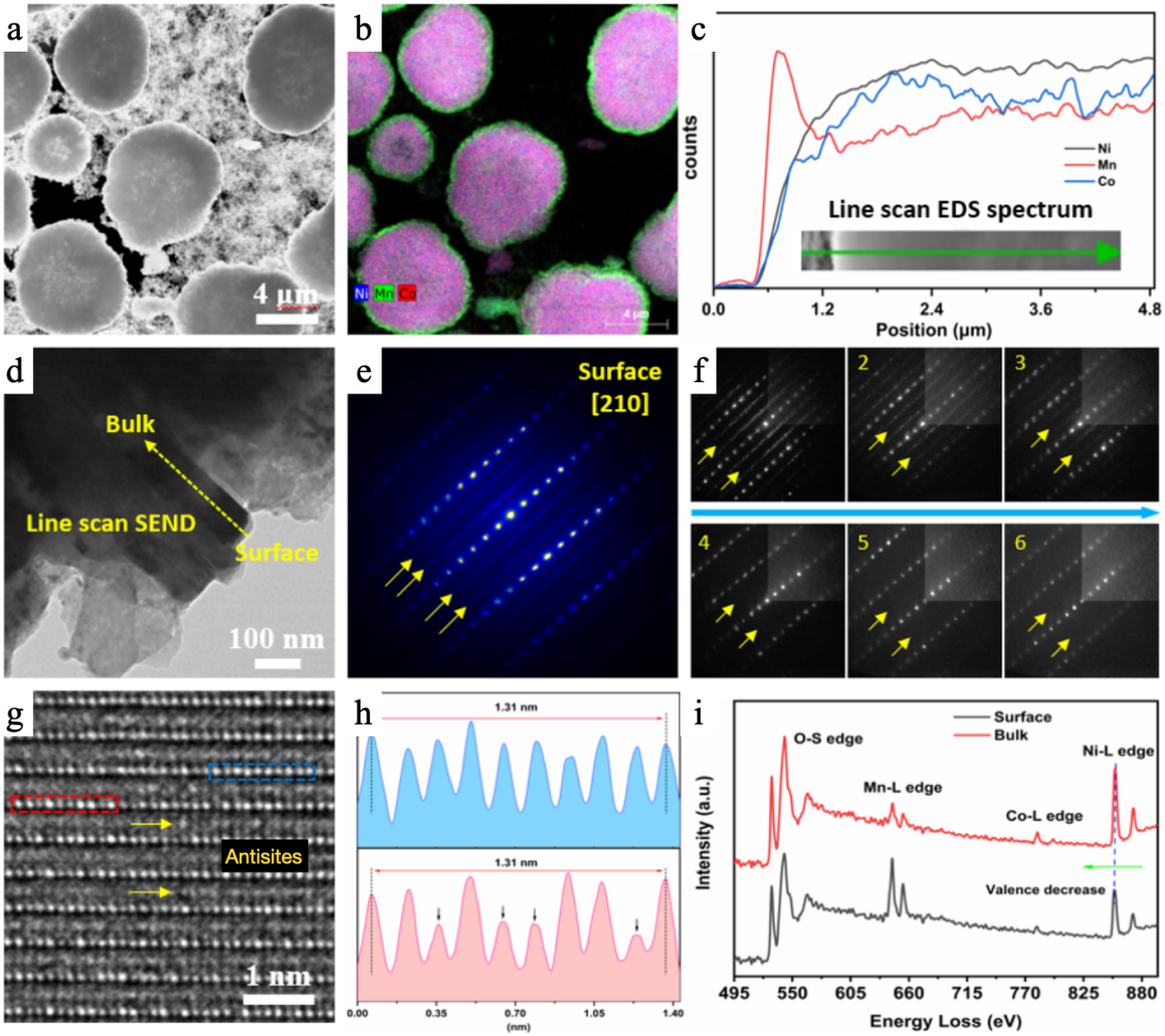

Figure 4.2. Morphology and structure in the pristine state. (a) Low magnification TEM image of MS-NMC. (b) EDS mapping showing Ni, Mn, and Co distribution in secondary particles. (c) EDS line scan for TM composition changes in a single MS-NMC secondary particle. (d) HRTEM showing SAD line scan location extending from MS-NMC surface to bulk. (e) SAED image of MS-NMC along the [210] direction. (f) Atomic level observations showing LR to layered phase transition from surface to bulk of MS-NMC. (g) HRTEM image of TM mixing in surface LR phases of MS-NMC. (h) Line scan signal counts associated with blue and red highlighted sections in c. (i) EELS scan from surface to bulk of MS-NMC.

Advanced characterizations including transmission electron microscopy (TEM) and high-resolution transmission electron microscopy (HRTEM) were then used to investigate the structure composition formed on the surface of pristine MS-NMC. Figure 4.2a and b show a low

magnification TEM of secondary particles and corresponding energy dispersive X-ray spectroscopy (EDS) mapping of elemental Ni, Mn, and Co. Most secondary particles are of uniform size and morphology. In the EDS, a distinctly homogenous Mn-rich layer less than 1 μm thick is clearly observable on a secondary particle surface of MS-NMC, while the bulk consists mostly of Ni and some Co or Mn. This corresponds with the XRF data obtained for a single particle and shows that even in a larger distribution of particles the distinct Mn enriched surfaces are successfully synthesized. A line-scan for the EDS of a single particle moving from the surface to the bulk is shown in Figure 4.2c where the chemical composition of the outer shell consists mostly of Mn. When moving towards the bulk, the intensity of Mn sharply decreases and plateaus, while Ni and Co intensities gradually increase. All these findings confirm successful co-precipitation of a chemical Ni-rich to Mn-rich transition from bulk to the surface with the as designed MS-NMC composition.

To investigate the atomic structure of this Mn-rich CGS, selected area diffraction (SAD) line scans were conducted from the surface to bulk along the [210] plane and are shown in Figure 4.2d, e, and f. In these images, bright points indicate TM elements while dark areas typically indicate lithium as they are not visible in electron based characterization methods.[129] Typical TEM of layered cathodes will show distinct rows of bright TM layers that are separated by dark spaces in between layers containing Li.[43] Interestingly, here faint elemental traces are also present between layers of bright atomic lattice points, which are characteristics of LR phases where lithium exists in the TM layer.[136] In addition, high contrast in the TM layer where some TM are much brighter than others, as shown in Figure 4.2e at the immediate surface, is an indication of DRX structure formation.[137] This is especially clear near the surface of MS-NMC as shown in Figure 4.2e. As the scan progresses from the surface to bulk (SAD scans 1-6) in

Figure 4.2f, these faint elemental traces fade and eventually are no longer visible when a pure layered phase is reached in the bulk. These findings provide evidence that structural phase changes exist in MS-NMC and it is not just the chemical composition that changes from surface to bulk. Also, these results show how bulk characterizations such as XRD shown earlier are unable to identify more localized phenomena such as the LR and DRX structures. High magnification HRTEM shown in Figure 4.2g also provide evidence of a LR phase. Surface regions of interest are enclosed with blue and red outlines where typical bright-bright lattice point patterns expected of TM layers in NMC are observable in the blue area. On the other hand, atypical bright-dark lattice point orderings are shown in the red area, which is expected for LR phase compositions due to Li site occupation in TM layers.[138] These images of the surface lattice structure corroborate that the phase structure changes when moving from surface to bulk. Associated signal counts for the blue and red regions are shown in Figure 4.2hwhere it is clear that the intensity remains consistent in the blue region TM layer, while sudden decreases occur in the red region. This further confirms the incorporation of LR phase as Li present in the TM layer of LR will decrease the intensity of the TM layer region.

Moreover, in Figure 4.2g some bright lattice points are observable in the Li layer and denoted by yellow arrows as antisites. Typically, these lattice points are associated with the formation of a rock-salt layer where Ni will usually migrate into the Li layer after cycling and exist in a 2+ oxidation state.[142] It is unusual that antisite observations are present in the pristine state of MS-NMC and suggests that a rock-salt phase was also formed during synthesis. To further investigate the chemical state of this region, electron energy loss spectroscopy (EELS) was conducted from the surface to bulk and shown in Figure 4.2i. Here, O-K edge and L edges of Ni, Mn, and Co are shown in their respective energy loss regions. It is evident that O K-edge

energy levels are higher in the bulk than in the surface, which indicate that O oxidation states are higher in the bulk. Intensities are also higher in the bulk, which signal differences in the local oxygen environment from the surface and suggests the presence of oxygen vacancies. In addition, Ni L-edge energy loss is lower at the surface than the bulk, which indicates that average Ni oxidation states are lower at the surface. Note, that lower TM valence states are typically a signature of DRX structures as the high amounts of Li content as well as Li and TM disordering reduces the valence state of TM to maintain electroneutrality.[140] These findings correspond with the real-space imaging of rock salt phases found at the surface of MS-NMC in Figure 4.2f and provide chemical evidence for their presence. Intensities of Mn L-edges are also higher at the surface whereas Co L-edges are lower in the surface indicating that Co is also at lower average oxidation state than Mn. Such results add further evidence that the as-designed chemical composition of MS-NMC was successfully synthesized, where the surface is enriched with Mn and multiple structures have formed in the bulk to surface transition. Typically, DRX phases can form during extended cycling when NMC particle surfaces are passivated by side reactions with electrolyte.[141] Given the inert nature and low reactivity of NiO rock-salt, the presence of this in the pristine state of MS-NMC may provide a stable interface with electrolyte before cycling even occurs. These characterizations however are unable to identify what specific element is present in the Li layer however prior studies have shown that Ni has a higher tendency to occupy antisites. Altogether, these structural observations collectively verify the successful formation of a DRX surface, a LR interlayer, and Ni-rich layered phase in the bulk, thus providing direct evidence of a composition where both chemical composition and structure are varied gradually in MS-NMC.

4.2.3 Electrochemical Performance

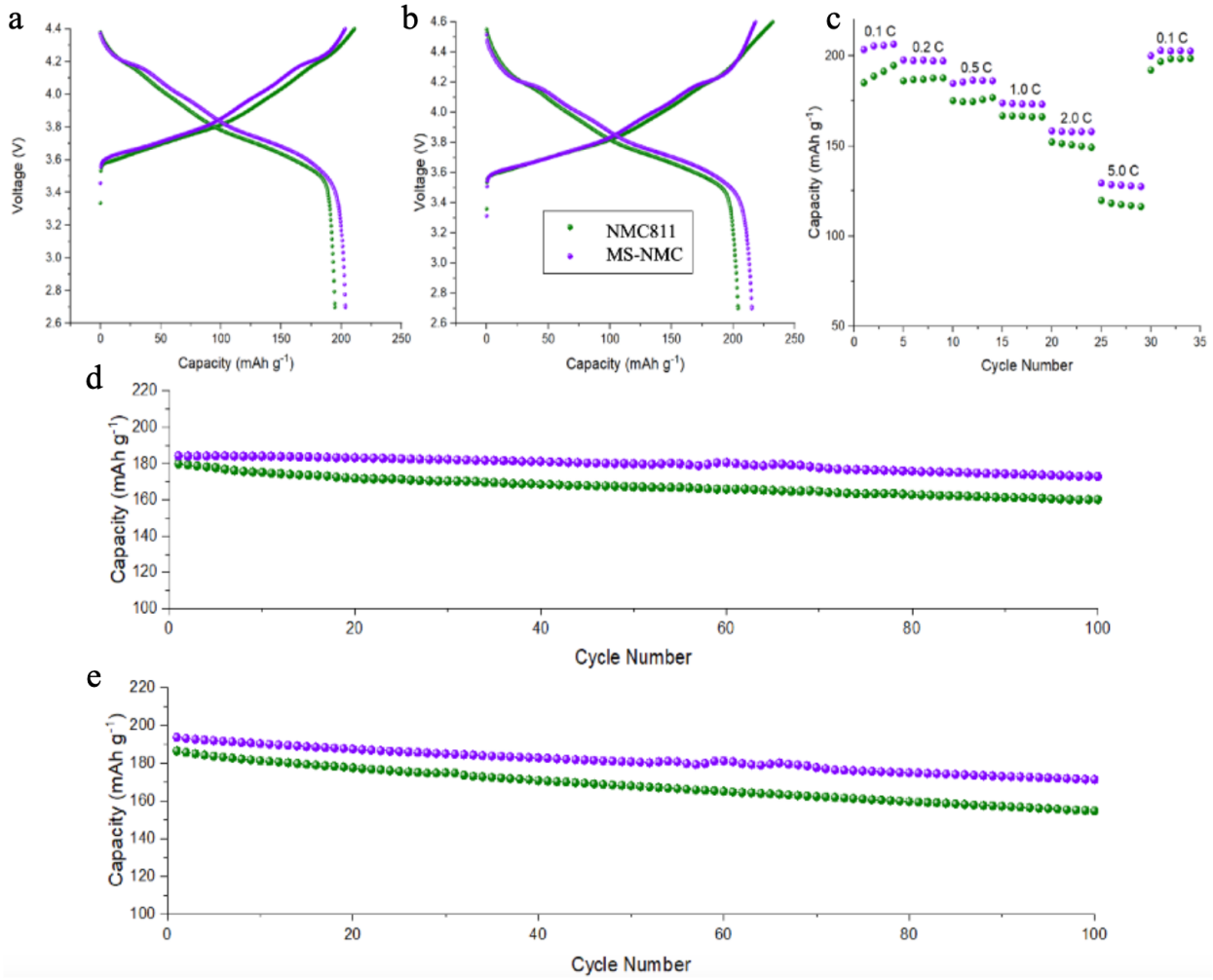

Figure 4.3. Electrochemical performance of MS-NMC and NMC811. (a and b) Initial charge/discharge profile of MS-NMC and NMC811 at 0.1C, respectively, between 2.7-4.4 V and 2.7-4.6 V.(c) Rate performance test comparing MS-NMC and NMC811. (d and e) Cycling performance of MS-NMC and NMC811 at 0.5C within 2.7-4.4 V and 2.7 – 4.6 V. Tests were conducted at 25 °C.

With clear evidence that a multi structure composition had been synthesized, electrochemical performances were compared between MS-NMC and NMC811 to quantify performance improvements. Shown in Figure 4.3a and b are the initial discharge capacities at a current rate of C/10 (1C = 200 mA g^{-1}) for MS-NMC and NMC811 (2.7-4.4 V: 208 mAh g^{-1} and 195 mAh g^{-1} in, 2.7-4.6V: 215 mAh g^{-1} and 204 mAh g^{-1} respectively). Here, MS-NMC exhibits less over-potential, particularly during discharge, which is attributed to improved electronic conductivity

and rate capability over NMC811. Figure 4.3d and e shows the cycling performance for the two cathodes at a current of C/2 within a voltage range of 2.7-4.4 V and 4.6 V for 100 cycles. Capacity retentions were recorded as 94% and 89% for MS-NMC and 89% and 83% for NMC811 at 4.4 V and 4.6 V respectively. These results are also confirmed in full cell tests at the coin cell level (Figure C.4.2-4.4) Although there was some improvement when cycled to 4.4 V, MS-NMC shows especially clear improvements at a high voltage of 4.6 V. Moreover, the rate capability of MS-NMC also seemed improve over NMC811, which may be due to primary particle morphology differences as chemical gradients have been observed to cause needle shaped primary particles that improve diffusion. (Figure 4.3c) Surprisingly, even with the LR content the voltage fade is quite low (Figure C.4.5). This indicates that the multi structure composition benefits structural reversibility in MS-NMC and dQ/dV profiles were investigated to verify. As shown in Figure C.4.6 and C.4.7, it is evident that all dQ/dV peaks of MS-NMC shift less than NMC811 when cycled to 100 cycles. Such significant shifts seen during cycling for NMC811 are indicative of poor structural reversibility that cause severe phase transitions which lead to capacity loss and less reversible Li-ion diffusion. On the other hand, minimal peak shifts observed for MS-NMC suggests that structure reversibility is maintained throughout cycles and that the structure is stable. Since LR and DRX lattice parameter changes are known to be less than that of NMC during cycling these results are expected.[161] However, characteristic plateaus above 4.5 V that are associated with anionic redox of LR structures are not visible in the charge discharge curves indicating that LR content may not be excessive. Based on these electrochemical tests, MS-NMC demonstrates robust advantages in capacity, cycle stability, and structure reversibility over NMC811. More importantly, the results provide evidence that the formed multi structure, where structure phases change from DRX to LR to layered phases,

improves upon the layered NMC phase. This new design adjusts chemical composition and structure, as opposed to only composition in the past, which pushes the boundaries of rational design strategies for Ni-rich cathode materials.

4.3.4 Chemical and Structural Stability During and After Cycling

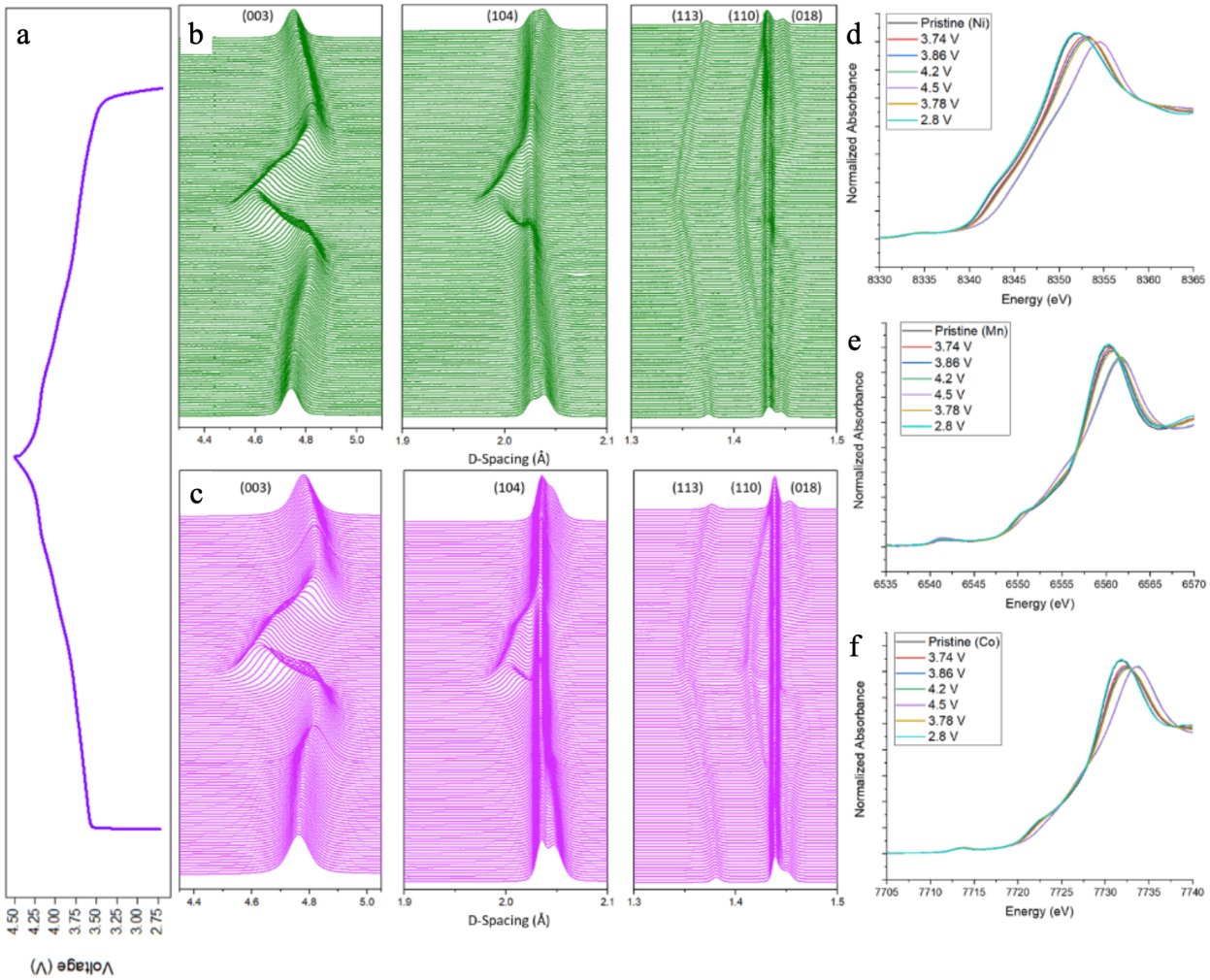

Figure 4.4. In situ structure evolution and chemical reversibility. (a) Associated charge discharge curve for the single cycle. (b and c) Two-dimensional contour plots of in situ XRD D-spacing for the structural evolution of NMC811 and MS-NMC during the initial cycle. (d, e, and f) Normalized ex-situ SXAS plots for Ni, Mn, and Co valence state changes at various charge/discharge voltages.

To investigate real-time structural evolution during cycling in MS-NMC and NMC811, in-situ high energy x ray diffraction (HEXRD) experiments were performed. Figure 4.4 and a show

two-dimensional (2D) contour plots for the structure evolutions of MS-NMC and NMC811 respectively, during the first charge-discharge at a current rate of C/10. Several characteristic peaks labeled as [003], [018]/[110] pair, and [113] are of interest. As evident in Figure 4.4b and c, both cathodes undergo similar structure evolution but the degree lattice parameters change are different. [003] peaks of both MS-NMC and NMC811 shift to a lower angle at 4.2 V and shift to a higher angle afterwards. These shifts to lower angle indicate processes that are associated with well-known H_1-M and M-H_2 phase transitions that indicate interlayer spacing have increased when Li has been extracted from the cathode.[31] Shifts back to higher angles are associated with H_2-H_3 phase transitions where the interlayer spacing decreases due to change in TM oxidation state and local coordination with O anions. Sudden changes in the lattice parameter generate lattice strain that induce intragranular and intergranular microcracks that damage particle morphology. From the experimental results, it is clear that the H_2-H_3 phase transition is less pronounced in MS-NMC than in NMC811. This indicates that MS-NMC particles undergo less severe structure evolution during cycling and are more structurally reversible, which corresponds well with the improved electrochemical performances over NMC811.

Furthermore, chemical reversibility of MS-NMC was investigated at various states of charge using ex-situ soft X-ray absorption spectroscopy (SXAS) as shown in Figure 4.4d,e, and f. Here, the K-edge x-ray absorption near edge spectroscopy (XANES) spectra for Ni, Mn, and Co are investigated. Ni K-edges spectra shift to higher energies during charge which corresponds with increases in Ni oxidation states from Ni^{2+} to Ni^{4+}. In contrast, Mn K-edges experience slight variations but shifts to higher energy values were not as pronounced as Ni. This demonstrates that Mn remains mostly 4+ during cycling which is consistent with prior findings. Co K-edges also show changes in edge shape during charge and therefore changes in bond length or

covalency. However, shifts are also not as pronounced as Ni and thus Co contributes less to capacity. Upon discharge to 2.8 V, K-edges for all TM's shift back to nearly overlap the pristine state. Based on these results, it is clear that the MS-NMC composition is chemically reversible as well as structurally reversible, which shows that the multi structure design did not affect the redox activity of TM elements.

In order to better understand the end of life state for NMC811 and MS-NMC after cycling, ex-situ postmortem focused ion beam-SEM was conducted and (FIB-SEM) images were taken, as shown in Figure 4.5a and b. Cross sectional images of pristine NMC811, after one discharge cycle to 2.7 V, and after 50 cycles are shown in Figure 4.5a. Morphologies under the same conditions for MS-NMC are shown in Figure 4.5b. As can be seen, the pristine NMC811 and MS-NMC secondary particles are densely packed by primary particles with some microcracks already present. Notably, NMC811 appears to be less dense than MS-NMC as evidenced by the presence of more microcracks. After an initial discharge cycle to 2.7 V, microcracks propagate further along NMC811 primary particles whereas MS-NMC particles undergo minimal cracking. These visual results suggest that primary particles in MS-NMC experience less volume changes during cycling, which corresponds with in-situ XRD results. Even after 50 cycles, fewer microcracks are observed in MS-NMC than in NMC811. Particularly in NMC811, the formation of macrocracks occur in the bulk and intergranular voids are formed. These cracks expose the particle core to electrolyte and parasitic side reactions will occur in the primary particles as well as secondary particle surfaces. After electrolyte exposure, rapid capacity loss and structure degradation will occur, which corresponds with electrochemical and in-situ XRD results. Clearly MS-NMC maintains structure and morphological stability better

than NMC811, which corresponds with the improved electrochemical performances and adds further evidence for the benefits of the multi structure design.

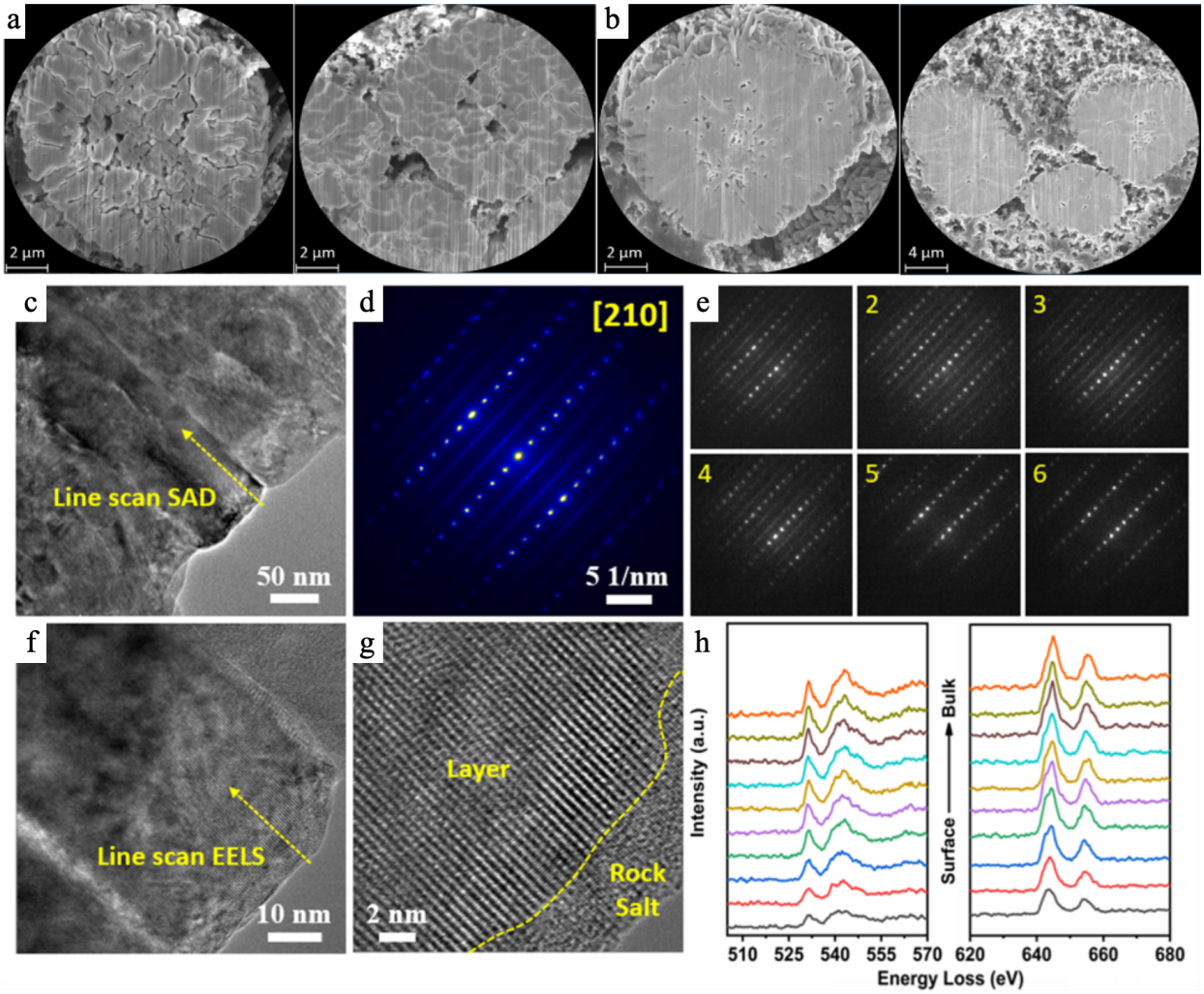

Figure 4.5. Morphology and structure after cycling. (a) SEM images of NMC811 morphology showing severe particle cracking after X cycles. (b) SEM images of MS-NMC morphology showing minimal particle cracking after X cycles. (c and f) HRTEM image of MS-NMC particle surface after 100 cycles.(d) SAD image of MS-NMC along the [210] direction after cycling. (e) Atomic level observations showing LR to layered phase transition from surface to bulk of MS-NMC after cycling. (g) HRTEM image showing change from DRX surface to LR to layered phases of MS-NMC. (h) EELS scan from surface to bulk of MS-NMC after cycling.

To further investigate MS-NMC particle structure stability, postmortem HRTEM was conducted after 100 cycles as shown in Figure 4.5c and f. Although some slight hairline fractures are visible in these images from the contrast, the overall structure is largely unchanged from the

pristine state. Line scan SAD was also conducted along the [210] plane to investigate atomic level structure changes extending from the surface to bulk, as shown in Figure 4.5d and e. In these images, the faint elemental traces present between layers of bright atomic lattice points are characteristic of LR phases where lithium exists in the TM layer.[162] As the scan progresses from the surface to bulk (SAD scans 1-6), these faint elemental traces fade and eventually are no longer visible when a pure layered phase is imaged in the bulk. These results indicate that even after cycling, the multi structure composition is well maintained in MS-NMC and the characteristic multi-phase transitions are still present. In addition, higher magnification HRTEM of particle surfaces shown in Figure 4.5g clearly shows the transition between DRX to LR to layered phase from the surface to bulk. The DRX phase does not show significant increases in thickness when compared to the pristine state, which suggests that MS-NMC surfaces were well protected by the DRX structure and fresh surfaces were not consumed by electrolyte.

Moreover, line scan EELS was conducted from the surface to bulk and results are shown in Figure 4.5h. Like the pristine state, EELS is useful for probing chemical evolution by visualizing the spectra of the oxygen K-edge (525-550 eV range) and the Mn L_3 and L_2-edges (640-660 eV range) after 100 cycles. The slight increases in O K-edge energy level when moving from surface to bulk indicate slight increases in oxidation states. Increases in the intensity of the O pre-edge peak also suggest changes in the local environment of oxygen, whereby weaker intensities observed at the surface indicate more oxygen vacancies. The energy loss of the Mn L_3 peak similarly increases when moving from surface to bulk, which indicates increases in Mn oxidation state. Lower energy loss at the surface corresponds to charge compensation owning to the presence of oxygen vacancies. These results indicate that after cycling some structure loss had occurred at the surface possibly due to oxygen loss, which reduces the average TM valence

state and can explain irreversible capacity loss observed during extended cycling. Lower TM valence states at the surface also provide chemical evidence that a DRX phase is present as TM's will have a +2 oxidation in that state. These changes in Mn L_3 and L_2 peaks are especially visible when compared to the pristine EELS shown in Figure 4.2i, where broader peaks at the surface after cycling show that particle degradation has occurred. However, when the line scan after 100 cycles extends into the bulk the increased intensities demonstrate that the LR phase is well maintained despite some degradation at the surface. When considered together with the HRTEM images showing structural evolution, these findings demonstrate that the dual-gradient composition is well maintained even after extended cycling and that the multi structure composition remains stable at interfaces with electrolyte.

4.3 Conclusion

In conclusion, a multi-structure NMC cathode was successfully synthesized by a controlled transition from layered core to LR interlayer to DRX surface structure. This combination of material structures leverages the individual strengths and weaknesses of each structure type to improve cathode performances at high voltages above 4.5 V. Here, the layered core can provide energy density and rate capability, while the LR interlayer can maintain redox activity with reduced volume change, and the DRX surface can enable structure stability. From electrochemical performance results compared to conventional NMC, surface side reactions, structure instability, and irreversible phase transitions are reduced. Moreover, this method successfully integrates a uniform layer of more than one structure type which remains yet to be achieved by conventional processes such as coating. This novel design opens new avenues for future cathode material designs and seeks to inform strategies to achieve robust performances.

4.4 Materials and Methods

4.4.1 Materials Synthesis

The secondary particle precursors of MS-NMC, and NMC811 were all synthesized via the co-precipitation method. A 4 L batch reactor was employed to synthesize all precursors. Appropriate amounts of $NiSO_4 \cdot 6H_2O$ (Sigma-Aldrich, ≥98%), $CoSO_4 \cdot 7H_2O$ (Sigma-Aldrich, ≥99%), and $MnSO_4 \cdot H_2O$ (Sigma-Aldrich, ≥99%) were used to prepare the 2.0 M starting solutions without any pre-treatments. For the precursor of NMC811, the starting solution mixture of Ni, Co, and Mn at 2.0 mol L^{-1} was pumped into the reactor under N_2 atmosphere. At the same time, 4.0 mol L^{-1} NaOH solution (aq.) and 5.0 mol L^{-1} NH_4OH solution (aq.), which acted as a chelating agent, were also pumped into the reactor. pH value of the precursor solution was kept at 11, temperature kept at 60°C, and stirring speed kept at 1000 rpm/s.

For the MS-NMC precursor, a starting solution mixture of Ni, Mn, and Co with a mol ratio of 8.9:0.5:0.6 stored in the first container was pumped into the reactor first; then, a solution of Ni and Mn with a mol ratio of 2.5:7.5 in the second container was pumped into the first container. At the same time, 4.0 mol L^{-1} NaOH solution (aq.) and 5.0 mol L^{-1} NH_4OH solution (aq.), which acted as a chelating agent, were also pumped into the reactor. pH value of the precursor solution was kept at 11, temperature kept at 60°C, and stirring speed kept at 1000 rpm/s.

The precursor powders were obtained by filtering, washing, and vacuum drying in an oven overnight. MS-NMC and NMC811 were prepared by thoroughly mixing the corresponding precursors with appropriate contents of $LiOH \cdot H_2O$. This was then followed by calcination at optimized conditions and various temperatures for 12 h: 750 ℃ for MS-NMC and 750 ℃ for NMC811, respectively.

4.4.2 Electrochemical Performance

For electrode preparation, active materials were mixed with carbon black (C45 Conductive Carbon Black, TIMCAL) and polyvinylidene fluoride (PVDF, 8%wt Solvay® 5130 PVDF binder dissolved in n-methyl-2-pyrrolidone (NMP)) at 80:10:10 wt% ratios and then followed by grinding the mixture in a mortar at 2000 r.p.m. for 9 min (3 min per time, a total of three times) in air atmosphere. The electrodes were dried at 80 °C under vacuum for 12 h to remove all traces of solvent. The 2032 type coin cells were used to prepare lithium metal cells. Celgard 2325 separators (25 μm), 1.2 M LiPF6 in EC/EMC (3:7) electrolyte (GEN II with a water content below 20 ppm, 40 μl), and Li metal foil (MTI, 16 mm × 0.6 mm (diameter × thickness), high purity of 99.9%) were used. The metal cells were then cycled vs Li+/Li and carried out in the environmental chamber at 30°C or at room temperature, using small amounts of powder (~6 mg) as positive electrodes.

4.4.3 Materials Characterization

X-ray diffraction measurement: Data of the cathode materials was collected using high-energy X-ray diffraction (HEXRD) located at sector 11-ID-C of the Advanced Photon Source at Argonne National Laboratory. A high-energy X-ray with a beam size of 0.2 mm×0.2 mm and wavelength of 0.1173 Å was used to obtain two-dimensional (2D) diffraction patterns in the transmission geometry. X-ray patterns were recorded with a Perkin-Elmer large-area detector placed at 1800 mm from the samples. Rietveld refinement of the collected HEXRD patterns were carried out using GSAS package.

In-situ time-resolved high-energy synchrotron XRD measurements during cycling were performed at the same beamline. With high penetration and low absorption, synchrotron HEXRD

precisely reflects bulk sample structure properties in real time and realistic conditions. This is beneficial when observing tiny phase changes that usually are invisible from lab scale XRD due to poor background noise and time limited resolutions. The 2032-coin cells exhibited a 3 mm hole suitable for X-rays to pass through and diffraction patterns were collected every 10 minutes.

X-ray absorption spectroscopy measurement: XANES for Ni K-edge, Mn K-edge, and Co K-edge were performed at the NSLS-II Brookhaven National Laboratory on the bending-magnet beamline 7-BM-B. X-ray photon energy was monochromatized by an Si(111) channel-cut crystal monochromator running in continuous scan mode. Higher-order harmonic contaminations were eliminated by detuning the monochromator to reduce the incident X-ray intensity by approximately 30%. All spectra were collected at room temperature in the transmission mode.

Synchrotron 3D fluorescence measurements and data analysis: 3D Nano fluorescence mapping were performed at the Hard X-ray Nanoprobe Beamline of the National Synchrotron Light Source II at Brookhaven National Laboratory. The nanoprobe experiment was carried out at 9.6 keV by focusing the coherent monochromatic X-rays down to a 50-nm spot size using a Fresnel X-ray zone plate. Tomography measurements were performed by collecting a total of 51 projections from -75° to 75°, with 3° intervals. The tomographic reconstruction was carried out using an iterative algorithm known as the algebraic reconstruction technique. Further visualization and quantification of the imaging data were carried out using the commercial software package Avizo.

Ex-situ FIB-SEM and Transmission electron microscopy measurement: The metal cells after electrochemical cycles were disassembled in an Ar-filled glove box. Subsequently, the cathode electrodes were washed immediately using dimethyl carbonate and then completely dried under

vacuum. After that, the cathode electrodes were cut into small pieces and pasted on a sample stage of FIB-SEM. Lastly, the sample stage is sealed in a jar filled with Ar gas. When transferring the sample stage into the FIB-SEM instrument, the samples will be exposed to the air for a few seconds. The cross-sectional SEM observations were conducted by a Zeiss NVision 40 FIB-SEM dual-beam system. For TEM tests, thin-section TEM specimens were prepared from each electrode foils by standard FIB lift-out procedure. The specimens were first thinned to 200 nm by a 30 kV Ga ion beam, and then further polished with a 5 kV Ga ion beam to remove damaged layers. TEM and HRTEM characterizations were conducted using the Argonne Chromatic Aberration-Corrected TEM (ACAT) (a FEI Titan 80–300 ST with an image aberration corrector to compensate for both spherical and chromatic aberrations) at an accelerating voltage of 200 kV. The 3D-rED datasets were acquired by stepwise tilting the sample with a collection angle of -40° to 40°. The tilt step was 2°. The reciprocal lattice pattern was then reconstructed using a Python script and the RED processing software package developed by Wan et al.

Chapter 5

Summary and Outlook

5.1 Dissertation Summary

Achieving low cost and high energy density NMC can enable low cost BEV with long driving range due to the significant impact that cathodes have on cost and performance.[1] However, efforts to modify NMC are ineffective as oftentimes tradeoffs between cost and energy density, cost and longevity, and energy density and longevity arise. Rather than continue modifying NMC, research efforts in the battery community have turned to developing alternative chemistries that overcome the intrinsic limitations of NMC. LR hold potential to resolve the tradeoff between cost and energy density but have been limited by voltage fade that had been thought to originate from oxygen release.[53] However, efforts to address oxygen release are ineffective, which suggests that the origin of voltage fade remain a mystery. SC cathodes on the other hand can resolve tradeoffs between energy density and longevity but are limited by increased processing costs.[45] Although removing Co from SC can reduce cost, few studies have discussed Co-free SC performances.[61] Therefore, there are clear knowledge gaps that prevent practical use of LR and SC.

In this dissertation, the discussion in chapter 2 and chapter 3 fills these knowledge gaps and inform LR and SC development. Data from advanced characterization techniques, such as BCDI or 3D rED, that span multiple length scales are used in chapter 2 to clarify the origin of oxygen release in LR cathodes and ultimately voltage fade. During cycling, material strain was found to accumulate and release due to different redox activity in composite LR structures and strategies to modify the distinct redox activity through phase modulation are proposed. For SC, the effects of Co removal are investigated in chapter 3 using nanodiffraction and x-ray

microscopy to better understand tradeoffs between cost and performance. A newly discovered LR nano domain was found to form in SC, which induced particle strain and reduced longevity at high voltages. These findings also contrast with NMC where performance at high voltages improved after Co removal and suggests that strategies to improve NMC may not directly apply to SC.[49]

Moreover, these insights from LR and SC have inspired the design of a multi structure NMC (MS-NMC) cathode as described in chapter 4. The spatial control of NMC, LR, and DRX structures in the bulk, inter layer, and surface of MS-NMC led to performances that were superior to conventional NMC. Even after long term cycling, the multi structure composition remained stable. This work is among the first to describe controlled synthesis of multi structure cathodes and serves to inspire pathways to develop other cathode material types.

5.2 Outlook and Future Work

LR, Co free SC, and MS-NMC hold potential to resolve tradeoffs faced by conventional NMC between cost and energy density, cost and longevity, and energy density and longevity. Realizing the use of these cathode materials can ultimately achieve BEV that are cheap and have long driving range. Through the work discussed in this dissertation, the origin of oxygen release and voltage fade in LR, understanding of Co free SC, and pathways to realize high voltage performance with MS-NMC have been revealed. However, despite their different intended purposes these cathode materials also share similarities.

LR, SC, and MS-NMC cathode materials are oxides that rely on Li diffusion to and from their structures to transfer charge.[12,58] In chapter 2, the understanding that strain evolution between $LiTMO_2$ and Li_2MnO_3 structure domains due to different redox activity can lead to voltage fade and oxygen release is applicable to the work discussed on SC. Since LR nano

domains were also observed in SC as discussed in chapter 3, it can be reasoned that the voltage fade and performance degradation present in Co free SC may be attributed to strain evolution of the LR nano domains. However, this understanding can also be utilized to inform material development. Although LR nano domains may be detrimental to SC performance, there may be other materials with structures that can improve performance if those materials can be formed instead of the LR nano domains. In fact, the O2 structure type proposed in chapter 2 may also be leveraged in chapter 3. Therefore, efforts to elucidate LR can also inform understanding of Co-free SC.

Moreover, the discovery of the LR nano domain in chapter 3 indicates that material composition can greatly influence structure formation, as it was unexpected that simply removing Co would form a new structure. Also in chapter 2, LiTMO2 and Li_2TMO_3 domains are structurally coherent in LR despite the high Mn content. Interestingly, its high Mn content could lower reactivity with electrolyte as Mn surface stabilization with electrolyte has been demonstrated by advanced NMC designs.[62-64] These insights were utilized in chapter 4 to synthesize, MS-NMC, where the LR interlayer and DRX surface were synthesized using a Co free precursor solution that only contained Ni and Mn. MS-NMC was designed to integrate lattice structure stability with chemical stability using materials with different structures and high Mn content. Therefore MS-NMC design is distinct from previous advanced chemical gradient designs where only chemical composition is changed when transitioning from particle bulk to surface.[62-64] Although the exact mechanism behind the structure formation is unclear, chemical composition and calcination temperature are likely key determinants. As discussed in chapter 3 and chapter 4, magnetic frustration that arises from certain chemical composition can generate site exchange defects that can change structure ordering. Temperature on the other hand must be

controlled so that element gradients are maintained and are sufficiently high enough so that structure formations can occur.[65] Interestingly, this understanding of synthesis also applies to LR and SC, which opens the possibility whereby multi structure LR or SC may also be synthesized in future work.

Additionally, much of the characterization work conducted in this dissertation relied on the use of advanced synchrotron techniques. Undoubtedly, these techniques provide newfound insights into material phenomena at length scales that have been previously unobserved, as evident in chapter 2 and chapter 3. BCDI and 3D rED were utilized to resolve the mystery surrounding voltage fade in LR while nanodiffraction and x-ray microscopy were used to identify the newly discovered LR domains present in Co free SC. Moreover, advanced in situ XRD was also applied in chapter 4 to investigate real time structure evolution of MS-NMC during cycling. Outside of the respective studies shown here, the methods may also be applied to other cathode material types such as Na ion and provide new insights on strain evolution or structure. Therefore, further development of next generation cathode materials requires the development of next generation characterization methods. In fact there are significant efforts underway to upgrade synchrotron sources and outfit them to study next generation materials.[163] The collected work in this dissertation have clearly shown how new tools can be leveraged to generate new insights and inform new development strategies.

Collectively, these three chapters on LR, Co free SC, and MS-NMC deepen the understanding of cathode materials operating at high voltages and leverage both advanced synthesis and characterization methods to do so. Material development and material understanding are undoubtedly linked, where pathways to develop better materials can only be realized by deeper understanding. In addition, it is also clear from the findings of this dissertation

how insights gained from the development of one cathode material can be used for another. Therefore, this dissertation furthers the understanding of material characteristics and material development of next generation cathode materials, which serves to enable robust cathodes that enable cheap BEV with long driving range.

As an aside, the commercial applicability of the characterization and synthesis methods utilized in this thesis to commercial settings are also of question. Battery technologies is a field where the lines between academic and commercial research interests are continually blurred and there is growing interest to translate academic ideas into practical applications faster.[18] Some aspects of this thesis, such as single particle observations described in chapter 2 and 3, would not be able to be conducted at a commercial site and the efficacy of the use of these tools would also be questionable. This is because academic work is typically conducted on gram or microgram scales even while commercial manufacturers operate at thousands of kilograms. Given this, even with the same chemistry, cathode materials in different batches can often behave differently as their synthesis conditions will not be uniform across such large quantities of material. As a result, the applicability of insights gained from advanced characterization such as BCDI or rED of one single particle to the large quantities seen at a commercial scale is unclear. Instead of relying on time consuming methods to investigate single particles, commercial settings require quick processes that can provide insights into large quantities of materials to investigate batch to batch consistency. Therefore, despite the scientific value and novel insights developed by the tools used in chapters 2 and 3, their use may be restricted to academic settings.

Similarly, the multi structure design concept described in chapter 4 would be challenging to realize in a commercial setting. This is because to integrate multiple structures the chemical concentration environment in the reactors would have to be continuously varied. This introduces

process control challenges and if the environments cannot be properly controlled between batches the performance consistency would vary widely. In addition, design targets such as structure layer thicknesses would be difficult to control as there is no straightforward method to check at mass production scales and ensure consistency across batches. Given the current landscape, this shows that the proposed multi-structure synthesis in this thesis to enable advanced cathode designs may be limited to specialty use cases where smaller batches of materials are customized for specific applications. Until the challenges with batch to batch consistency are addressed and efficient characterization methods are developed to verify consistency, the multi structure design concept may also be limited to academic use.

Nonetheless, despite the limitations on commercial applicability with the work collected in this thesis, the gathered work has undoubtedly deepened scientific understanding of cathode materials and elucidated ways to resolve tradeoffs between cost and energy density, cost and longevity, or energy density and longevity faced by conventional NMC.

References

1. Tarascon, J.M. Key challenges in future Li-battery research. *Philosophical Transactions of the Royal Society A: Mathematical, Physical and Engineering Sciences* **2010**, 368, 3327-3241.

2. Turcheniuk, K.; Bondarev, D.; Amatucci, G.; Yushin, G. Battery materials for low-cost electric transportation. *Materials Today* **2021**, 42, 57-72.

3. Catsaros, O. Lithium-ion battery pack prices hit record low of $139/kWh. *BloombergNEF* **2023**.

4. Rajaeifar, M.; Ghadimi, P.; Raugei, M.; Wu, Y.; Heidrich, O. Challenges and recent developments in supply and value chains of electric vehicle batteries: a sustainability perspective. *Resources, Conservation and Recycling* **2022**, 180, 106144.

5. U.S. DRIVE electrochemical energy storage technical team roadmap. *U.S. Council for Automotive Research* **2017**.

6. Li, M.; Lu, J.; Chen, Z.; Amine, K. 30 years of lithium-ion batteries. *Advanced Materials* **2018**, 30, 1800561.

7. Schmidt-Rohr, K. How batteries store and release energy: explaining basic electrochemistry. *Journal of Chemical Education* **2018**, 95, 1801-1810.

8. Arora, P.; Zhang, Z. Battery separators. *Chemical Reviews* **2004**, 104, 4419-4462.

9. Xu, K. Electrolytes and interphases in Li-ion batteries and beyond. *Chemical Reviews* **2014**, 114, 11503-11618.

10. Chaofeng, L.; Neale, Z.; Cao, G. Understanding electrochemical potentials of cathode materials in rechargeable batteries. *Materials Today* **2016**, 19.2, 109-123.

11. Saw, L.; Ye, Y.; Ya, A. Integration issues of lithium-ion battery into electric vehicles battery pack. *Journal of Cleaner Production* **2016**, 113, 1032-1045.

12. Manthiram, A. A reflection on lithium-ion battery cathode chemistry. *Nature Communications* **2020**, 11, 1550.

13. Daniel, C.; Mohanty, D.; Li, J.; Wood, D. Cathode Materials Review. *AIP Conference Proceedings* **2014**, 1597, 26-43.

14. Wu, F.; Yushin, G. Conversion cathodes for rechargeable lithium and lithium-ion batteries. *Energy & Environmental Science* **2017**, 2, 435-459.

15. Yoshino, A. The birth of the lithium-ion battery. *Angewandte Chemie International Edition* **2012**, 51, 5798-5800.

16. Yang, X.; Wang, C.Y. Thermally modulated lithium iron phosphate batteries for mass-market electric vehicles. *Nature Energy* **2021**, 6, 176-185.

17. Li, X.; Youlong, X.; Chunlei, W. Suppression of jahn-teller distortion of spinel $LiMn_2O_4$ cathode. *Journal of Alloys and Compounds* **479**, 1-2, 310-313.

18. Frith, J.; Lacey, M.; Ulissi, U. A non-academic perspective on the future of lithium-based batteries. *Nature Communications* **2023**, 14, 420.

19. International Energy Agency. Net zero by 2050: a roadmap for the global energy sector. *IEA* **2021**.

20. Mancini, L.; Eslava, N.; Traverso, M.; Mathieux, F. Assessing impacts of responsible sourcing initiatives for cobalt: insights from a case study. *Resources Policy* **2021**, 71, 102015.

21. National Minerals Information Center. Mineral Commodity Summaries. *U.S. Geological Survey* **2018**.

22. Ryu, H.; Sun, H.; Myung, S.; Yoon, C.; Sun, Y.K. Reducing cobalt from lithium-ion batteries for the electric vehicle era. *Energy & Environmental Science* **2021**, 2, 844-852.

23. Xu, J.; Lin, F.; Doeff, M.; Tong, W. A review of Ni-based layered oxides for rechargeable Li-ion batteries. *Journal of Materials Chemistry A* **2017**, 5, 874-901.

24. Li, W.; Erickson, E.; Manthiram, A. High-nickel layered oxide cathodes for lithium-based automotive batteries. *Nature Energy* **2020**, 5, 26-34.

25. MacNeil, D.; Lu, Z.; Dahn, J. Structure and electrochemistry of $Li[Ni_xCo_{1-2x}Mn_x]O_2$ ($0 \leq x \leq 1/2$). *Journal of the Electrochemical Society* **2002**, 149, A1332.

26. Kalyani, P.; Nalaiselvi, N. Various aspects of $LiNiO_2$ chemistry: a review. *Science and Technology of Advanced Materials* **2005**, 6, 689.

27. Kim, M.; Shin, H.; Shin, D.; Sun, Y.K. Synthesis and electrochemical properties of $Li[Ni_{0.8}Co_{0.2}]O_2$ and $Li[Ni_{0.8}Mn_{0.2}]O_2$ via co-precipitation. *Journal of Power Sources* **2006**, 159, 1328-1333.

28. Zheng, J.; Ye, Y.; Liu, T.; Xiao, Y.; Wang, C.; Wang, F.; Pan, F. Ni/Li disordering in layered transition metal oxide: electrochemical impact, origin, and control. *Accounts of Chemical Research* **2019**, 52, 2201-2209.

29. Li, M.; Lu, J. Cobalt in lithium-ion batteries. *Science* **2020**, 367, 979-980.

30. Zhou, K.; Xiz, Q.; Li, B.; Manthiram, A. An in-depth understanding of the effect of aluminum doping in high-nickel cathodes for lithium-ion batteries. *Energy Storage Materials* **2021**, 34, 229-240.

31. Bianchini, M.; Roca-Ayats, M.; Hartmann, P.; Brezesinski, T.; Janek, J. There and back again – the journey of $LiNiO_2$ as a cathode active material. *Angewandte Chemie International Edition* **2018**, 58, 10434-10458.

32. Sun, H.; Zhao, K. Electronic structure and comparative properties of $LiNi_xMn_yCo_zO_2$ cathode materials. *Journal of Physical Chemistry C* **2017**, 121, 6002-6010.

33. Tian, C.; Lin, F.; Doeff, M. Electrochemical characteristics of layered transition metal oxide cathode materials for lithium ion batteries: surface, bulk behavior, and thermal properties. *Accounts of Chemical Research* **2018**, 51, 89-96.

34. Ahaliabadeh, Z.; Kong, X.; Fedorovskaya, E.; Kallio, T. Extensive comparison of doping and coating strategies for Ni-rich positive electrode materials. *Journal of Power Sources* **2022**, 540, 231633.

35. Wang; Y.; Gao, M.; Liu, S.; Li, G.; Gao, X. Yttrium surface gradient doping for enhancing structure and thermal stability of high-Ni layered oxide as cathode for Li-ion batteries. *ACS Applied Materials & Interfaces* **2021**, 13, 7343-7354.

36. Han, B.; Key, B.; Lapidus, S.; Garcia, J.; Iddir, H.; Vaughey, J.; Dogan, F. From coating to dopant: how the transition metal composition affects alumina coatings on Ni-rich cathodes. *ACS Applied Materials & Interfaces* **2017**, 9, 41291-41302.

37. Yang, J.; Kim, H.; Ceder, G. Insights into layered oxide cathodes for rechargeable batteries. *Molecules* **2021**, 26, 3173.

38. Li, S.; Yao, Z.; Zheng, J.; Fu, M.; Cen, J.; Hwang, S.; Jin, H.; Orlov, A.; Gu, Lin.; Wang, S.; Chen, Z.; Su, D. Direct observation of defect-aided structural evolution in a nickel-rich layered cathode. *Angewandte Chemie International Edition* **2020**, 59, 22092-22099.

39. Tornheim, A.; Sharifi-Asl, S.; Garcia, J.; Bareno, J.; Iddir, H.; Shahbazian-Yassar, R.; Zhang, Z. Effect of electrolyte composition on rock salt surface degradation in NMC cathodes during high-voltage potentiostatic holds. *Nano Energy* **2019**, 55, 216-225.

40. Golubkov, A.; Fuchs, D.; Wagner, J.; Wiltsche, H.; Stangel, C.; Fauler, G.; Voitic, G.; Thaler, A.; Hacker, V. Thermal-runaway experiments on consumer Li-ion batteries with metal-oxide and olivine-type cathodes. *RSC Advances* **2014**, 4, 3633-3642.

41. Ruan, Y.; Song, X.; Fu, Y.; Song, C.; Battaglia, V. Structural evolution and capacity degradation mechanism of $LiNi_{0.6}Mn_{0.2}Co_{0.2}O_2$ cathode materials. *Journal of Power Sources* **2018**, 400, 539-548.

42. Li, T.; Yuan, X.; Zhang, L.; Song, D.; Shi, K.; Bock, C. Degradation mechanisms and mitigation strategies of nickel-rich NMC-based lithium-ion batteries. *Electrochemical Energy Reviews* **2019**, 3, 43-80.

43. Clement, R.; Lun, Z.; Ceder, G. Cation-disordered rocksalt transition metal oxides and oxyfluorides for high energy lithium-ion cathodes. *Energy & Environmental Science* **2019**, 13, 345-373.

44. Lee, J.; Seo, D.; Balasubramanian, M.; Twu, N.; Li, X.; Ceder, G. A new class of high capacity cation-disordered oxides for rechargeable lithium batteries: Li-Ni-Ti-Mo oxides. *Energy & Environmental Science* **2015**, 8, 3255-3265.

45. Qian, G.; Zhang, Y.; Li, L.; Zhang, R.; Xu, J.; Cheng, Z.; Xie, S.; Rao, Q.; He, Y.; Shen, Y.; Chen, L.; Tang, M.; Ma, Z. Single-crystal nickel-rich layered oxide battery cathode materials: synthesis, electrochemistry, and intra-granular fracture. *Energy Storage Materials* **2020**, 27, 140-149.

46. Li, H.; Liu, A.; Zhang, N.; Wang, Y.; Yin, S.; Wu, H.; Dahn, J. An unavoidable challenge for Ni-rich positive electrode materials for lithium-ion batteries. *Chemistry of Materials* **2019**, 31, 7574-7583

47. Li, J.; Downie, L.; Ma, L.; Qiu, W.; Dahn, J. Study of the failure mechanisms of $LiNi_{0.8}Mn_{0.1}Co_{0.1}O_2$ cathode material for lithium ion batteries. *Journal of the Electrochemical Society* **2015**, 162, A1401.

48. Liu, T.; Yu, L.; Lu, J.; Zhou, T.; Huang, X.; Cai, Z.; Dai, A.; Gim, J.; Ren, Y.; Xiao, X.; Holt, M.; Chu, Y.; Arslan, I.; Wen, J.; Amine, K. Rational design of mechanically robust Ni-rich cathode materials via concentration gradient strategy. *Nature Communications* **2021**, 12, 6024.

49. Liu, T.; Yu, L.; Liu, J.; Lu, J.; Bi, X.; Dai, A.; Li, M.; Li, M.; Hu, Z.; Ma, L.; Luo, D.; Zheng, J.; Wu, T.; Ren, Y.; Wen, J.; Pan, F.; Amine, K. Understanding Co roles towards developing Co-free Ni-rich cathodes for rechargeable batteries. *Nature Energy* **2021**, 6, 277-286.

50. Assat, G.; Tarascon, J.M. Fundamental understanding and practical challenges of anionic redox activity in Li-ion batteries. *Nature Energy* **2018**, 3, 373-386.

51. Grimaud, A.; Hong, W.; Shao-Horn, Y.; Tarascon, J.M. Anionic redox processes for electrochemical devices. *Nature Materials* **2016**, 15, 121-126.

52. Sathiya, M.; Rousse, G.; Ramesha, K.; Laisa, C.; Vezin, H.; Sougrati, M.; Doublet, M.; Foix, D.; Gonbeau, D.; Walker, W.; Prakash, A.; Hassine, M.; Dupont, L.; Tarascon, J.M. Reversible anionic redox chemistry in high-capacity layered-oxide electrodes. *Nature Materials* **2013**, 12, 827-835.

53. House, R.; Marie, J.; Perez-Osorio, M.; Rees, G.; Boivin, E.; Bruce, P. The role of O_2 in O-redox cathodes for Li ion batteries. *Nature Energy* **2021**, 6, 781-789.

54. Shukla, A.; Ramasse, Q.; Ophus, C.; Kepaptsoglou, D.; Hage, F.; Gammer C.; Bowling, C.; Gallegos, P.; Venkatachalam, S. Effect of composition on the structure of lithium- and manganese-rich transition metal oxides. *Energy & Environmental Science* **2018**, 11, 830-840.

55. Jarvis, K.; Deng, Z.; Allard, L.; Manthiram, A.; Ferreira, P. Atomic structure of a lithium-rich layered oxide material for lithium-ion batteries: evidence of a solid solution. *Chemistry of Materials* **2011**, 23, 3614-3621.

56. Liu, Z.; Liu, S.; Zhang, L.; Zhang, Q.; Lin, H.; Chen, C.; Hu, Z.; Yang, Y.; Ma, J.; Yu, R.; Wang, X.; Wang, Z.; Chen, L. Feasibility to improve the stability of lithium-rich layered oxides by surface doping. *ACS Applied Materials & Interfaces* **2022**, 14, 18353-18359.

57. Zhang, F.; Lou, Z.; Li, S.; Yu, Z.; Liu, Q.; Dai, A.; Cao, C.; Toney, M.; Ge, M.; Xiao, X.; Lee, W.; Yao, Y.; Deng, J.; Liu, T.; Tang, Y.; Yin, G.; Lu, J.; Su, Dong, Wang, J. Surface regulation enables high stability of single-crystal lithium-ion cathodes at high voltage. *Nature Communications*. **2020**, 11, 1-11.

58. Langdon, J.; Manthiram, A. A perspective on single-crystal layered oxide cathodes for lithium-ion batteries. *Energy Storage Materials* **2021**, 37, 143-160.

59. Bi, Y.; Tao, J.; Wu, Y.; Li, L.; Xu, Y.; Hu, E.; Wu, B.; Hu, J.; Wang, C.; Zhang, J.; Qi, Y.; Xiao, J. Reversible planar gliding and microcracking in a single-crystalline Ni-rich cathode. *Science* **2020**, 370, 1313,-1317.

60. Li, H.; Li, J.;, Zaker, N.; Zhang, N.; Botton, G.; Dahn, J. Synthesis of single crystal $LiNi_{0.88}Co_{0.09}Al_{0.03}O_2$ with a two-step lithiation method. *Journal of the Electrochemical Society* **2019**, 166, A1956.

61. Xia, Y.; Zhou, L.; Wang, K.; Lu, C.; Xiao, Z.; Mao, Q.; Lu, X.; Zhang, J.; Huang, H.; Gan, Y.; He, X.; Zhang, W.; Xia, X. Economical cobalt-free single-crystal $LiNi_{0.6}Mn_{0.4}O_2$ cathodes for high-performance lithium-ion batteries. *Journal of Solid State Electrochemistry* **2023**, 27, 1363-1372.

62. Sun, Y.K.; Myung, S.; Kim, M.; Prakash, J.; Amine, K. Synthesis and characterization of $Li[(Ni_{0.8}Co_{0.1}Mn_{0.1})_{0.8}(Ni_{0.5}Mn_{0.5})_{0.2}]O_2$ with the microscale core-shell structure as the positive electrode material for lithium ion batteries. *Journal of the American Chemical Society* **2014**, 130, 82-89.

63. Sun, Y.K.; Myung, S.; Park, B.; Prakash, J.; Belharouak, I.; Amine, K. High-energy cathode materials for long-life and safe lithium batteries. *Nature Materials* **2009**, 8, 320-324.

64. Sun, Y.K.; Chen, Z.; Noah, H.; Lee, D.; Jung, H.; Ren, Y.; Wang, S.; Yoon, C.; Myung, S.; Amine, K. Nanostructured high-energy cathode materials for advanced lithium batteries. *Nature Materials* **2012**, 11, 942-947.

65. Malik, M.; Chan, K.; Azimi, G. Review on the synthesis of $LiNi_xMn_yCo_{1-x-y}O_2$ (NMC) cathodes for lithium-ion batteries. *Materials Today Energy* **2022**, 28, 101066.

66. Wang, Z.; Yang, L.; Xu, C.; Cheng, J.; Zhao, J.; Huang, Q.; Yang, C. Advances in reactive co-precipitation technology for preparing high-performance cathodes. *Green Carbon* **2023**, 1, 193-209.

67. Tynjala, P.; Laine, P.; Valikangas, J.; Kauppinen, T.; Lassi, U. Effect of reaction conditions on the coprecipitation of $Ni(OH)_2$ for lithium-ion batteries. *Chemical Engineering & Technology* **2023**, 46, 2279-2284.

68. Hu, J.; Wang, H.; Xiao, B.; Liu, P.; Huang, T.; Li, Y.; Ren, X.; Zhang, Q.; Liu, J.; Ouyang, X.; Xun, X. Challenges and approaches of single-crystal Ni-rich layered cathodes in lithium batteries. *National Science Review* **2023**, 10, 12.

69. Liang, L.; Du, K.; Peng, Z.; Cao, Y.; Duan, J.; Jiang, J.; Hu, G. Co-precipitation synthesis of $Ni_{0.6}Co_{0.2}Mn_{0.2}(OH)_2$ precursor and characterization of $LiNi_{0.6}Co_{0.2}Mn_{0.2}O_2$ cathode material for secondary lithium ion batteries. *Electrochimica Acta* **2014**, 130, 82-89.

70. Li, J.; Zhang, N.; Li, H.; Liu, A.; Wang, Y.; Yin, S.; Wu, H.; Dahn, J. Impact of the synthesis conditions on the performance of Li $Ni_xCo_yAl_zO_2$ with high Ni and low Co content. *Journal of the Electrochemical Society* **2018**, 165, A3544.

71. Wolfman, M.; Wang, X.; Garcia, J.; Barai, P.; Stubbs, J.; Eng, Peter.; Kahvecioglu, O.; Kinnibrugh, T.; Madsen, K.; Iddir, H.; Srinivasan, V.; Fister, T. The important of surface oxygen for lithiation and morphology evolution during calcination of high-nickel NMC cathodes. *Advanced Energy Materials* **2022**, 12, 2102951.

72. Smith, A.; Dahn, J. Delta differential capacity analysis. *Journal of the Electrochemical Society* **2012**, 159, A290.

73. Dolotko, O.; Senyshyn, A.; Muhlbauer, M.; Nikolowski, K.; Ehrenberg, H. Understanding structural changes in NMC Li-ion cells by in situ neutron diffraction. *Journal of Power Sources* **2014**, 255, 197-203.

74. Lin, F.; Liu, Y.; Cheng, L.; Singer, A.; Shpyrko, O.; Xin, H.; Tamura, N.; Tian, C.; Weng, T.; Yang, X.; Meng, Y.; Nordlund, D.; Yang, W.; Doeff, M. Synchrotron x-ray analytical techniques for studying materials electrochemistry in rechargeable batteries. *Chemical Reviews* **2017**, 117, 13123-13186.

75. Qian, G.; Wang, J.; Li, H.; Ma, Z.; Pianetta, P.; Li, L.; Yu, X.; Liu, Y. Structural and chemical evolution in layered oxide cathodes of lithium-ion batteries revealed by synchrotron techniques. *National Science Review* **2022**, 9, 2.

76. Li, M.; Liu, T.; Bi, X.; Chen, Z.; Amine, K.; Zhong, C.; Lu, J. Cationic and anionic redox in lithium-ion based batteries. *Chemical Society Reviews* **2019**, 49, 1688-1705.

77. Hu, E.;, Yu, X.; Lin, R.; Bi, X.; Lu, J.; Bak, S.; Nam, K.; Xin, H.; Jaye, C.; Fischer, D.; Amine, K.; Yang, X. Evolution of redox couples in Li- and Mn-rich cathode materials and mitigation of voltage fade by reducing oxygen release. *Nature Energy* **2018**, 3, 690-698

78. Zheng, J.; Myeong, S.; Cho, W.; Yan, P.; Xiao, J.; Wang, C.; Cho, J.; Zhang, J. Li- and Mn-rich cathode materials: challenges to commercialization. *Advanced Energy Materials* **2016**, 7, 1601284.

79. Choi, J.; Aurbach, D. Promise and reality of post lithium-ion batteries with high energy densities. *Nature Reviews Materials* **2016**, 1, 1-16.

80. Sathiya, M.; Abakumov, A.; Foix, D.; Rousse, G.; Ramesha, K.; Saubanere, M.; Doublet, M.; Vezin, H.; Laisa, C.; Prakash, A.; Gonbeau, D.; Van Tendeloo, G.; Tarascon, J.M. Origin of voltage decay in high-capacity layered oxide electrodes. *Nature Materials* **2015**, 14, 230-238.

81. Pearce, P.; Perez, A.; Rousse, G.; Saubanere, M.; Batuk, D.; Foix, D.; McCalla, E.; Abakumov, A.; Van Tendeloo, G.; Doublet, M.; Tarascon, J.M. Evidence for anionic redox activity in a tridimensional-ordered-Li-rich positive electrode β-Li_2IrO_3. *Nature Materials* **2017**, 16, 580-586.

82. Hong, J.; Gent, W.; Xiao, P.; Lim, K.; Seo, D.; Wu, J.; Csernica, P.; Takacs, C.; Nordlund, D.; Sun, C.; Stone, K.; Passarello, D.; Yang, W.; Prendergast, D.; Ceder, G.; Toney, M.; Chueh, W. Metal-oxygen decoordination stabilizes anion redox in Li rich oxides. *Nature Materials* **2019**, 18, 256-265.

83. Hu, S.; Li, Y.; Peng, J.; Zhou, T.; Pang, W.; Didier, C.; Peterson, V.; Wang, H.; Li, Q.; Guo, Z. Insight of a phase compatible surface coating for long-durable Li-rich layered oxide cathode. *Advanced Energy Materials* **2019**, 9, 1901795.

84. Shang, H.; Ning, F.; Li, B.; Zuo, Y.; Lu, S.; Xia, D. Suppressing voltage decay of a lithium-rich cathode material by surface enrichment with atomic ruthenium. *ACS Applied Materials & Interfaces* **2018**, 10, 21349-21355.

85. Singer, A.; Zhang, M.; Hy, S.; Cela, D.; Fang, C.; Wynn, T.; Qiu, B.; Xia, Y.; Liu, Z.; Ulvestad, A.; Hua, N.; Wingert, J.; Liu, H.; Sprung, M.; Zozulya, A.; Maxey, E.; Harder, R.; Meng, Y.; Shpyrko, O. Nucleation of dislocations and their dynamics in layered oxide cathode materials during battery charging. *Nature Energy* **2018**, 3, 641-647.

86. Yan, P.; Zheng, J.; Tang, Z.; Devaraj, A.; Chen, G.; Amine, K.; Zhang, J.; Liu, L.; Wang, C. Injection of oxygen vacancies in the bulk lattice of layered cathodes. *Nature Nanotechnology* **2019**, 14, 602-608.

87. Assat, G.; Foix, D.; Delacourt, C.; Iadecola, A.; Dedryvere, R.; Tarascon, J.M. Fundamental interplay between anionic/cationic redox governing the kinetics and thermodynamics of lithium-rich cathodes. *Nature Communications* **2017**, 8, 1-12.

88. Luo, K.; Roberts, M.; Hao, R.; Guerrini, N.; Pickup, D.; Liu, Y.; Edstrom. K.; Guo, J.; Chadwick, A.; Duda, L.; Bruce, P. Charge-compensation in 3d-transition-metal-oxide intercalation cathodes through the generation of localized electron holes on oxygen. *Nature Chemistry* **2016**, 8, 684-691.

89. Liu, T.; Dai, A.; Lu, J.; Yuan, Y.; Xiao, Y.; Yu, L.; Li, M.; Gim, J.; Ma, L.; Liu, J.; Zhan, C.; Li, L.; Zheng, J.; Ren, Y.; Wu, T.; Shahbazian-Yassar, R.; Wen, J.; Pan, F.; Amine, K. Correlation between magnaese dissolution and dynamic phase stability in spinel-based lithium-ion battery. *Nature Communications* **2019**, 10, 1-11.

90. Xu, C.; Marker, K.; Lee, J.; Mahadevegowda, A.; Reeves, P.; Day, S.; Groh, M.; Emge, S.; Ducati, C.; Mehdi, B.; Tang, C.; Grey, C. Bulk fatigue induced by surface reconstruction in layered Ni-rich cathodes for Li-ion batteries. *Nature Materials* **2021**, 20, 84-92.

91. Xu, Z.; Jiang, Z.; Kuai, C.; Xu, R.; Qin, C.; Zhang, Y.; Rahman, M.; Wei, C.; Nordlund, D.; Sun, C.; Xiao, X.; Du, X.; Zhao, K.; Yan, P.; Liu, Y, Lin, F. Charge distribution guided by grain crystallographic orientations in polycrystalline battery materials. *Nature Communications* **2020**, 11, 1-9.

92. Ulvestad, A.; Singer, A.; Clark, J.; Cho, H.; Kim, J.; Harder, R.; Maser, J.; Meng, Y.; Shpyrko, O. Topological defect dynamics in operando battery nanoparticles. *Science* **2015**, 348, 1344-1347.

93. Qian, G.; Zhang, J.; Chu, S.; Li, J.; Zhang, K.; Yuan, Q.; Ma, Z.; Pianetta, P.; Li, L.; Jung, K.; Liu, Y. Understanding the mesoscale degradation in nickel-rich cathode materials through machine-learning-revealed strain-redox decoupling. *ACS Energy Letters*. **2021**, 6, 687-693.

94. Robinson, I.; Harder, R. Coherent x-ray diffraction imaging of strain at the nanoscale. *Nature Materials* **2009**, 8, 291-298.

95. Yoon, W.; Iannopollo, S.; Grey, C.; Carlier, D.; Gorman, J.; Reed, J.; Ceder, G. Local structure and cation ordering in O3 lithium nickel manganese oxides with stoichiometry $Li[Ni_xMn_{(2-x)/3}Li_{(1-2x)/3}]O_2$. *Electrochemical and Solid-State Letters* **2004**, 7, A167-A171.

96. Yu, H.; Ishikawa, R.; So, Y.; Shibata, N.; Kudo, T.; Zhou, H.; Ikuhara, Y. Direct atomic-resolution observation of two phases in the $Li_{1.2}Mn_{0.567}Ni_{0.166}Co_{0.067}O_2$ cathode material for lithium-ion batteries. *Angewandte Chemie International Edition* **2013**, 52, 5969-5973.

97. Leifer, N.; Penki, T.; Nanda, R.; Grinblat, J.; Luski, S.; Aurbach, D.; Goobes, G. Linking structure to performance of $Li_{1.2}Mn_{0.54}Ni_{0.13}Co_{0.13}O_2$ (Li and Mn rich NMC) cathode materials synthesized by different methods. *Physical Chemistry Chemical Physics* **2020**, 22, 9098-9109.

98. Xu, Z.; Hou, D.; Kautz, D.; Liu, W.; Xu, R.; Xiao, X.; Lin, F. Charging reactions promoted by geometrically necessary dislocations in battery materials revealed by in situ single-particle synchrotron measurements. *Advanced Materials* **2020**, 32, 2003417.

99. Jha, S.; Charalambous, H.; Okasinski, J.; Tsakalakos, T. Using in operando diffraction to relate lattice strain with degradation mechanism in a NMC battery. *Journal of Materials Science* **2019**, 54, 2358-2370.

100. Qiu, B.; Zhang, M.; Lee, S.; Liu, H.; Wynn, T.; Wu, L.; Zhu, Y.; Wen, W.; Brown, C.; Zhou, D.; Liu, Z. Metastability and reversibility of anionic redox-based cathode for high-energy rechargeable batteries.

101. Zhao, S.; Yan, K.; Zhang, J.; Sun, B.; Wang, G. Reaction mechanisms of layered lithium-rich cathode materials for high-energy lithium-ion batteries. *Angewandte Chemie International Edition* **2021**, 60, 2208-2220.

102. Strehle, B.; Kleiner, K.; Jung, R.; Chesneau, F.; Mendez, M.; Gasteiger, H.; Piana, M. The role of oxygen release from Li- and Mn-rich layered oxides during the first cycles investigated by on-line electrochemical mass spectrometry. *Journal of the Electrochemical Society* **2017**, 164, A400.

103. Nakayama, K.; Ishikawa, R.; Kobayashi, S.; Shibata, N.; Ikuhara, Y. Dislocation and oxygen-release driven delithiation in Li_2MnO_3. *Nature Communications* **2020**, 11, 1-7.

104. Rana, J.; Stan, M.; Kloepsch, R.; Li, J.; Shumacher, G.; Welter, E.; Zizak, I.; Banhart, J.; Winter, M. Structural changes in Li_2MnO_3 cathode material for Li-ion batteries. *Advanced Energy Materials* **2013**, 4, 1300998.

105. Xiao, R.; Li, H.; Chen, L. Density functional investigation on Li_2MnO_3. *Chemistry of Materials* **2012**, 24, 4242-4251.

106. Chen, H.; Islam, M. Lithium extraction mechanisms in Li-rich Li_2MnO_3 involving oxygen hole formation and dimerization. *Chemistry of Materials* **2016**, 28, 6656-6663.

107. Li, L.; Xie, Y.; Maxey, E.; Harder, R. Methods for operando coherent x-ray diffraction nto relate lattice strain with degradation mechanism in a NMC battery. *Journal of Material Science* **2019**, 54, 2358-2370.

108. Robinson, I.; Vartanyants, I.; Williams G.; Pfeifer, M.; Pitney, J. Reconstruction of the shapes of gold nanocrystals using coherent x-ray diffraction. *Physical Review Letters* **2001**, 87, 195505.

109. Maiti, S.; Sclar, H.; Sharma, R.; Vishkin, N.; Fayena-Greenstein, M.; Grinblat, J.; Talianker, M.; Burstein, L.; Solomatin, N.; Tiurin, O.; Eil, Y.; Noaked, M.; Markovskyy, B.; Aurbach, D. Understand the role of alumina, pentalithium, aluminate, and pentasodium aluminate coatings on the Li and Mn-rich NCM cathode material for enhanced electrochemical performance. *Advanced Functional Materials* **2020**, 31, 2008083.

110. Li, J.; Lin, C.; Weng, M.; Qiu, Y.; Chen, P.; Yang, K.; Huang, W.; Hong, Y.; Li, J.; Zhang, M.; Dong, C.; Zhao, W.; Xu, Zhi.; Wang, X.; Xu, K.; Sun, J.; Pan, F. Structural origin of the high-voltage instability of lithium cobalt oxide. *Nature Nanotechnology* **2021**, 5, 599-605.

111. Eum, D.; Kim, B.; Kim, S.; Park, H.; Wu, J.; Cho, S.; Yoon, G.; Lee, M.; Jung, S.; Yang, W.; Seong, W.; Ku, K.; Tamwattana, O.; Park, S.; Hwang, I.; Kang, K. Voltage decay and redox asymmetry mitigation by reversible cation migration in lithium-rich layered oxide electrodes. *Nature Materials* **2020**, 4, 419-427.

112. House, R.; Rees, G.; Perez-Osorio, N.; Marie, J.; Boivin, E.; Robertson, A.; Nag, A.; Garcia-Fernandez, M.; Zhou, K.; Bruce, P. First-cycle voltage hysteresis in Li-rich 3d cathodes associated with molecular O_2 trapped in the bulk. *Nature Energy* **2020**, 5, 777.

113. Cesernica, P.; Kalirai, S.; Gent, W.; Lim, K.; Yu, Y.; Liu, Y.; Ahn, S.; Kaili, E.; Xu, X.; Stone, K.; Marshall, A.; Sinclair, R.; Shapiro, D.; Toney, M.; Chueh, W. Persistent and partially mobile oxygen vacancies in Li-rich layered oxides. *Nature Energy* **2021**, 6, 1-11.

114. Liu, H.; Harris, K.; Jiang, M.; Wu, Y.; Goward, G.; Botton, G. Unraveling the rapid performance decay of layered high-energy cathodes: from nanoscale degradation to drastic bulk evolution. *ACS Nano* **2018**, 12, 2708-2718

115. Boulineau, A.; Simonin, L.; Colin, J.; Bourbon, C.; Patoux, S. First evidence of manganese-nickel segraegation and densification upon cycling in Li-rich layered oxides for lithium batteries. *Nano Letters* **2013**, 13, 3857-3863.

116. Teufl, T.; Strehle, B.; Muller, P.; Gasteiger, H.; Mendez, M. Oxygen release and surface degradation of Li- and Mn-rich layered oxides in variation of the Li_2MnO_3 Content. *Journal of the Electrochemical Society* **2018**, 165, A2718-A2731.

117. Chen, Z.; Li, J.; Zheng, X. Unraveling oxygen evolution in Li-rich oxides: a unified modeling of the intermediate peroxo/superoxol-like dimers. *Journal of the American Chemical Society* **2019**, 141, 10751-10759.

118. Armand, M.; Tarascon, J.M. Building better batteries. *Nature* **2008**, 451, 652-657.

119. Chu, S.; Cui, Y.; Liu, N. The path towards sustainable energy. *Nature Materials* **2017**, 16, 16-22.

120. Nitta, N.; Wu, F.; Lee, J.; Yushin, G. Li-ion battery materials: present and future. *Materials Today* **2015**, 18,252-264.

121. Liu. T.; Liu, J.; Li, L.; Yu, L.; Diao, J.; Zhou, T.; Li, S.; Dai, A.; Zhao, W.; Xu, S.; Ren, Y.; Wang, L.; Wu, T.; Qi, R.; Xiao, Y.; Zheng, J.; Chao, W.; Harder, R.; Robinson, I.; Wen, J.; Lu, J.; Pan, F.; Amine, K. Origin of structural degradation in Li-rich layered oxide cathode. *Nature* **2022**, 606, 305-213.

122. Liu, T.; Lin, L.; Bi, X.; Tian, L.; Yang, K.; Liu, J.; Li, M.; Chen, Z.; Lu, J.; Amine, K.; Xu, K.; Pan, F. In situ quantification of interphasial chemistry in Li-ion battery. *Nature Nanotechnology* **2019**, 1, 50-56.

123. Thackeray, M.; Amine, K. Layered Li-Ni-Mn-Co oxide cathodes. *Nature Energy* **2021**, 6, 933.

124. Zhang, R.; Wang, C.; Zou, P.; Lin, R.; Ma, L.; Yin, L.; Li, T.; Xu, W.; Jia, H.; Li, Q.; Sainio, S.; Kisslinger, K.; Trask, S.; Ehrlich, S.; Yang, Y.; Kiss, A.; Ge, M.; Polzin, B.; Lee, S.; Xu, W.; Ren, Y.; Lin, H. Compositionally complex doping for zero-strain zero-cobalt layered cathodes. *Nature* **2022**, 610, 67-73.

125. Wang, L.; Liu, T.; Wu, T.; Lu, J. Strain-retardant coherent perovskite phase stabilized Ni-rich cathode. *Nature* **2022**, 611, 61-67.

126. Lin, F.; Nordlund, D.; Li, Y.; Quan, M.; Cheng, L.; Weng, T.; Liu Y.; Xin, H.; Doeff, M. Metal segregation in hierarchically structured cathode materials for high-energy lithium batteries. *Nature Energy* **2016**,1, 1-8.

127. Yoon, M.; Dong, Y.; Hwang, J.; Sung, J.; Cha, H.; Ahn, K.; Huang, Y.; Kang, S.; Li, J.; Cho, J. Reactive boride infusion stabilizes Ni-rich cathodes for lithium-ion batteries. *Nature Energy* **2021**, 6, 362-371.

128. Gao, H.; Cai, J.; Xu, G.; Li, L.; Ren, Y.; Meng, X.; Amine, K.; Chen, Z. Surface modification for suppressing interfacial parasitic reactions of a nickel-rich lithium-ion cathode. *Chemistry of Materials* **2019**, 31, 2723-2730.

129. Lee, J.; Urban, A.; Li, X.; Su, D.; Hautier, G.; Ceder, G. Unlocking the potential of cation-disordered oxides for rechargeable lithium batteries. *Science* **2014**, 6170, 519-522.

130. Shukla, A.; Ramasse, Q.; Ophus, C.; Duncan, H.; Hage, F.; Chen, G. Unravelling structural ambiguities in lithium- and manganese-rich transition metal oxides. *Nature Communications* **2015**, 6, 8711.

131. Ji, H.; Wu, J.; Cai, Z.; Liu, J.; Kwon, D.; Kim, H.; Urban, A.; Papp, J.; Foley, E.; Tian, Y.; Balasubramanian, M.; Kim, H.; Clement, R.; McCloskey, B.; Yang, W.; Ceder, G. Ultrahigh power and energy density in partially ordered lithium-ion cathode materials. *Nature Energy* **2020**, 5, 213-221

132. Zhao, W.; Zheng, J.; Zou, L.; Jia, H.; Liu, B.; Wang, H.; Engelhard, M.; Wang, C.; Xu, W.; Yang, Y.; Zhang, J. High voltage peration of Ni-rich NMC cathodes enabled by stable electrode/electrolyte interphases. *Advanced Energy Materials* **2018**, 8, 1800297.

133. Xue, W.; Huang, M.; Li, Y.; Zhu, Y.; Gao, R.; Xiao, X.; Zhang, W.; Li, S.; Xu, G.; Yu, Y.; Li, P. Lopez, J.; Yu, D.; Dong, Y.; Fan, W.; Shi, Z.; Xiong, R.; Sun, C.; Hwang, I.; Lee, W.; Shao-Horn, Y.; Johnson, J.; Li, J. Ultra-high-voltage Ni-rich layered cathodes in practical Li metal batteries enabled by a sulfonamide-based electrolyte. *Nature Energy* **2021**, 6, 495-505.

134. Tan, S.; Shadike, Z.; Li, J.; Wang, X.; Yang, Y.; Lin, R.; Cresce, A.; Hu, J.; Hunt, A.; Waluyo, I.; Ma, L.; Monaco, F.; Cloetens.; Xiao, J.; Liu, Y.; Yang, X.; Xu, K.; Hu, E. Additive engineering for robust interphases to stabilize high-Ni layered structures at ultra-high voltages of 4.8 V. *Nature Energy* **2022**, 7, 484-494.

135. Xu, J.; Zhang, J.; Pollard, T.; Li, Q.; Tan, S.; Hou, S.; Wang, H.; Chen, F.; He, H.; Hu, E.; Xu, K.; Yang, X.; Borodin, O.; Wang, C. Electrolyte design for Li-ion batteries under extreme operating conditions. *Nature* **2023**, 7949, 694-700.

136. Cheng, X.; Li, Y.; Cao, T.; Wu, R.; Wang, M.; Liu, H.; Liu, X.; Lu, J.; Zhang, Y. Real-time observation of chemomechanical breakdown in a layered nickel-rich oxide cathode realized by in situ scanning electron microscopy. *ACS Energy Letters* **2021**, 6, 1703-1710.

137. Heenan, T.; Wade, A.; Tan, C.; Parker, J.; Matras, D.; Leach, A.; Robinson, J.; Llewellyn, A.; Dimitrijevic, A.; Jervis, R.; Quinn, P.; Brett, D.; Shearing, P. Identifying the origins of microstructural defects such as cracking within Ni-rich NMC811 cathode particles for lithium-ion batteries. *Advanced Energy Materials* **2020**, 10, 2002655.

138. Yan, P.; Zheng, J.; Gu, M.; Xiao, J.; Zhang, J.; Wang, C. Intragranular cracking as a critical barrier for high-voltage usage of layer-structured cathode for lithium ion batteries. *Nature Communications* **2017**,8, 14101.

139. Wang, L.; Lei, X.; Liu, T.; Dai, A.; Su, D.; Amine, K.; Lu, J.; Wu, T. Regualtion of surface defect chemistry toward stable Ni-rich cathodes. *Advanced Materials* **2022**, 19, 2200744.

140. Satish, R.; Wichmann, L.; Crafton, M.; Giovine, R.; Li, L.; Ahn, J.; Yue, Y, Tong, W.; Chen, G.; Wang, C.; Clement, R.; Kostecki, R. Exposure history and its effect towards stabilizing Li exchange across disordered rock salt interfaces. *ChemElectroChem* **2021**, 8, 3982-3991.

141. Xiao, B.; Sun, X. Surface and subsurface reactions of lithium transition metal oxide cathode materials: an overview of the fundmanetal origins and remedying approaches. *Advanced Energy Materials* **2018**, 8, 1802057.

142. Qiao, R.; Liu, J.; Kourtakis, K.; Roelofs, M.; Peterson, D.; Duff, J.; Deibler, D.; Wray, L.; Yang, W. Transition-metal redox evolution in $LiNi_{0.5}Mn_{0.3}Co_{0.2}O_2$ electrodes at high potentials. *Journal of Power Sources* **2017**, 360, 294-300.

143. Gent, W.; Lim, K.; Liang, Y.; Li, Q.; Barnes, T.; Ahn, S.; Stone, K.; McIntire, M.; Hong, J.; Song, J.; Li, Y.; Mehta, A.; Ermon, S.; Tyliszczak, T.; Kilcoyne, D.; Park, J.; Doo, S.; Toney, M.; Yang, W.; Prendergast, D.; Chueh, W. Coupling between oxygen redox and cation migration explains unusual electrochemistry in lithium-rich layered oxide cathodes. *Nature Communications* **2017**, 8, 2091.

144. Li, J.; Sharma, N.; Jiang, Z.; Yang, Y.; Monaco, F.; Xu, Z.; Hou, D.; Ratner, D.; Pianetta, P.; Cloetens, P.; Lin, F.; Zhao, K.; Liu, Y. Dynamics of particle network in composite battery cathodes. *Science* **2022**, 376, 517-521.

145. Xu, G.; Liu, X.; Daali, A.; Amine, R.; Chen, Z.; Amine, K. Challenges and strategies to advance high-energy nickel-rich layered lithium transition metal oxide cathodes for harsh operation. *Advanced Functional Materials* **2020**, 30, 2004748.

146. Nisar, U.; Muralidharan, N.; Essehli, R.; Amin, R.; Belharouak, I. Valuation of surface coatings in high-energy density lithium-ion battery cathode materials. *Energy Storage Materials* **2021**, 38, 309-328.

147. Kim, D.; Sandi, G.; Croy, J.; Gallagher, K.; Kan, S.; Lee, E.; Slater, M.; Johnson, C.; Thackeray, M. Composite 'layered-layered-spinel' cathode structures for lithium-ion batteries. *Journal of the Electrochemical Society* **2012**, 160, A31.

148. Wang, R.; Li, X.; Liu, L.; Lee, J.; Seo, D.; Bo, S.; Urban, A.; Ceder, G. A disordered rock-salt Li-excess cathode material high capacity and substantial oxygen redox activity: $Li_{1.25}Nb_{0.25}Mn_{0.5}O_2$. *Electrochemistry Communications* **2015**, 60, 70-73.

149. Croy, J.; Guiterrez, A.; He, M.; Yonemoto, B.; Lee, E.; Thackeray, M. Development of manganese-rich cathodes as alternatives to nickel-rich chemistries. *Journal of Power Sources* **2019**, 434, 226706.

150. Zhu, Z.; Yu, D.; Shi, Z.; Gao, R.; Xiao, X.; Waluyo, I.; Ge, M.; Dong, Y.; Xue, W.; Xu, G.; Lee, W.; Hunt, A.; Li, J. Gradient-morph $LiCoO_2$ single crystals with stabilized energy density above 3400 Wh L^{-1}. *Energy & Environmental Science* **2020**, 13, 1865-1878.

151. Lun, Z.; Ouynag, B.; Kwon, D.; Ha, Y.; Foley, E.; Huang, Y.; Cai, Z.; Kim, H.; Balasubramanian, M.; Sun, Y.; Huang, J.; Tian, Y.; Kim, H.; McCloskey, B.; Yang, W.; Clement, R.; Ji, H.; Ceder, G. Cation-disordered rocksalt-type high-entropy cathodes for Li-ion batteries. *Nature Materials* **2021**, 2, 214-221.

152. Gallgher, K.; Croy, J.; Balasubramanian, M.; Bettge, M.; Abraham, D.; Burrell, A.; Thackeray, M. Correlating hysteresis and voltage fade in lithium- and manganese-rich layered transition-metal oxide electrodes. *Electrochemistry Communications* **2013**, 33, 96-98.

153. Wang, L.; Dai, A.; Xu, W.; Lee, S.; Cha, W.; Harder, R.; Liu, T.; Ren, Y.; Yin, G.; Zuo, P.; Wang, J.; Lu, J.; Wang, K. Structural distortion induced by manganese activation in a

lithium-rich layered cathode. *Journal of the American Chemical Society* **2020**, 35, 14966-14973.

154. Wang, L.; Liu, T.; Dai, A.; Andrade, V.; Ren, Y.; Xu, W.; Lee, S.; Zhang, Q.; Gu, L.; Wang, S.; Wu, T.; Jin, H.; Lu, J. Reaction inhomogeneity coupling with metal rearrangement triggers electrochemical degradation in lithium-rich layered cathode. *Nature Communications* **2021**, 12, 5370.

155. Cai, Z.; Ouyang, B.; Hau, H.; Chen, T.; Giovine, R.; Koirala, K.; Li, L.; Ji, H.; Ha, Y.; Sun, Y.; Huang, J.; Chen, Y.; Wu, V.; Yang, W.; Wang, C.; Clement, R.; Lun, Z.; Ceder, G. In situ formed partially disordered phases as earth-abundant Mn-rich cathode materials. *Nature Energy* **2024**, 9, 27-36.

156. Lun, Z.; Ouyang, B.; Cai, Z.; Clement, R.; Hwan, D.; Huang, J.; Papp, J.; Balasubramanian, M.; Tian, Y.; McCloskey, B.; Ji, H.; Kim, H.; Kitchaev, D.; Ceder, G. Design principles for high-capacity Mn-based cation-disordered rocksalt cathodes. *Chem* **2020**, 6, 153-168.

157. Cai, Z.; Zhang, Y.; Lun, Z.; Ouyang, B.; Gallington, L.; Sun, Y.; Hau, H.; Chen, Y.; Scott, M.; Ceder, G. Thermodynamically driven synthetic optimization for cation-disordered rock salt cathodes. *Advanced Energy Materials* **2022**, 12, 2103923.

158. Huang, J.; Zhong, P.; Ha, Y.; Kwon, D.; Crafton, M.; Tian, Y.; Balasubramanian, M.; McCloskey, B.; Yang, W.; Ceder, G. Non-topotactic reactions enable high rate capability in Li-rich cathode. *Nature Energy* **2021**, 6, 706-714.

159. Kitchaev, D.; Lun, Z.; Richards, W.; Ji, H.; Clement, R.; Balasubramanian, M.; Kwon, D.; Dai, K.; Papp, J.; Lei, T.; McCloskey, B.; Yang, W.; Lee, J.; Ceder, G. Design principles for high transition metal capacity in disordered rocksalt Li-ion cathodes. *Energy & Environmental Science* **2018**, 11, 2159-2171

160. Wei, Z.; Zhi, Z.; Wen, X.; Li, X.; Qiu, B.; Gu, Q.; Sun, J.; Han, Y.; Luo, H.; Guo, H.; Xia, Y.; Yin, C.; Cai, P.; Liu, Z. Eliminating oxygen releasing of Li-rich layered cathodes by tuning the distribution of superlattice domain. *Materials Today Energy* **2022**, 27, 1001039.

161. Cui, S.; Gao, M.; Li, G.; Gao, X. Insights into Li-rich Mn-based cathode materials with high capacity: from dimension to lattice to atom. *Advanced Energy Materials* **2021**, 12, 2003885.

162. Dixit, H.; Zhou, W.; Idrobo, J.; Nanda, J.; Cooper, V. Facet-dependent disorder in pristine high-voltage lithium-manganese-rich cathode material. *ACS Nano* **2014**, 8, 12710-12716.

163. Shin, S. New era of synchrotron radiation: fourth-generation storage ring. *AAPS Bulletin* **2021**, 31, 21.

Appendix

Appendix A: Supporting Information for Chapter 2

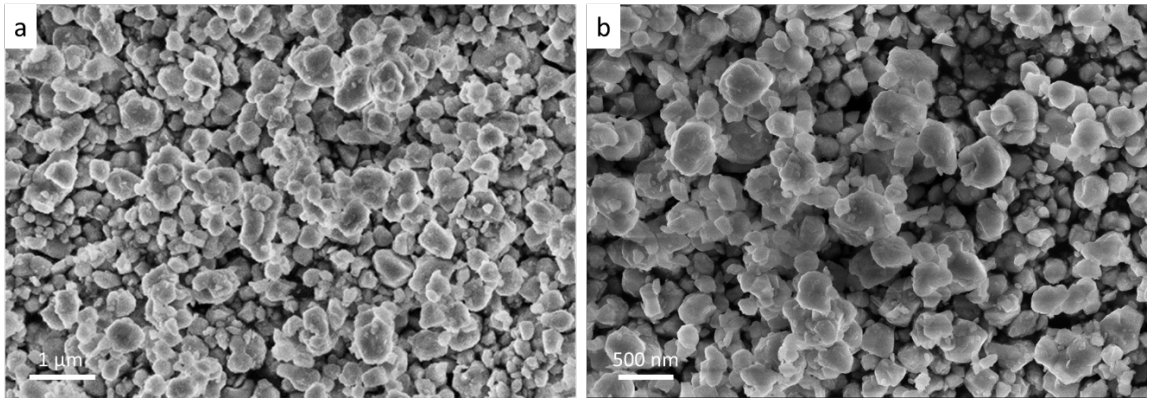

Figure A.2.1. The SEM image of the LMR powder. The particle size ranges from 200-600 nm, which is ideal for the BCDI measurement.

$Li_{1.2}Ni_{0.13}Mn_{0.54}Co_{0.13}O_2$ used in this paper is one of the most representative compositions for Li- and Mn-rich layered oxides and has been frequently used as a model material for mechanism understanding in many previous works.[1-10]

Synthesis of primary particle, rather than secondary particles, was purposefully controlled for minimizing interference from morphological factors. Figure A.2.1 shows a single-particle morphology with sizes ranging from 200 to 600 nm, which is an ideal size for the Bragg coherent diffraction imaging (BCDI) measurements. Data in Figure A.2.4 confirms that the composition of as-prepared sample was close to the designed composition.

The electrochemical behaviors (Figure A.2.1b) including the shape of charge-discharge profiles, capacity performance and voltage decays all represent the typical behaviors of Li- and Mn-rich layered oxides.

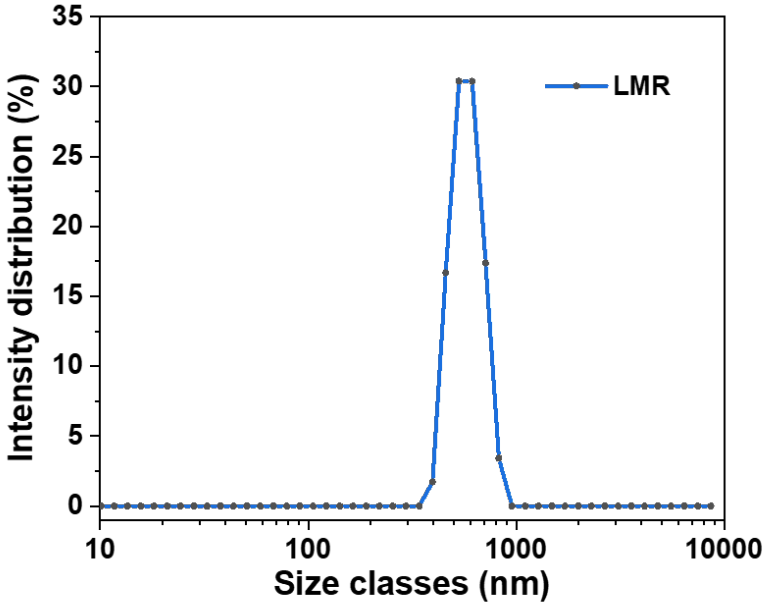

Figure A.2.2. The particle size distribution of the as-prepared LMR cathode. The particle size distribution of as prepared $Li_{1.2}Ni_{0.13}Mn_{0.54}Co_{0.13}O_2$ is analyzed using Zetasizer Nano ZS90. The mean particle size of LMR cathode is around 583 nm.

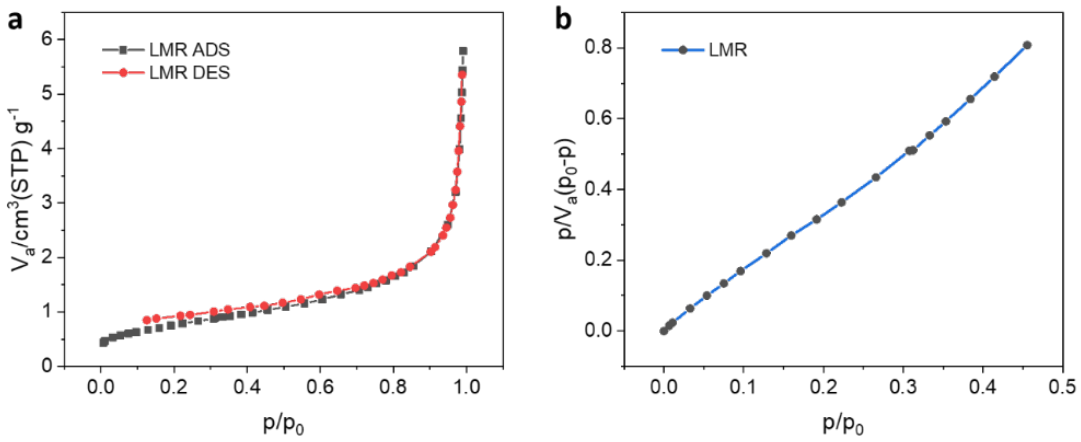

Figure A.2.3. Nitrogen physisorption analysis of LMR. (a) The nitrogen adsorption/desorption isotherm of LMR. (b) The corresponding BET plot of LMR. The specific surface area of the as prepared LMR cathode is characterized by a nitrogen physisorption analysis experiment and calculated using the Brunauer-Emmett-Teller (BET) model. The nitrogen adsorption/desorption isotherm and the corresponding BET plot of the as-prepared LMR cathode indicate that its specific surface area is calculated to be 2.804 $m^2\ g^{-1}$.

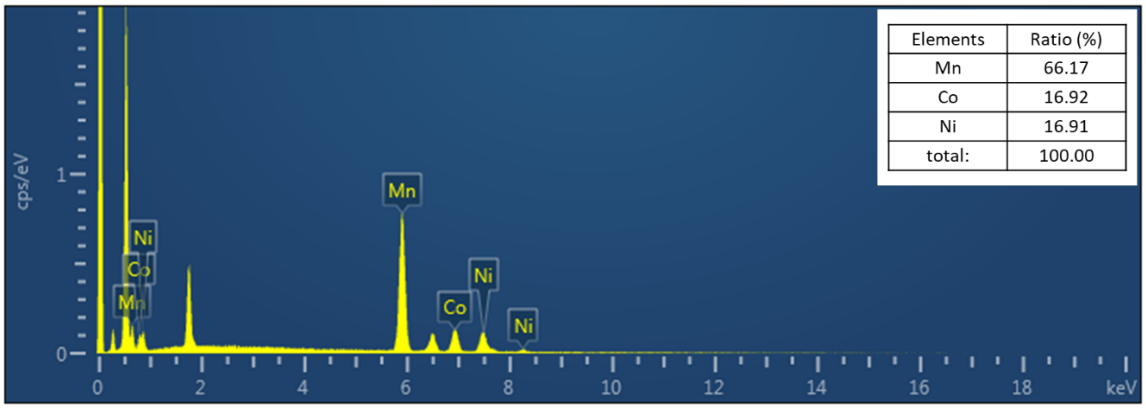

Figure A.2.4. SEM-EDS results of the pristine LMR cathode. The actual chemical composition complies well with the design (Mn : Co : Ni = 4 : 1 : 1).

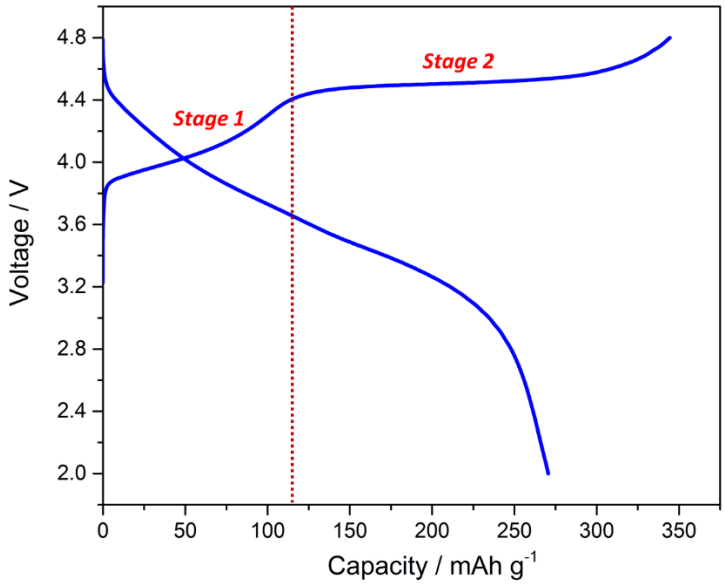

Figure A.2.5. The first charge/discharge curve of LMR cathode. The first charge profile exhibits two distinct electrochemical stages at different voltage ranges. Stage 1 corresponds to the Li^{+} extraction (de-lithiation) from $LiTMO_2$ domains with concomitant oxidation of Ni^{2+} and Co^{2+}. Stage 2 corresponds to the activation of Li_2MnO_3 domains, further Li+ extraction and at this stage oxygen is oxidized (at high potentials) to per-oxo species: $(2O^{2-} \leftrightarrow [O2]^{2-} + 2e^{-})$.

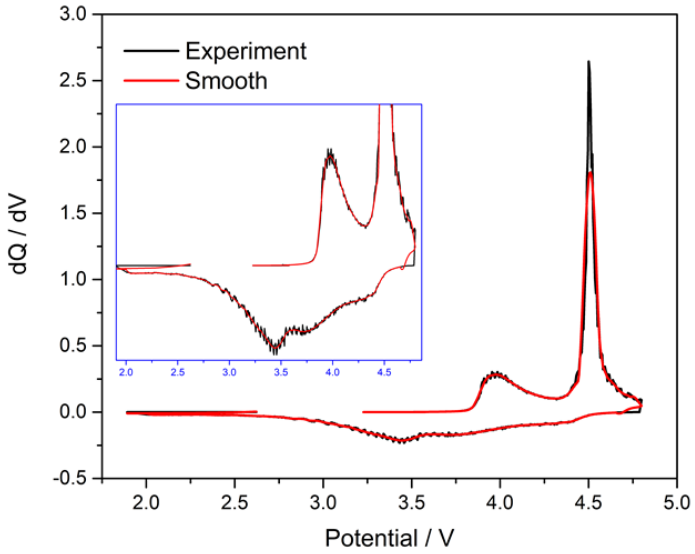

Figure A.2.6. The corresponding dQ/dV curve of the first charge/discharge curve. The dQ/dV curve of the first charge exhibits two oxidation peaks at different voltage ranges. The broad peak at 4.0 V corresponds to the oxidation of Ni and Co in $LiTMO_2$ domains. The sharp peak at 4.5 V corresponds to the activation of Li_2MnO_3 domains.

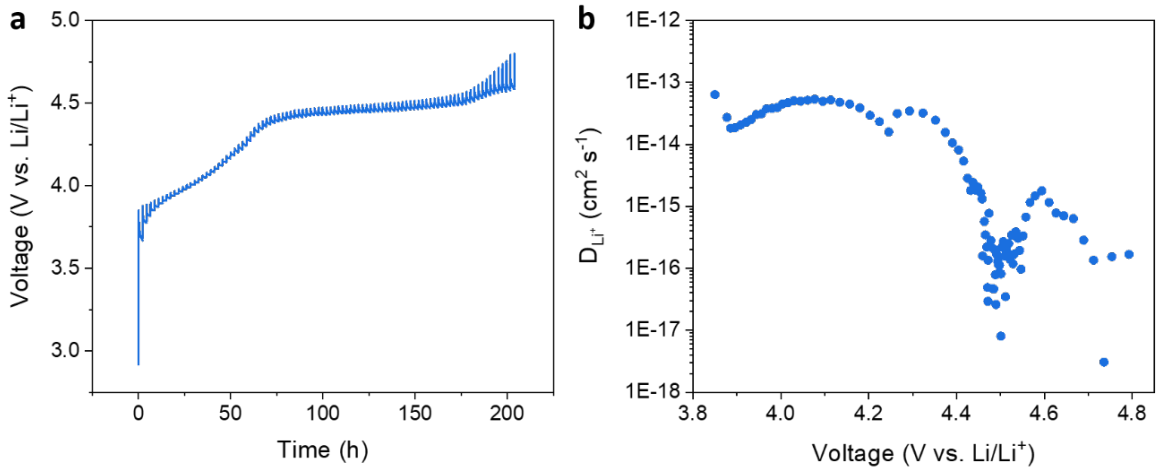

Figure A.2.7. The galvanostatic intermittent titration technique (GITT) test of the first charge. (a) The voltage profile derived from the GITT test. (b) Li ion diffusion coefficients during the first charge. The Li-ion diffusion coefficient keeps stable in stage 1 but dramatically decreases after the activation of Li_2MnO_3 domains (stage 2).

The Galvanostatic Intermittent Titration Technique (GITT) measurement was performed by periodically pulsing and relaxing the battery between 2.0 and 4.8 V using a NEWARE electrochemical analyzer with a 10 min pulse at 25 mA g-1 followed by 2 h relaxation every step. The Li+ diffusion coefficient (DLi+) was calculated using Equation (1):

$$D_{Li^+} = \frac{4}{\pi\tau}\left(\frac{R_s}{3}\right)^2\left(\frac{\Delta E_s}{\Delta E_t}\right)^2 \quad \text{(A2.1)}$$

in which τ is the pulse time of 600 s and Rs is particle equivalent radius of 200 nm.

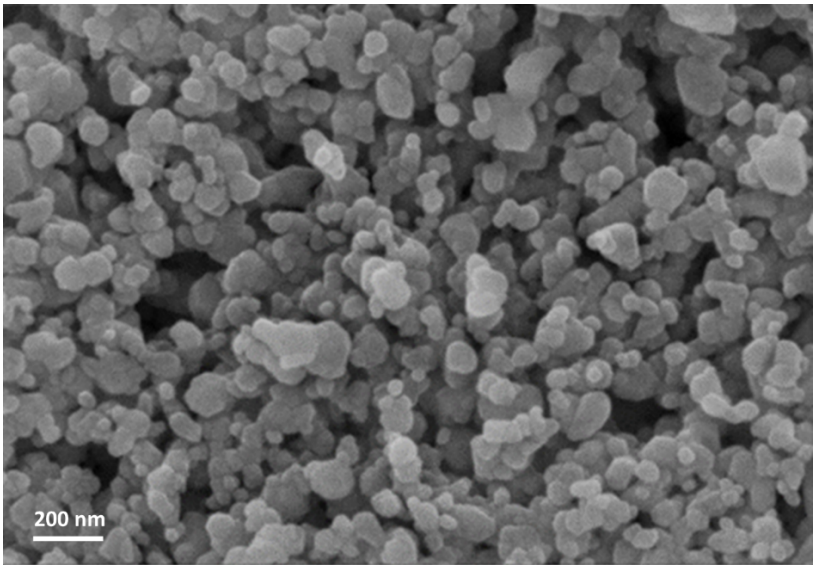

Figure A.2.8. The SEM image of the as-prepared Li_2MnO_3 powder. The as-prepared Li_2MnO_3 exhibits a single-particle morphology with average particle size of 100-200 nm.

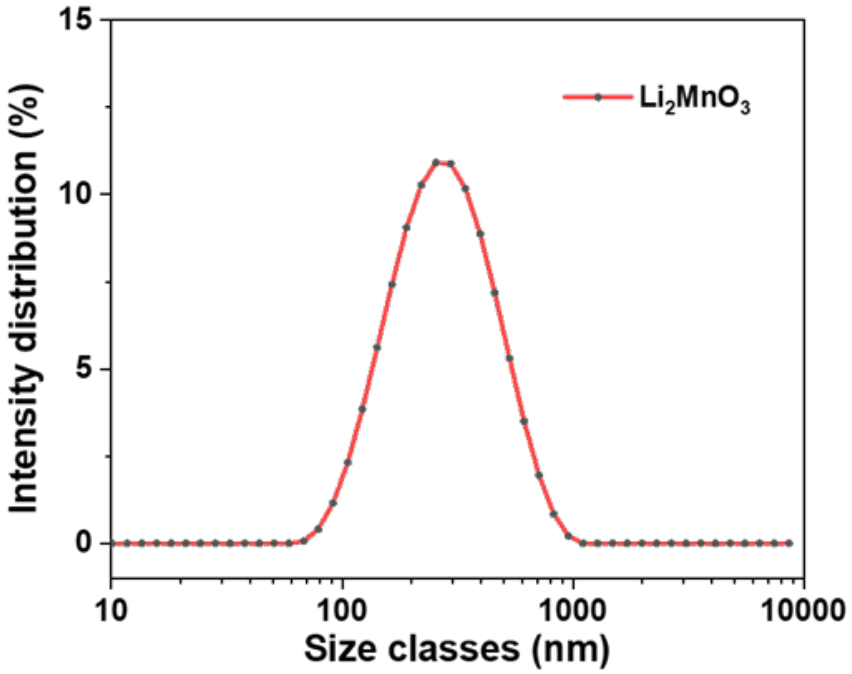

Figure A.2.9. The particle size distribution of the as-prepared Li_2MnO_3 powder. The particle size distribution of Li_2MnO_3 is analyzed using Zetasizer Nano ZS90. The particle size distribution is relatively wide, and its mean intensity locates at 304 nm because of the existence of particle agglomerates.

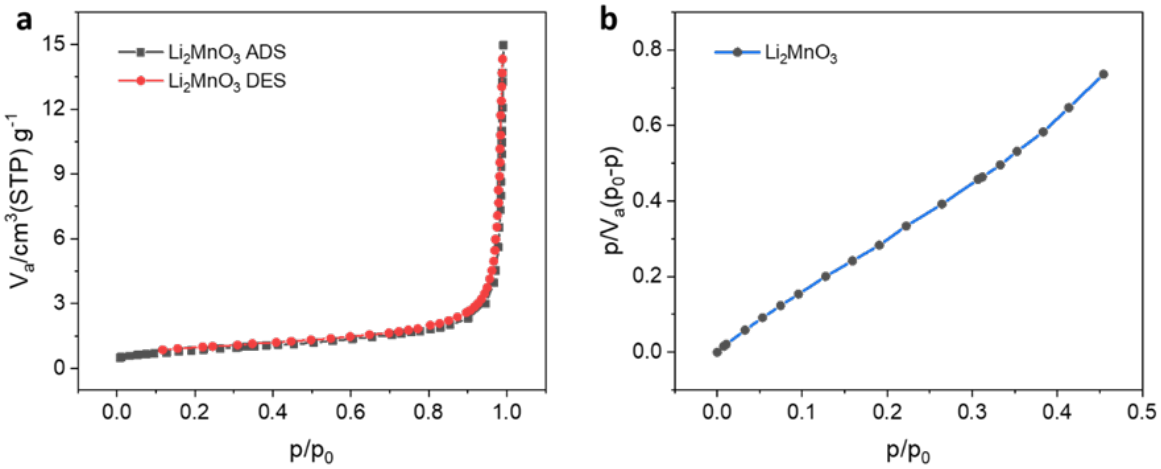

Figure A.2.10. Nitrogen physisorption analysis of the as-prepared Li_2MnO_3 powder. (a) The nitrogen adsorption/desorption isotherm of the as-prepared Li_2MnO_3 powder. (b) The corresponding BET plot of the as-prepared Li_2MnO_3 powder.

The specific surface area of Li_2MnO_3 is further characterized by a nitrogen physisorption analysis experiment and calculated using the Brunauer-Emmett-Teller (BET) model. The nitrogen adsorption/desorption isotherm and the corresponding BET plot of Li_2MnO_3 are shown in Figure A.2.10. The specific surface area of Li_2MnO_3 is calculated to be 3.1106 m^2 g^{-1}. In general, the morphology and surface area of Li_2MnO_3 are comparable to that of the LMR cathode.

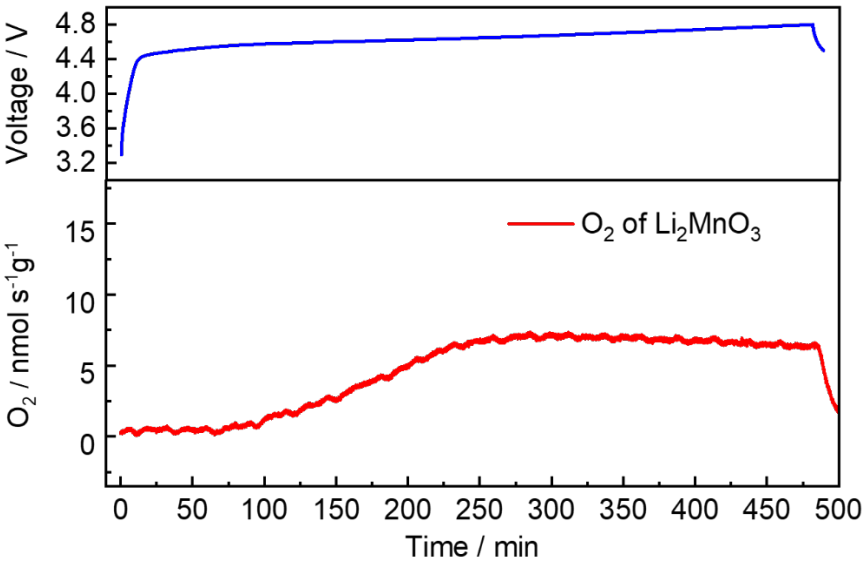

Figure A.2.11. *In-situ* differential electrochemical mass spectroscopy measurements for the first charge of Li_2MnO_3. The signal of O_2 evolution is not detected until 20% delithiation of Li_2MnO_3.

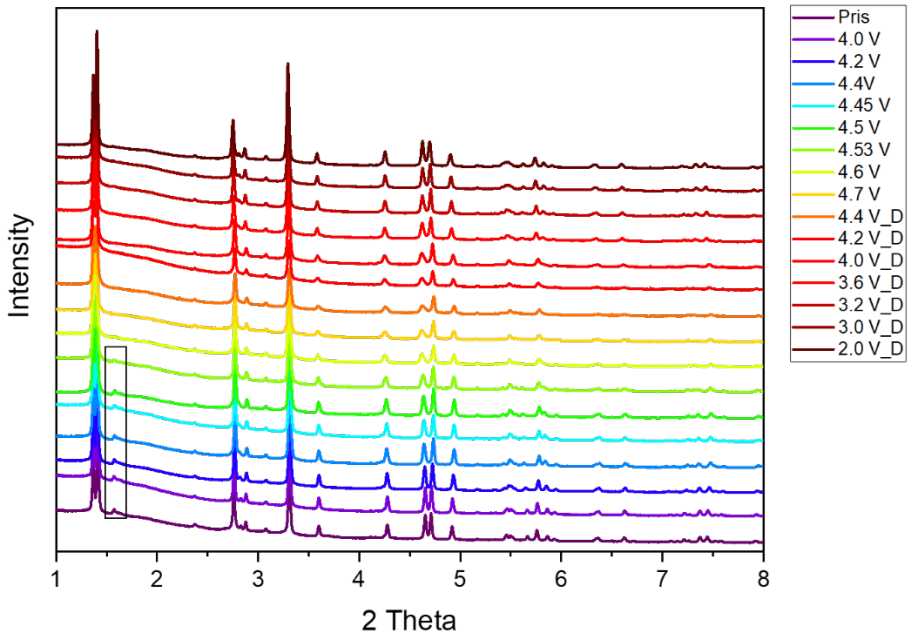

Figure A.2.12. The *ex-situ* XRD patterns of the first charge/discharge for the LMR cathode. The obvious lattice parameter changes can be observed from *ex-situ* XRD pattern, particularly in the 2 theta range of 3.0-6.0°.

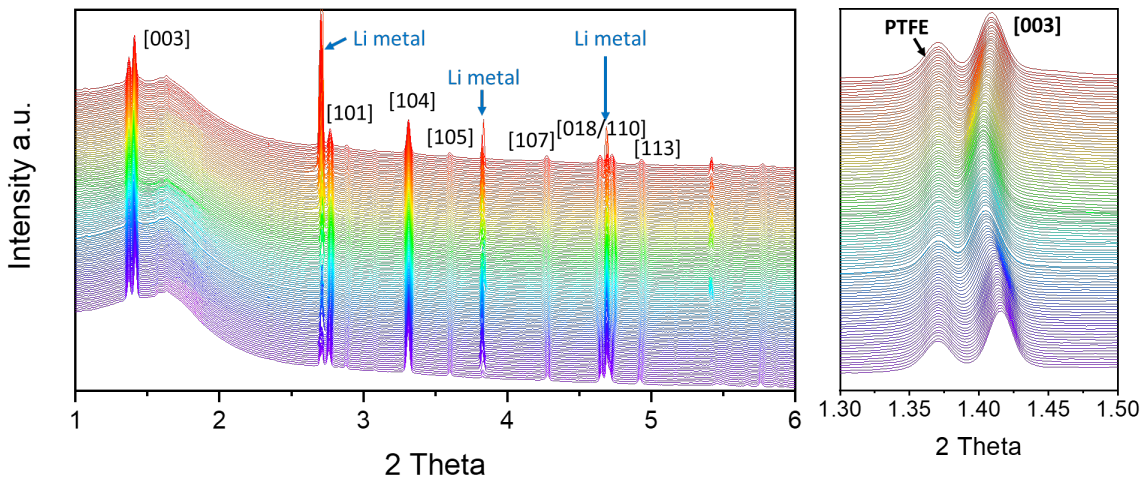

Figure A.2.13. The in-situ XRD patterns of the as-prepared LMR cathode during the first charge/discharge in the voltage range of 2.0-4.8 V using a current rate of C/10 (1C = 250 mA g^{-1}). The obvious lattice parameter changes can be observed from in situ XRD patterns, particularly in the 2-theta range of 1.3-1.5. Generally, the structure evolution observed in in-situ XRD is completely consistent with that in ex-situ XRD (Figure A.2.3c).

In situ HEXRD measurements during cycling were performed at the 11-ID-C beamline of the Advanced Photon Source at Argonne National Laboratory. The high penetration and low absorption of HEXRD is beneficial to observe tiny phase changes that are usually invisible from lab scale XRD. The 2032-coin cells have a 3 mm hole suitable for X-rays to pass through and diffraction patterns were collected every 10 minutes. Kapton tape was used to seal the holes of the coin cells, preventing them from air exposure.

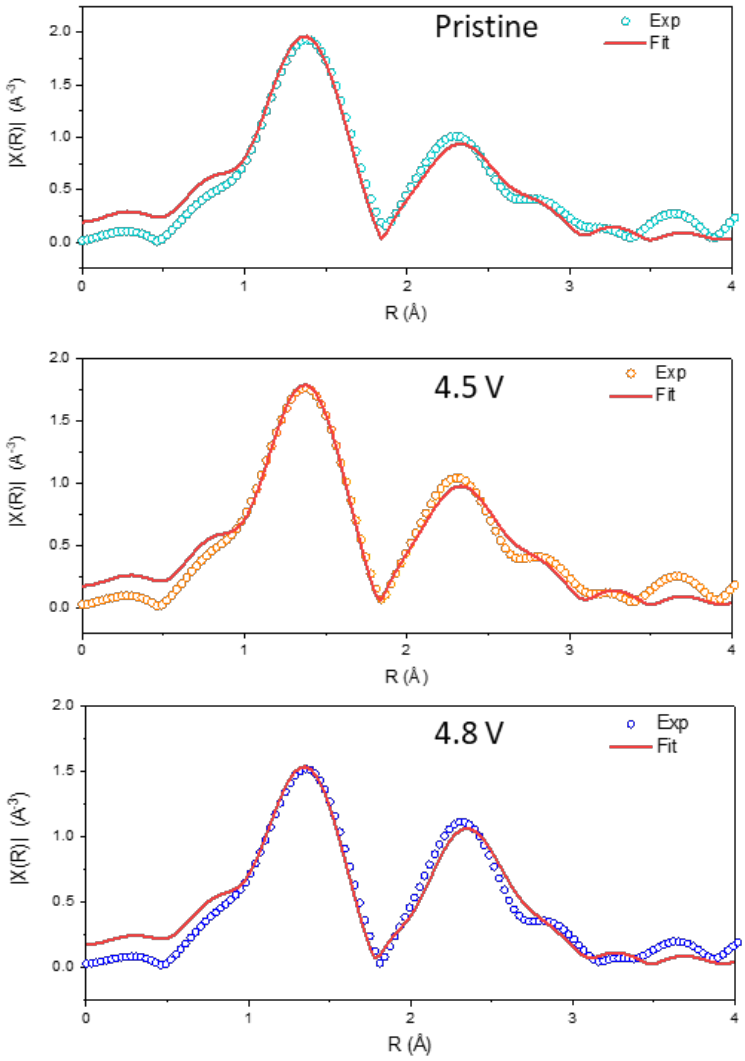

Figure A.2.14. *Ex-situ* Mn *K-edge* EXAFS spectra of the samples at pristine, 4.5V and 4.8V and the corresponding fitting results. Detailed fitting results are shown in Table A2.2.

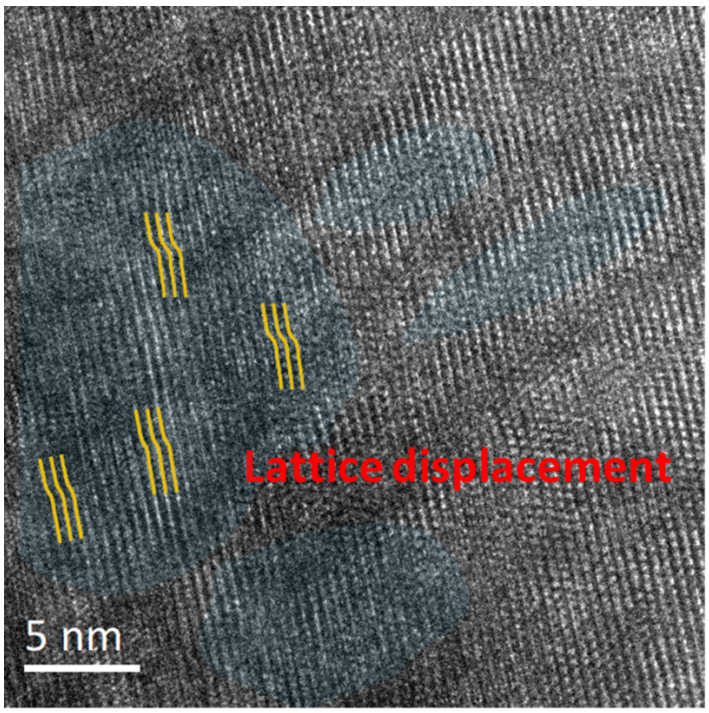

Figure A.2.15. Visible lattice displacement observations using TEM of the LMR charged to 4.47 V.

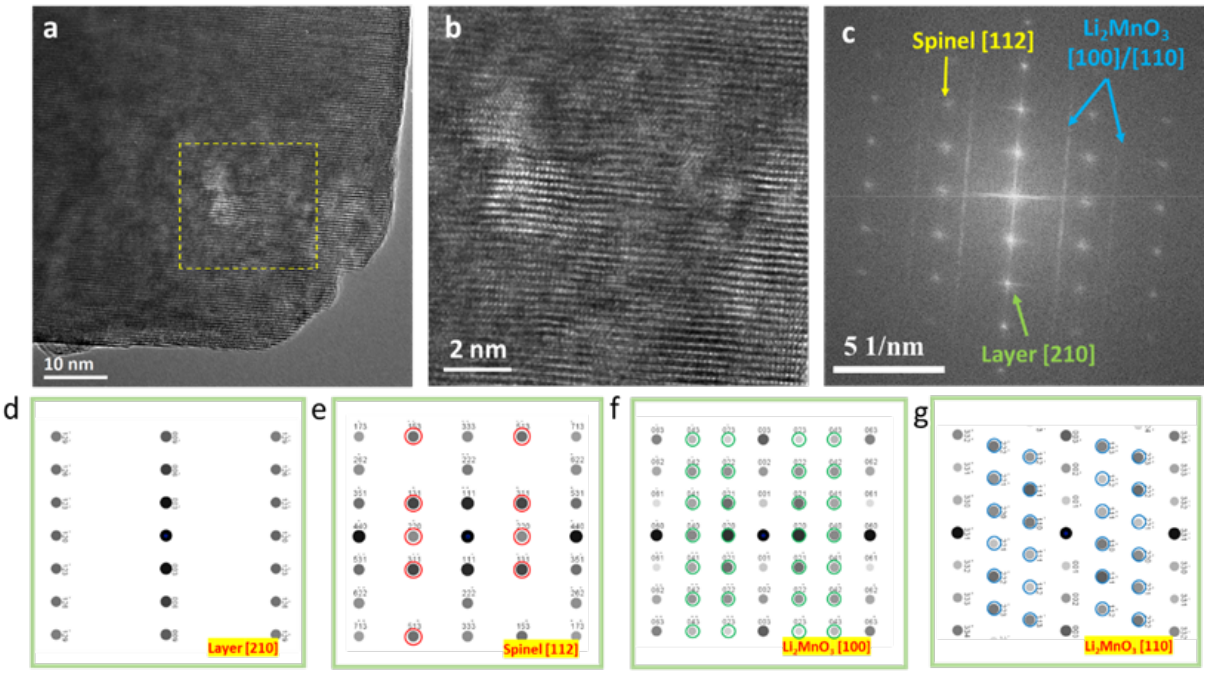

Figure A.2.16. Visible observations of the LMR charged to 4.5 V. (a) High magnification TEM image of the LMR charged to 4.5 V. (b) The enlarged image of the selected area in Figure A.2.16a. (c) The corresponding Fourier pattern of the select area of Figure A.2.16a. (d, e, f and g) The simulated patterns of standard electron diffractions for Layer [210], spinel [112], and Li_2MnO_3 [100]/[110].

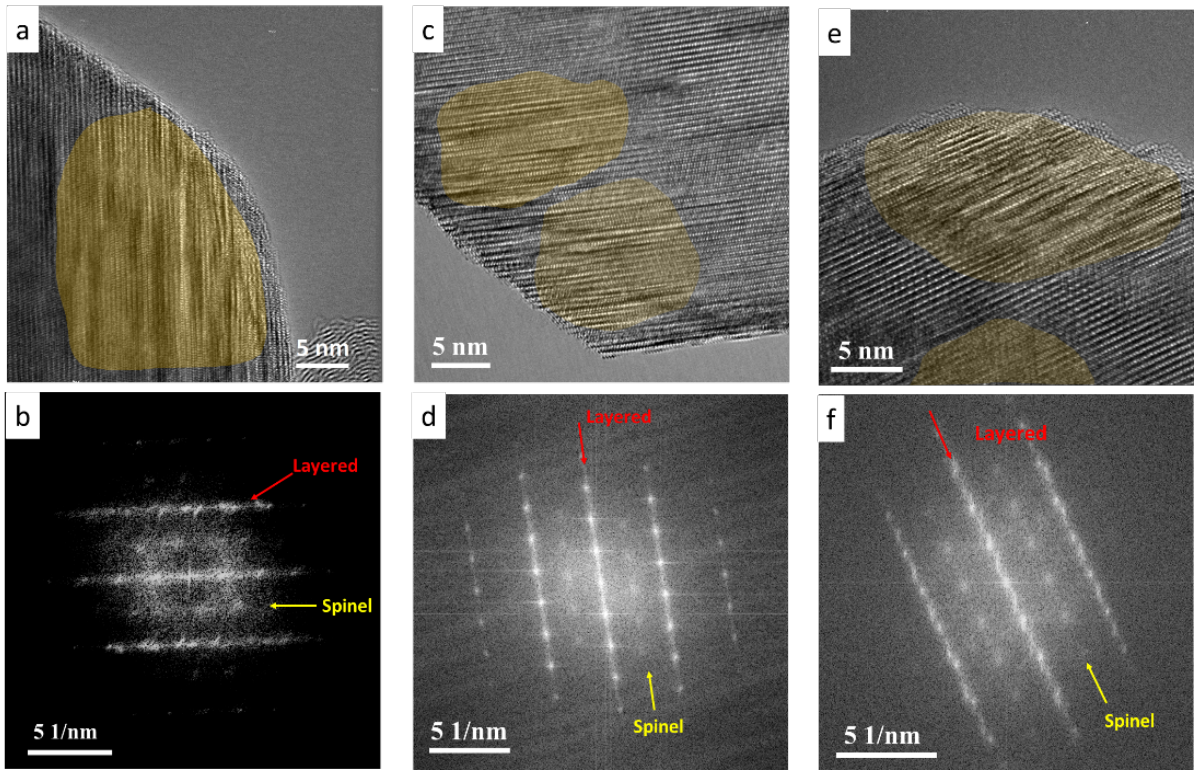

Figure A.2.17. (a, c and e) TEM images of the LMR cathode charged to 4.5 V. The lattice displacements are highlighted with yellow marks. (b, d and f) The corresponding FFT images of Figure A.2.17 (a, c and e). Obvious lattice displacements are observed in the different particles and the corresponding FFT images confirm the existence of spinel phase at 4.5 V, which is highly consistent with Figure A.2.4g results.

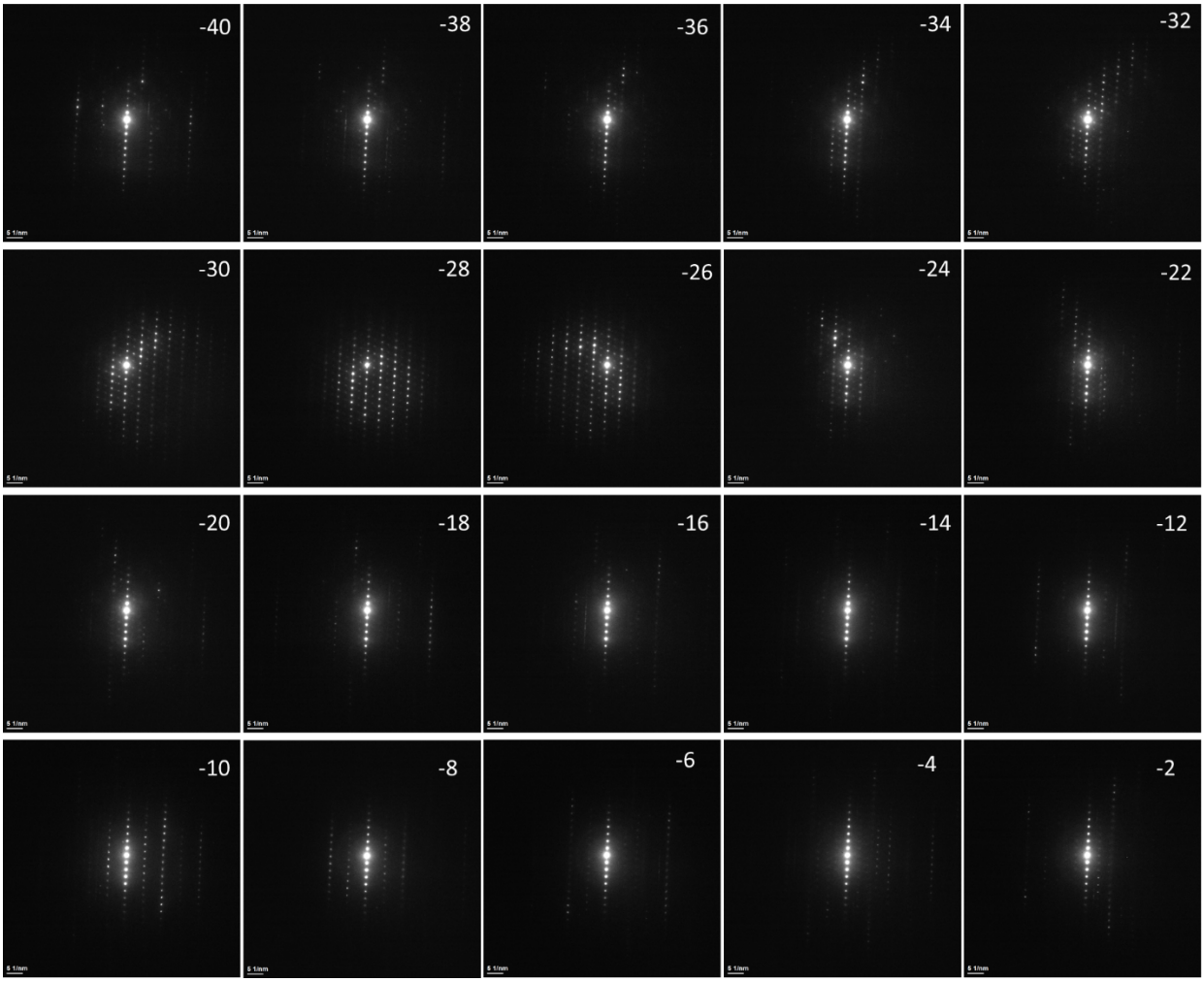

Figure A.2.18. The SAED images captured at different rotation angles from -40 to -2º. These SAED images in Figure A.2.19- 20 are used for 3D-rED reconstruction.

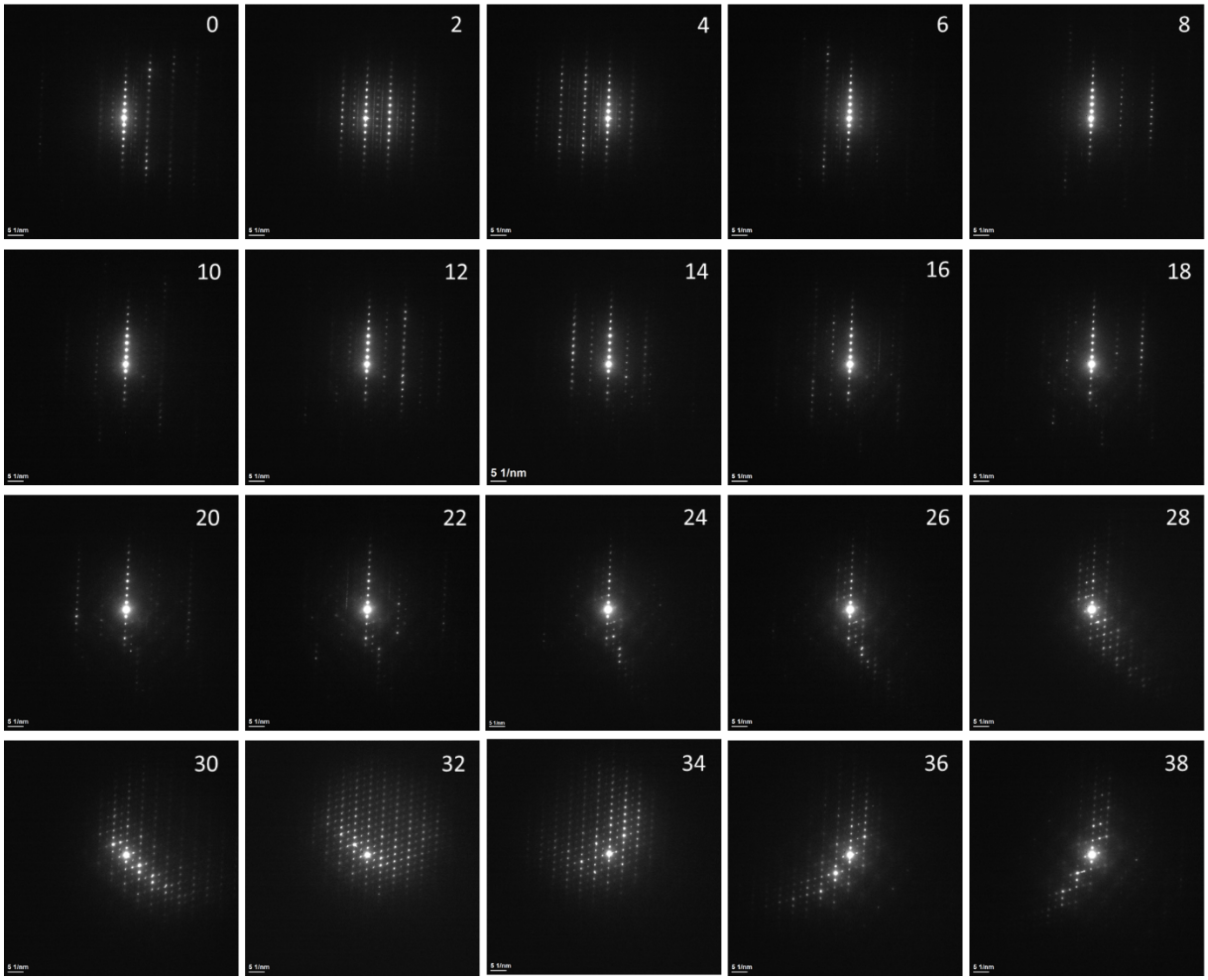

Figure A.2.19. The SAED images captured at different rotation angles from 0 to 38º. These SAED images in Figure A.2.19-20 are used for 3D-rED reconstruction.

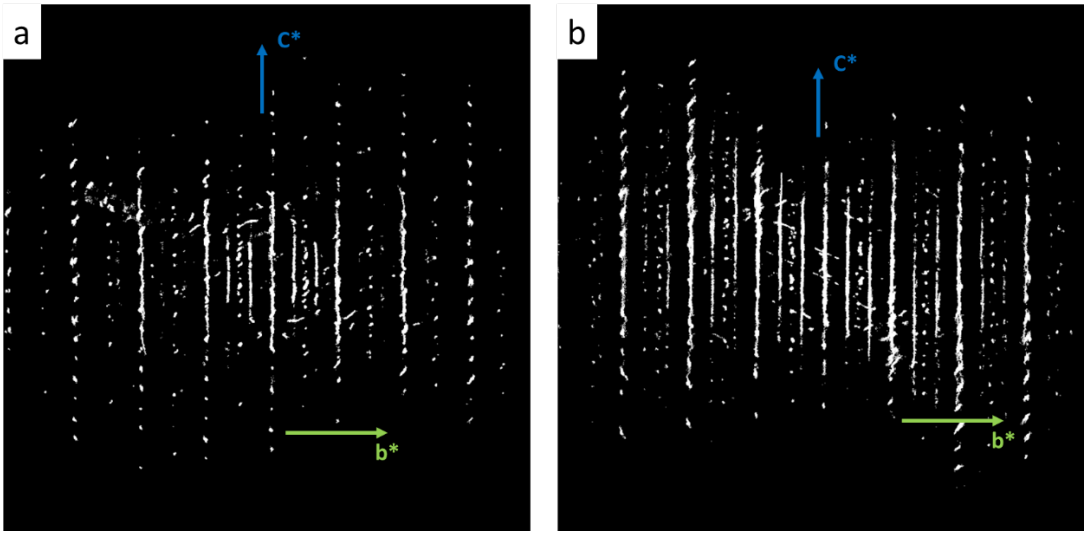

Figure A.2.20. (a and b) The reciprocal lattice viewed along the a* axis of the LMR cathode at 4.5 V.

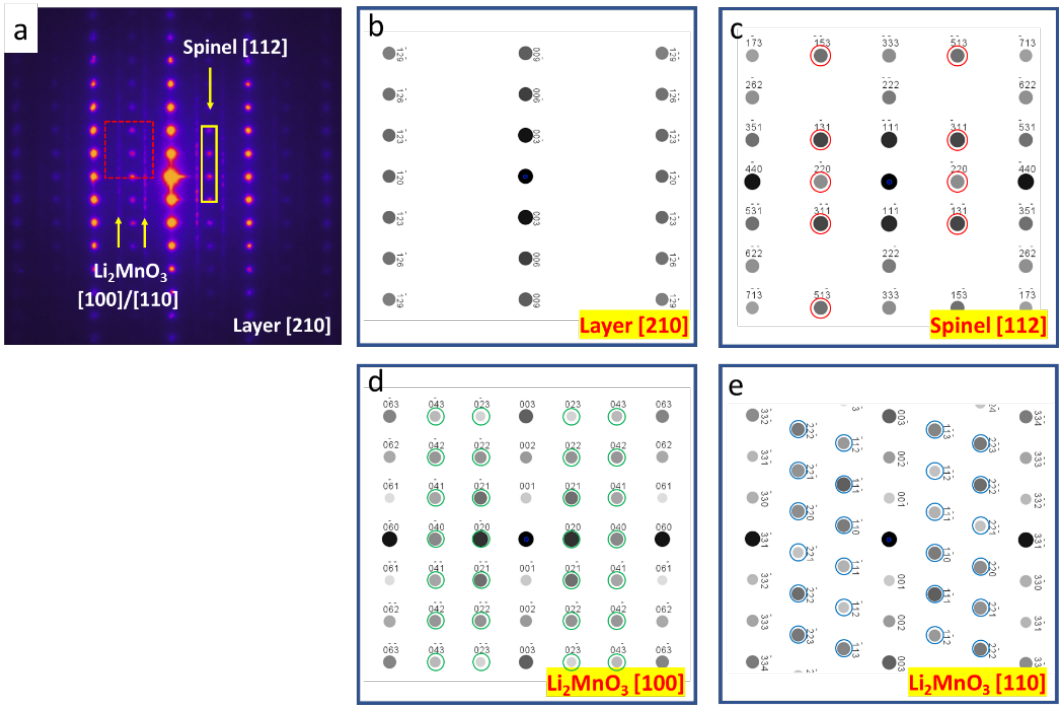

Figure A.2.21. (a) The selected area electron diffraction (SAED) image of the sample charged to 4.5 V. In addition to the typical layered structure and weak Li_2MnO_3 reflection, the reflection that corresponds to the spinel lattice can be also observed. (b, c, d and e) The simulated patterns of standard electron diffractions for Layer [210], spinel [112], and Li_2MnO_3 [100]/[110].

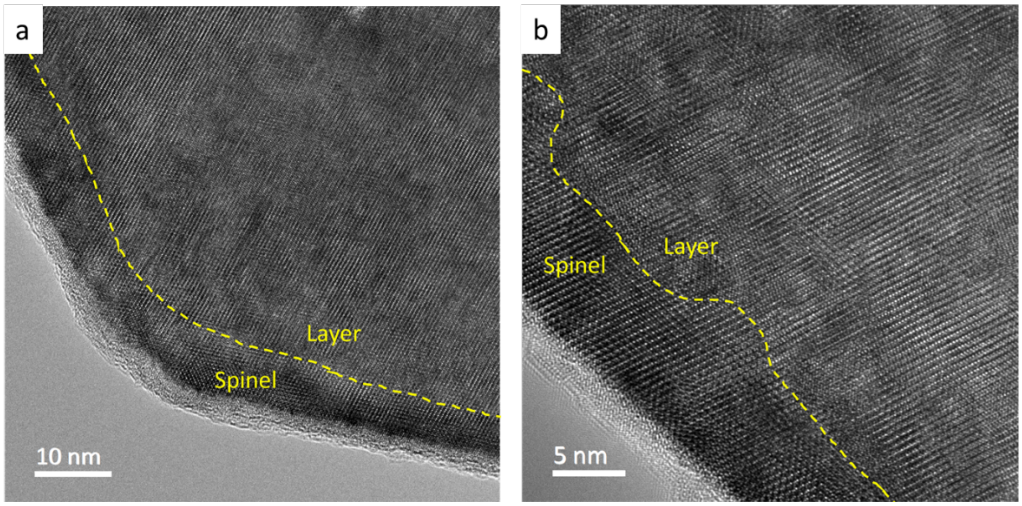

Figure A.2.22. Visible observations of the LMR charged to 4.8 V. (a) Low magnification TEM image of the LMR charged to 4.8 V. (b) High magnification TEM image of the LMR charged to 4.8 V. A clear reconstruction surface layer with the spinel phase can be visualized.

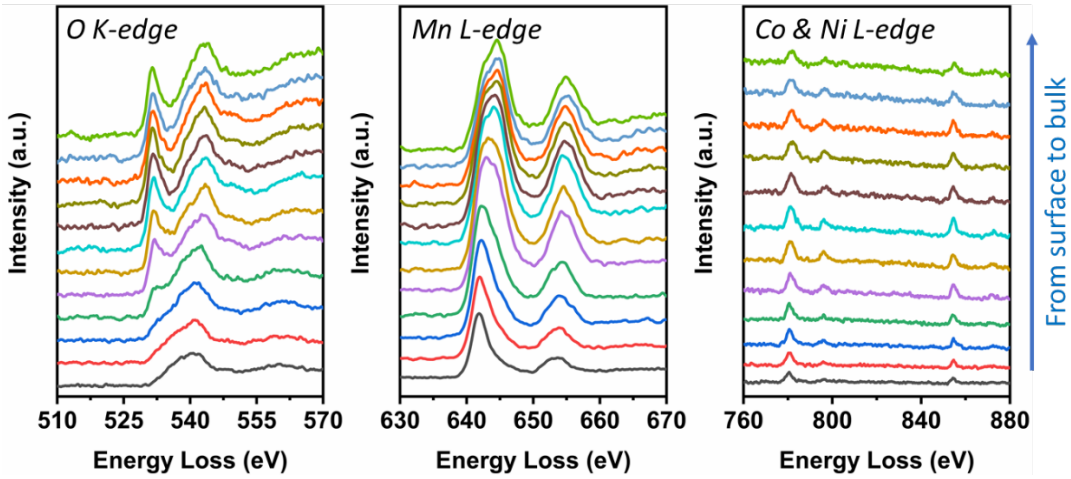

Figure A.2.23. Electron energy-loss spectroscopy line scans of the O *K-edge*, Mn *L-edge*, Co & Ni *L-edge* for the LMR charged to 4.8 V along the direction from surface to bulk. The intensity of O-K edge prepeaks substantially reduces from the interior to the exterior and almost disappears near the surface. Concurrently, Mn L-edge shows left shift near the surface.

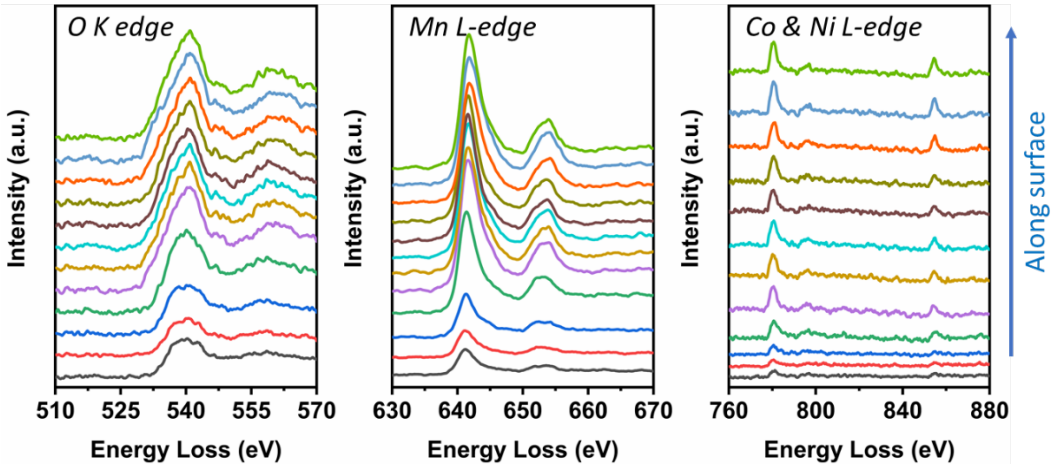

Figure A.2.24. Electron energy-loss spectroscopy line scans of the O *K-edge*, Mn *L-edge*, Co & Ni *L-edge* for the LMR charged to 4.8 V along the surface fringe. The O-K line-scan parallel to the surface confirms that the oxygen release uniformly occurs in the entire particle surface as the disappeared O prepeak.

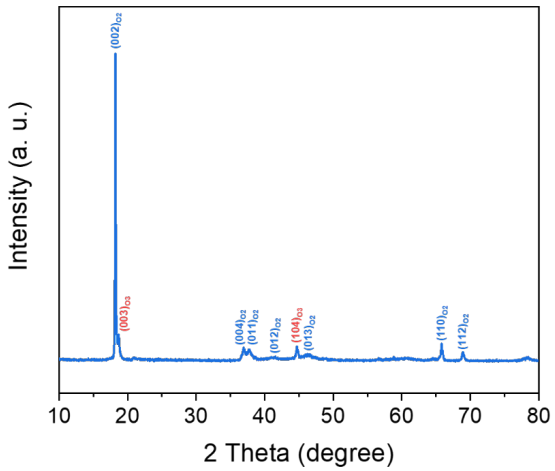

Figure A.2.25. The XRD pattern of as-prepared $Li_{1.03}Ni_{0.13}Mn_{0.54}Co_{0.13}O_2$. The diffraction peaks belonging to an O2 phase with P63mc symmetry are indexed by blue marks, while the others belonging to an O3 phase with R-3m symmetry are indexed by red marks.

The O2 phase based $LixNi_{0.13}Mn_{0.54}Co_{0.13}O_2$ was synthesized using a sol-gel method followed by a low-temperature ion exchange method. $NaCH_3COO·3H_2O$ (Aladdin, 99%), $LiCH_3COO·2H_2O$ (Aladdin, 99%), $Ni(CH_3COO)_2·4H_2O$ (Aladdin, 99%), $Mn(CH_3COO)_2·4H_2O$ (Aladdin, 99%), $Co(CH_3COO)_2·4H_2O$ (Aladdin, 99%) and Polyvinylpyrrolidone (Aladdin, K30) were mixed in a molar ratio of 85:20:13:54:13:370 and then dissolved in 50 mL of deionized water. The resulting solution was dried at 90 °C overnight and then calcinated at 500 °C for 3 hours. The obtained powder was thoroughly ground and mixed in a mortar and then calcinated at 800 °C for 10 hours to obtain the sodium containing precursor, $Na_{0.83}Li_{0.2}Ni_{0.13}Co_{0.13}Mn_{0.54}O_2$. Note that 20% Li in this precursor mainly occupies the TM layers, and 83% Na occupies the Na layers. Finally, the precursor was subjected to ion exchange in eutectic $LiNO_3$-LiCl at 280 °C for 4 hours to obtain $Li_{0.83}Li_{0.2}Ni_{0.13}Mn_{0.54}Co_{0.13}O_2$. To simplify, it can be written as $Li_{1.03}Ni_{0.13}Mn_{0.54}Co_{0.13}O_2$.

The XRD pattern of as-prepared $Li_{1.03}Ni_{0.13}Mn_{0.54}Co_{0.13}O_2$ is shown in Figure A.2.7. The major diffraction peaks can be well indexed to an O2 phase with P63mc symmetry, while the other minor ones can be indexed to an O3 phase with R-3m symmetry. Therefore, $Li_{1.03}Ni_{0.13}Mn_{0.54}Co_{0.13}O_2$ is mainly O2 phase based with minor O3 phase coexisted.

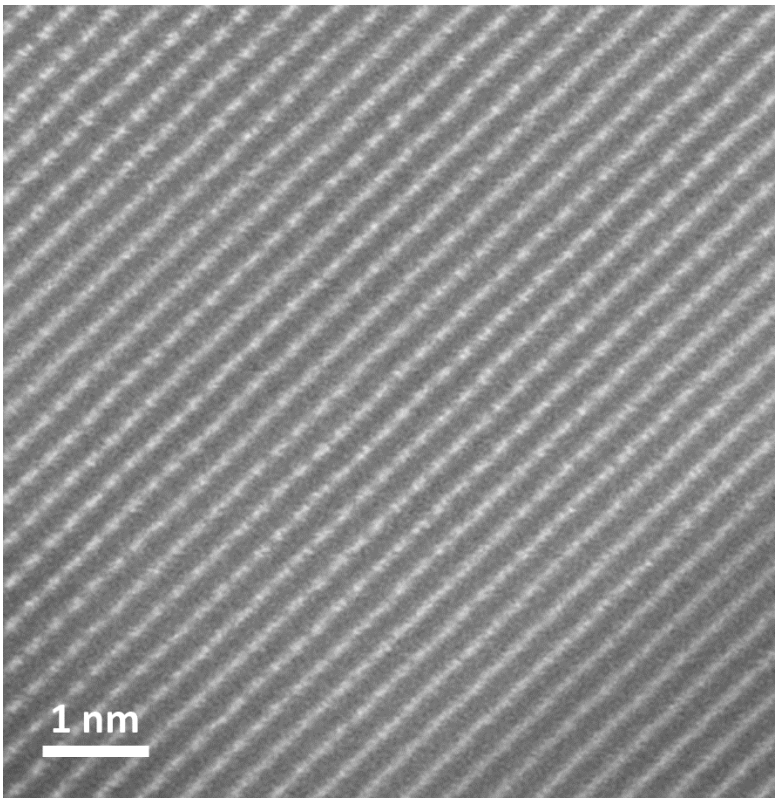

Figure A.2.26. High resolution TEM image showing the atomic arrangements of O2 phase LMR. The domain structure is eliminated and replaced by homogeneous atomic arrangement. Since it has been proven challenging to alter the domain mesostructure of the O3 type-LMR, we attempted to eliminate composite domain structure with homogeneous atomic arrangement in O2 type-LMR cathode. As shown in Figure A.2.25, the Li_2MnO_3-like domain is rarely observed in the O2-type LMR, which suggests that the structural motifs in the O2 type LMR cathode are dispersed in the TM layer instead of being aggregated to form a Li_2MnO_3-like domain.

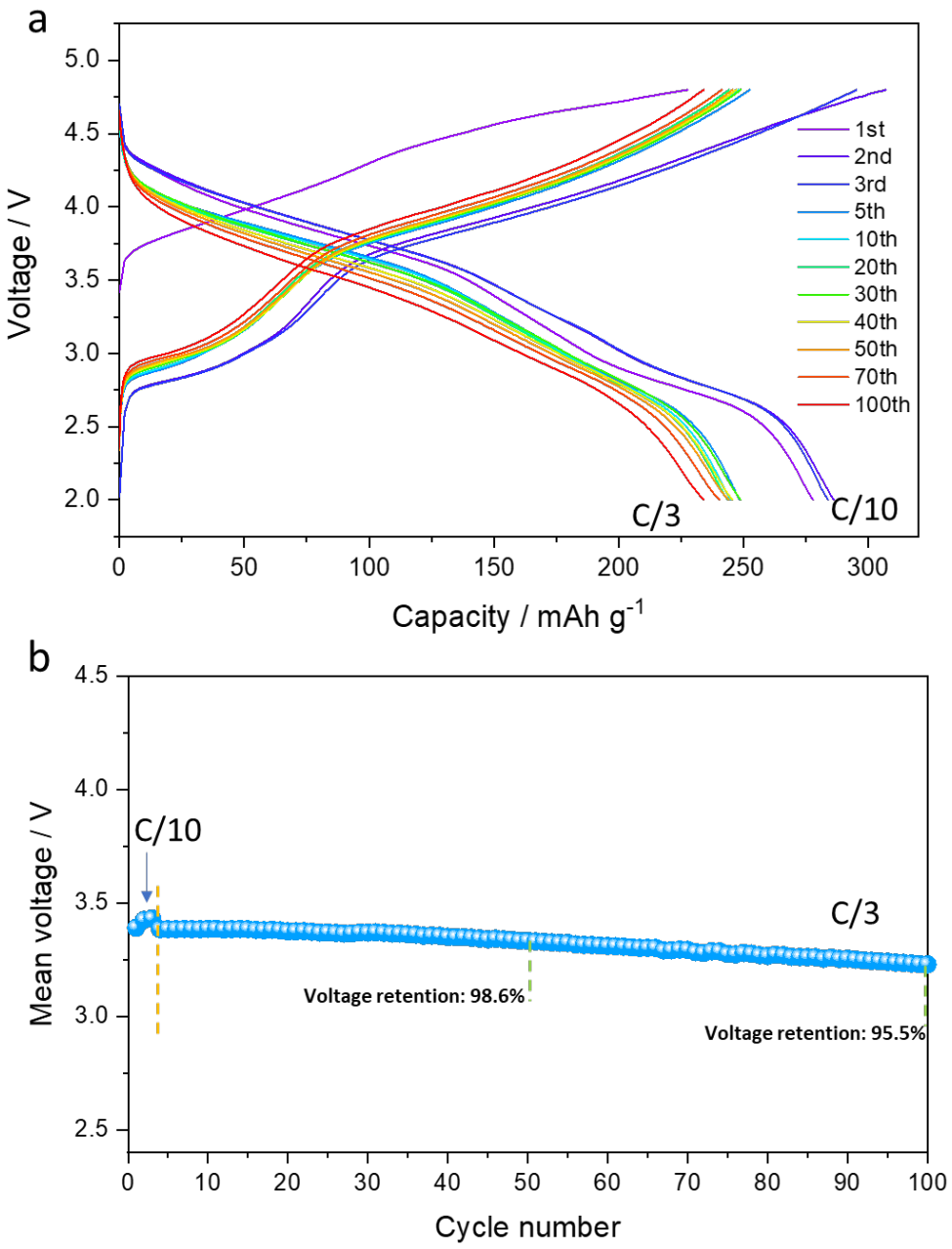

Figure A.2.27. (a) The charge/discharge profiles of O2 phase based-LMR cathode. The cells were activated at C/10 within first 2 cycles and then cycled at C/3. The smooth charging behavior with no apparently differentiated voltage plateaus indicates effectively suppressed differential electrochemical activities. (b) The voltage stability of the O2 type-LMR cathode during cycles presents in the plot of average (mean) voltage profiles vs cycle number.

Table A.2.1. Lattice parameters obtained by the two-phase structure model refinement of pristine LMR cathode.

Phases			
Phase 1 Space group: $R\bar{3}m$	**Phase fraction**		**0.57(4)**
	Lattice parameters	*a=b*	2.8535(6) (Å)
		c	14.2424(9) (Å)
		V	100.43(6) (Å^3)
Phase 2 Space group: *C2/m*	**Phase fraction**		**0.43(4)**
	Lattice parameters	*a*	4.9488(1) (Å)
		b	8.5485(4) (Å)
		c	5.0366(6) (Å)
		β	109.556(0) (°)
		V	200.78(2) (Å^3)
Agreement factors	Rwp (%)		5.73
	Rp (%)		5.86

The XRD pattern of the LMR cathode is refined using the two-phase model, which consists of both rhombohedral R3$\bar{}$m and monoclinic C2/m phases that are present in LMR cathodes.

Table A.2.2. Structural parameters of the samples obtained by fitting the EXAFS data. There are the average coordination number (CN), path distance (R), Debye-Waller factor (σ^2), threshold energy correction (ΔE), and the R-Factor of the fitting.

Samples	Shells	CN	R (Å)	σ^2 (Å^2)	ΔE (eV)	R-Factor
pristine	Mn-O	6	1.905	0.003	-5.3	0.014
	Mn-TM	2.8	2.869	0.003		
charged to 4.5 V	Mn-O	5.3	1.904	0.003	-4.7	0.010
	Mn-TM	2.7	2.873	0.003		
charged to 4.8 V	Mn-O	4.9	1.890	0.005	-7.7	0.015
	Mn-TM	3.8	2.875	0.005		

Appendix B: Supporting Information for Chapter 3

Table B.3.1. The refinement results of the HEXRD measurements of SC75, including lattice parameters, Li/Ni disorder and R_{wp}.

Samples	a=b	c	Li/Ni disorder	R_{wp}
SC75	2.8710	14.1995	5.44%	0.0746

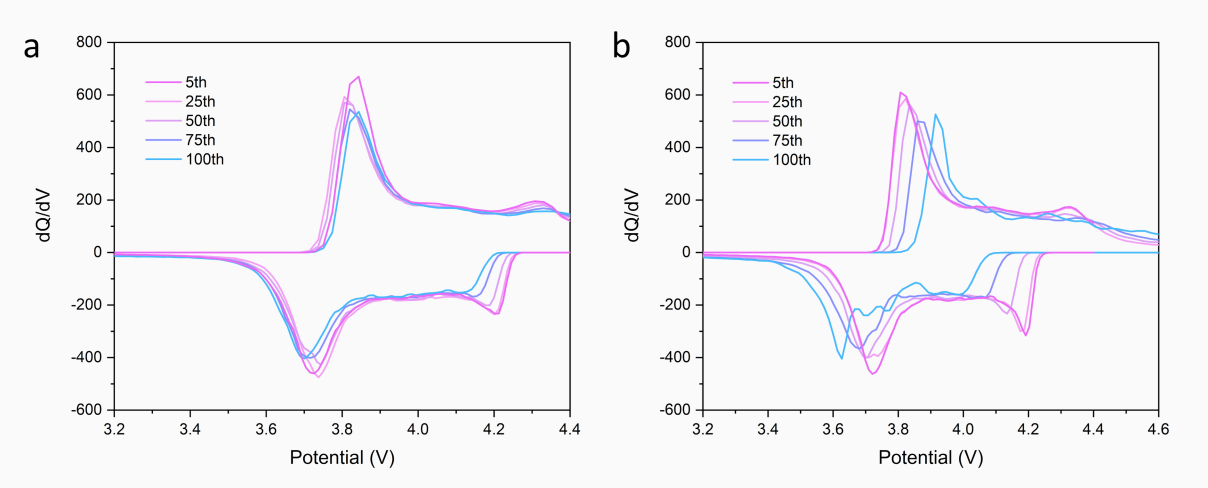

Figure B.3.1. The *dQ/dV* curves for 4.4 V and 4.6 V cycling, respectively.

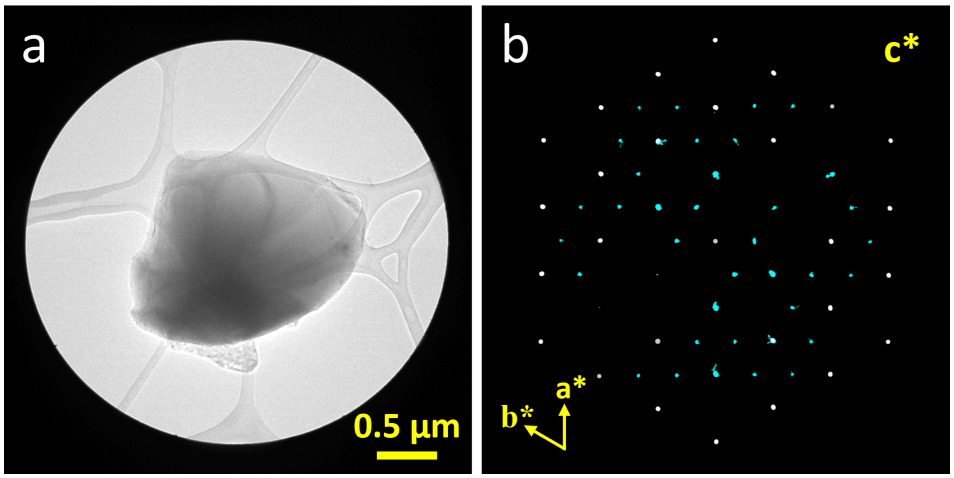

Figure B.3.2. (a), The TEM image of the selected particle for 3D-CRED. (b) The reconstructed 3D-reciprocal lattice projections along the c* direction.

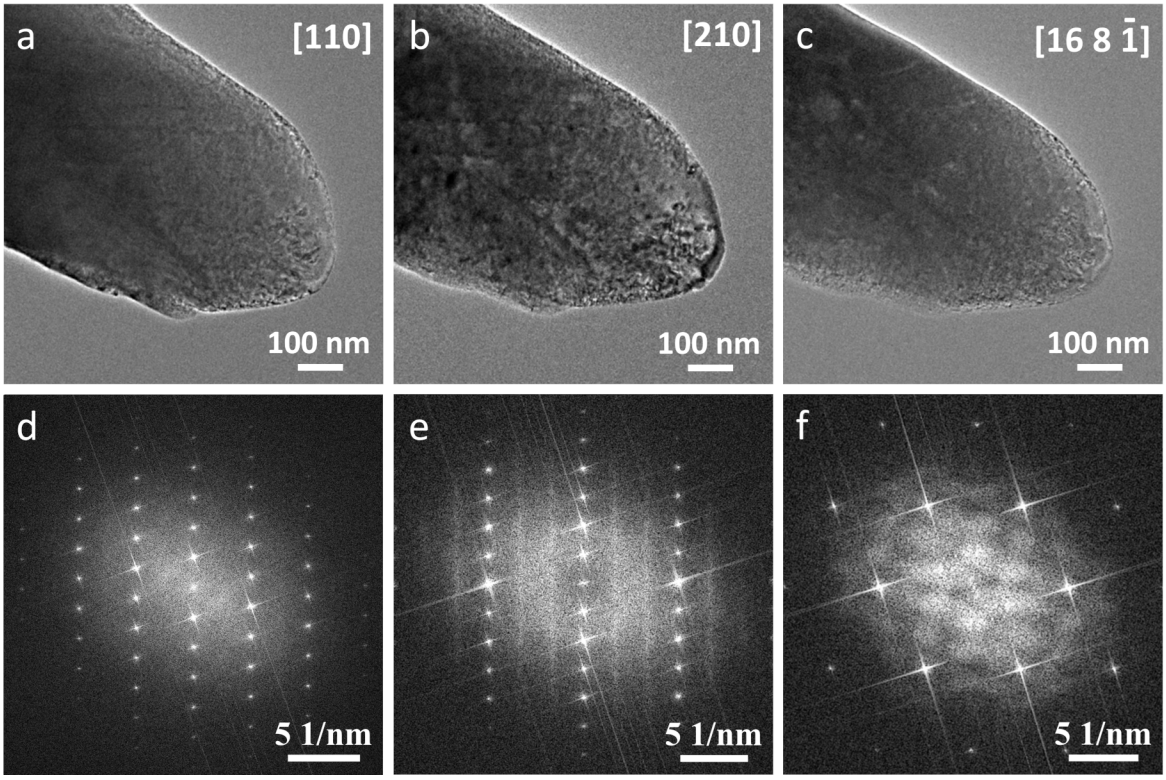

Figure B.3.3. (a-c) The low-magnification TEM images of a same SC75 particle along different zone axises. (d-f) The corresponding fast Fourier transformation (FFT) patterns of the HRTEM images in the Figure B.3.3g-i.

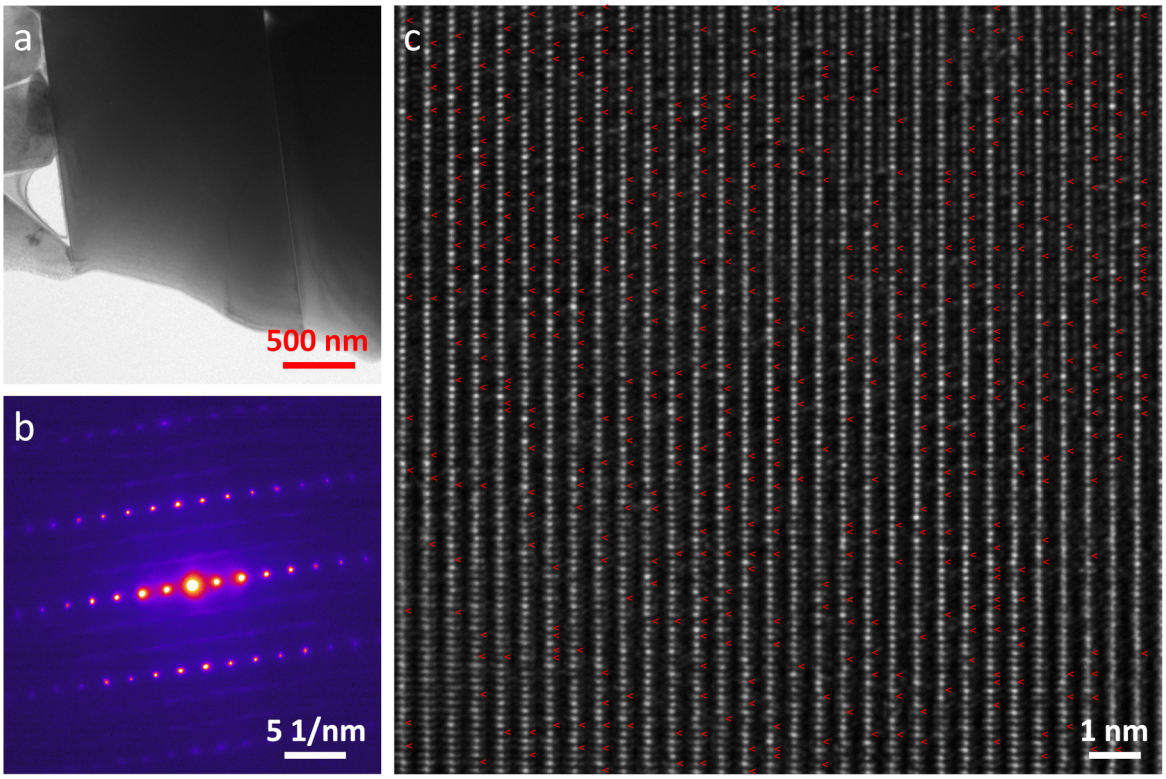

Figure B.3.4. (a) The low-magnification TEM image of the SC75 particle along the [210] zone axis. (b) The corresponding SAED pattern. (c) The HRTEM image with red indicators showing the dim dots.

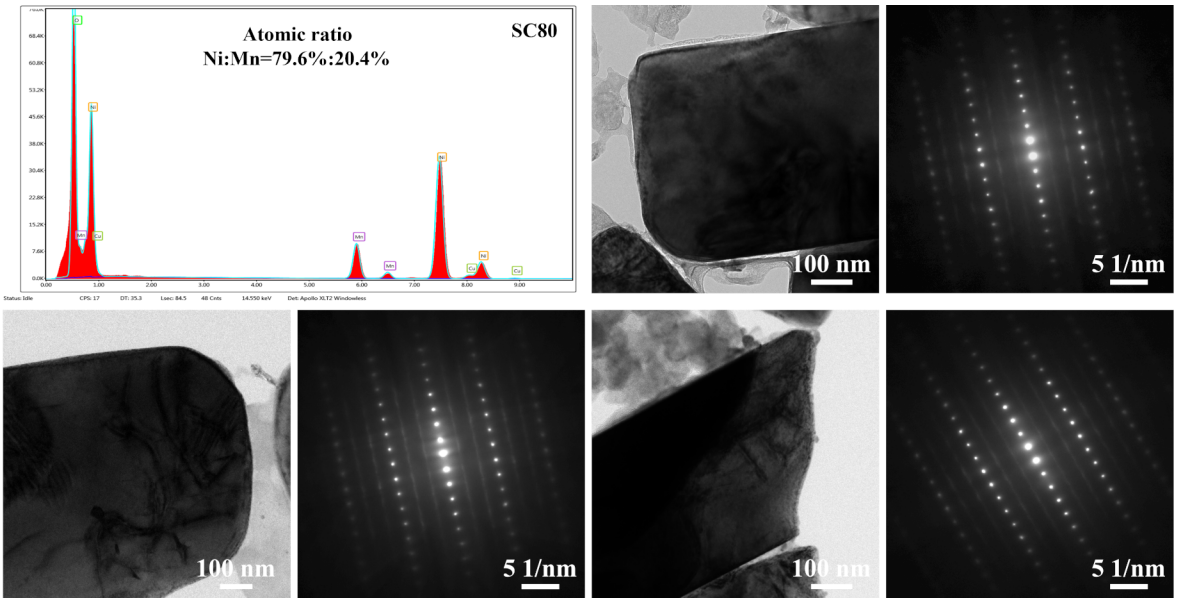

Figure B.3.5. The EDS spectrum and structural characterization of the SC80 sample.

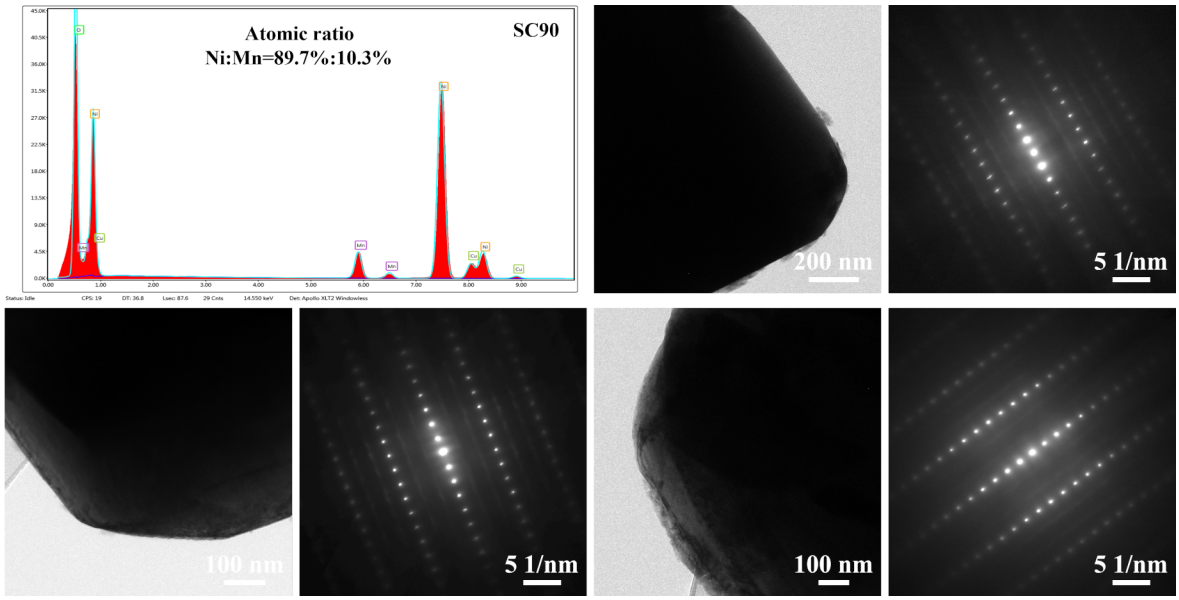

Figure B.3.6. The EDS spectrum and structural characterization of the SC90 sample.

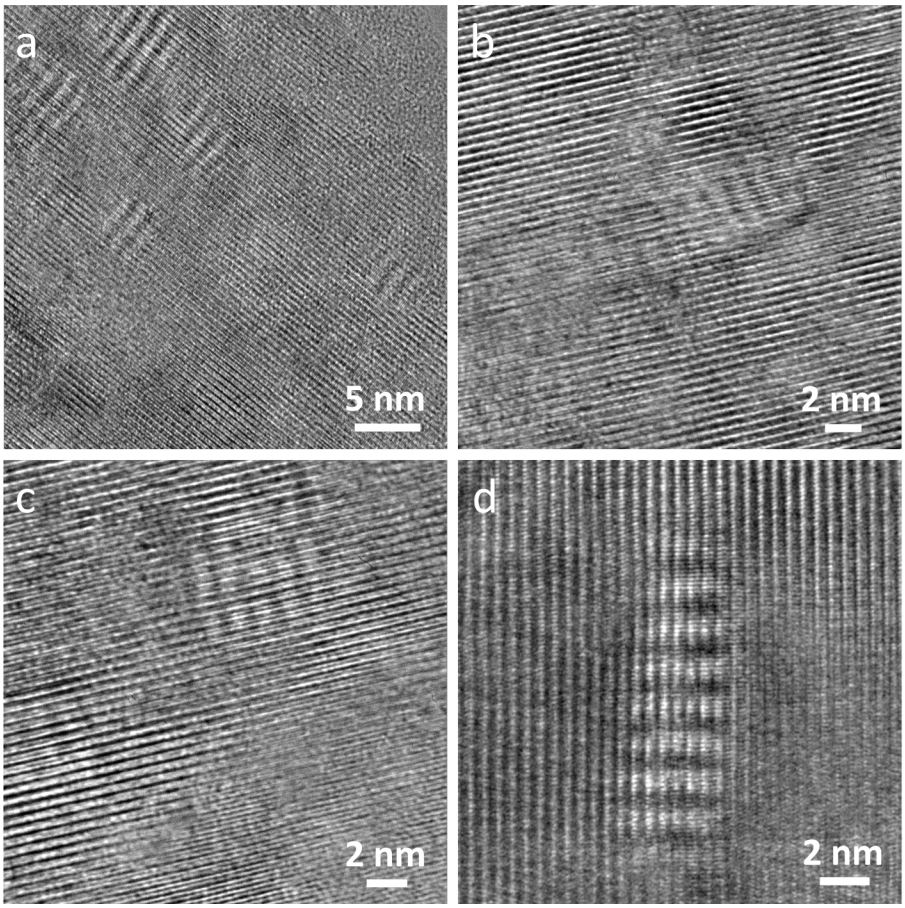

Figure B.3.7. (a-d) The high-magnification TEM images of the SC75 cathode after 100 cycles at 0.5C and 2.8-4.4 V, showing the moire patterns.

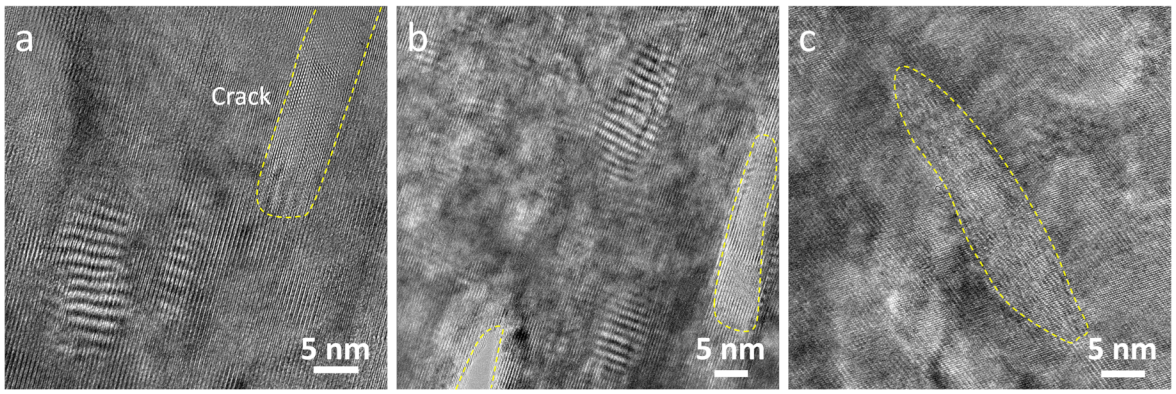

Figure B.3.8. (a-c) The high-magnification TEM images of the SC75 cathode after 100 cycles at 0.5C and 2.8-4.6 V, showing the moire patterns and cracks.

Appendix C: Supporting Information for Chapter 4

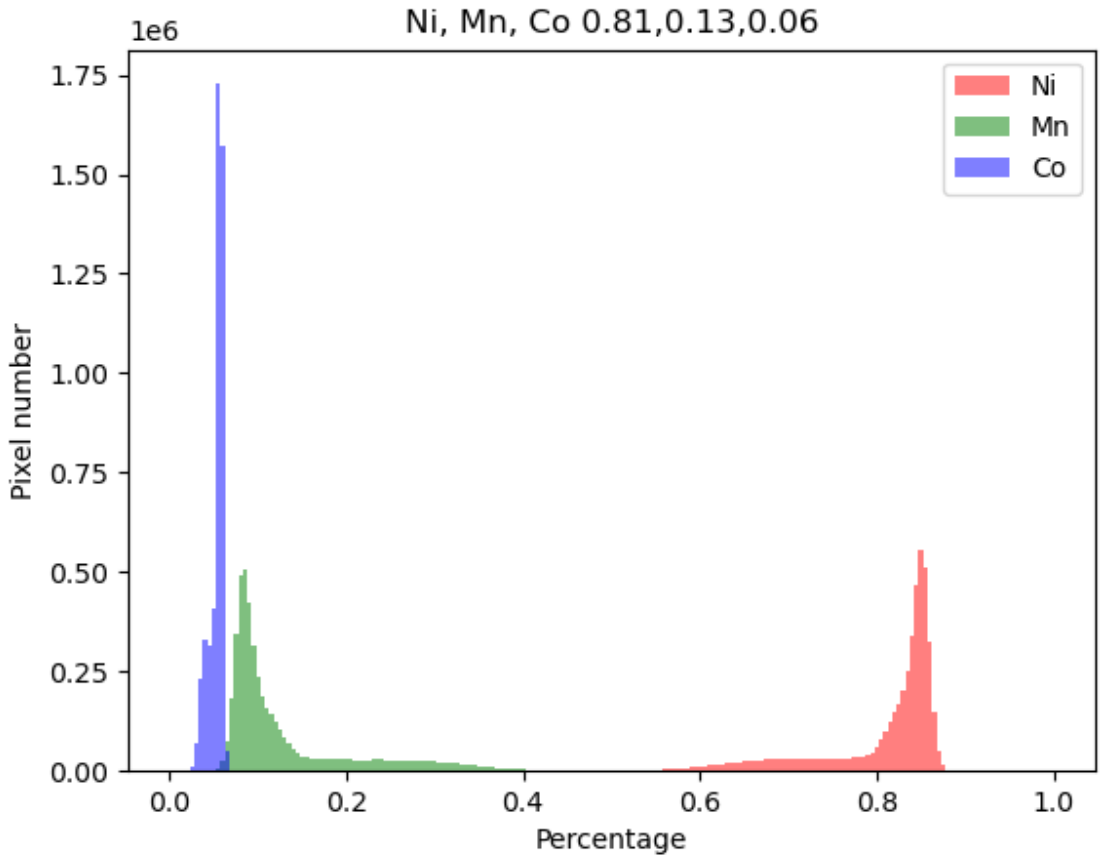

Figure C.4.1. Quantitative composition profile obtained from 3D XRF showing average Ni, Mn, and Co compositions.

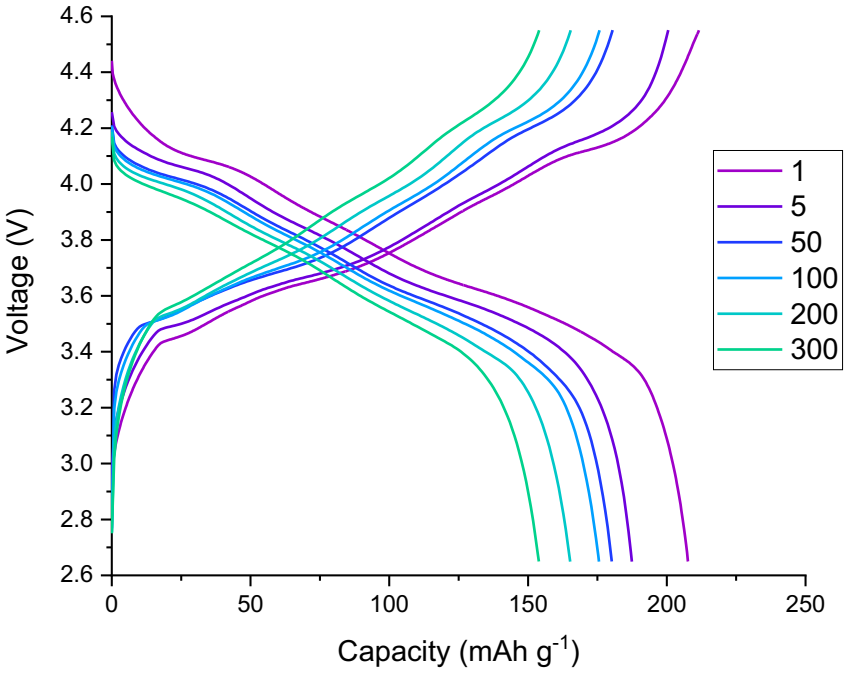

Figure C.4.2. Cycling charge/discharge profiles of MS-NMC full cells using graphite anode with voltage range of 2.65 – 4.55 V, current rate of 1C, and temperature controlled to 25°C.

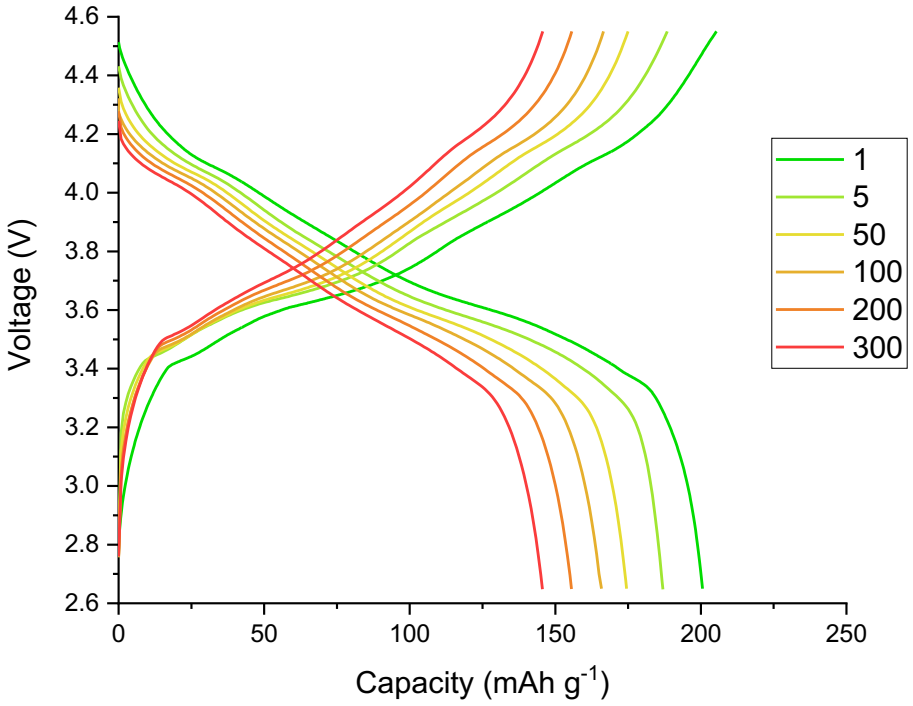

Figure C.4.3. Cycling charge/discharge profiles of NMC811 full cells using graphite anode with voltage range of 2.65 – 4.55 V, current rate of 1C, and temperature controlled to 25°C.

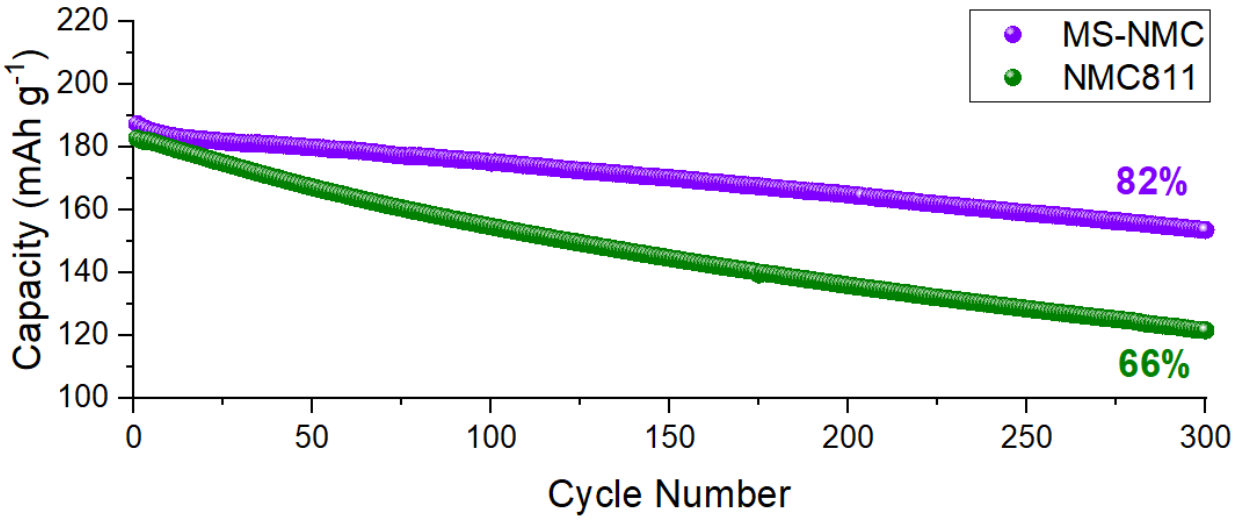

Figure C.4.4. Cycle performance of MS-NMC and NMC811 full cells using graphite anode with voltage range of 2.65 – 4.55 V, current rate of 1C, and temperature controlled to 25°C.

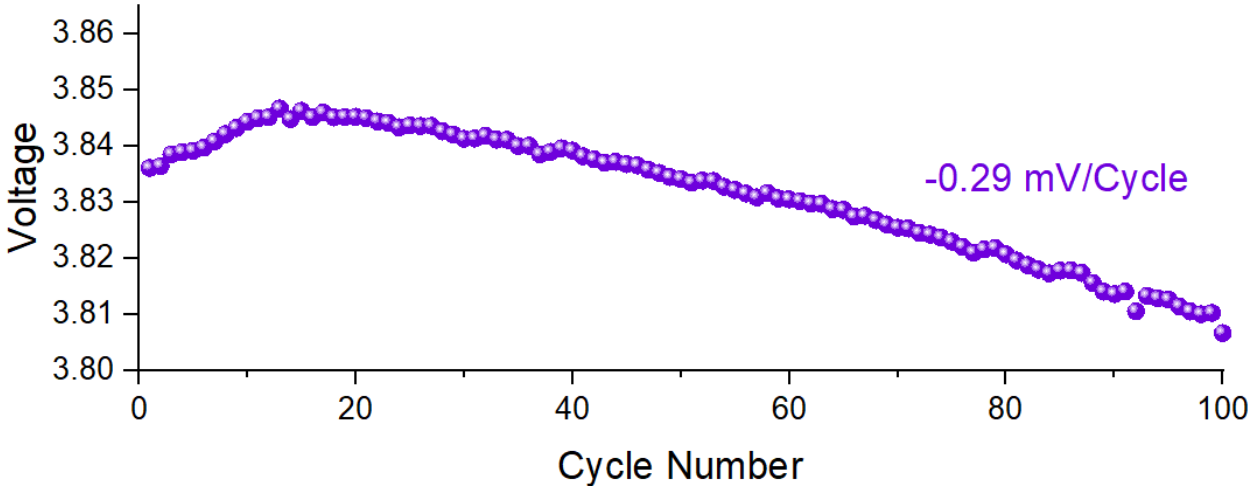

Figure C.4.5. Average voltages for MS-NMC in half cell format and cycled within a voltage range of 2.7 – 4.6 V, current rate of 0.5C, and at room temperature (22 ± 0.5°C).

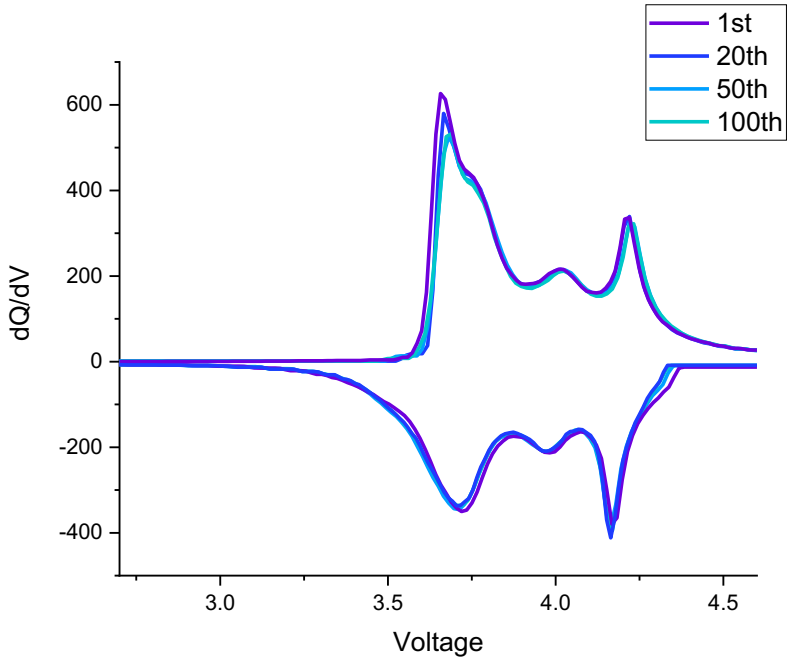

Figure C.4.6. dQ/dV profiles for MS-NMC in half cell format and cycled within a voltage range of 2.7 – 4.6 V, current rate of 0.5C, and at room temperature (22 ± 0.5°C).

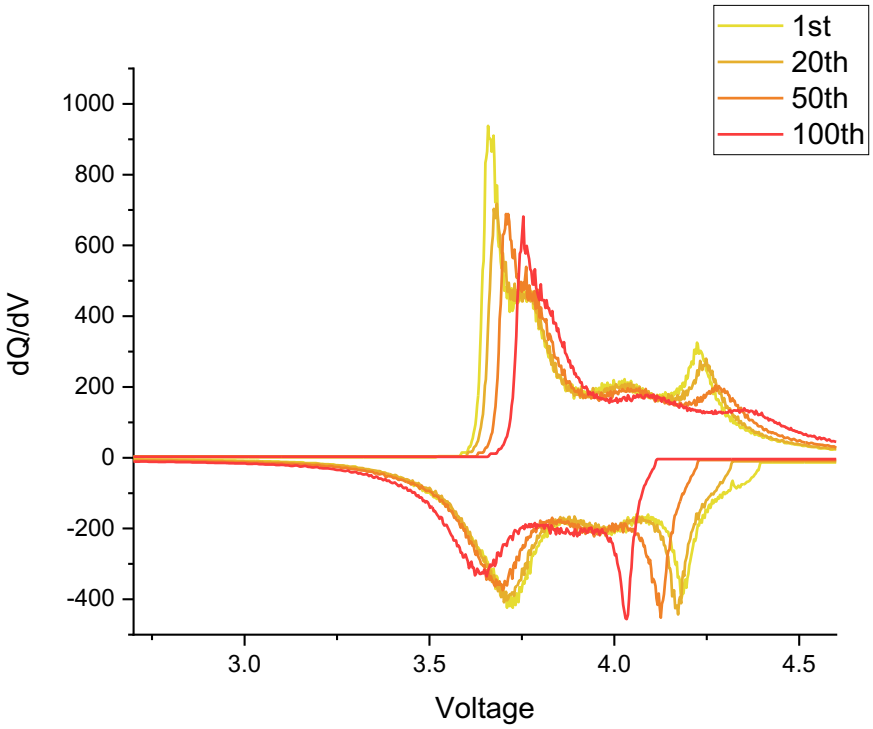

Figure C.4.7. dQ/dV profiles for NMC811 in half cell format and cycled within a voltage range of 2.7 – 4.6 V, current rate of 0.5C, and at room temperature (22 ± 0.5°C).